

**UCSF**

**UC San Francisco Electronic Theses and Dissertations**

**Title**

Magnetic resonance elastography at 3 tesla: Implementation, validation and application to a degenerative disc model

**Permalink**

<https://escholarship.org/uc/item/2833q34j>

**Author**

Dunn, Timothy Christian

**Publication Date**

2005

Peer reviewed|Thesis/dissertation

**Magnetic Resonance Elastography at 3 Tesla:  
Implementation, Validation and Application to a  
Degenerative Disc Model**

by

**Timothy Christian Dunn**

DISSERTATION

Submitted in partial satisfaction of the requirements for the degree of

DOCTOR OF PHILOSOPHY

in

Bioengineering

in the

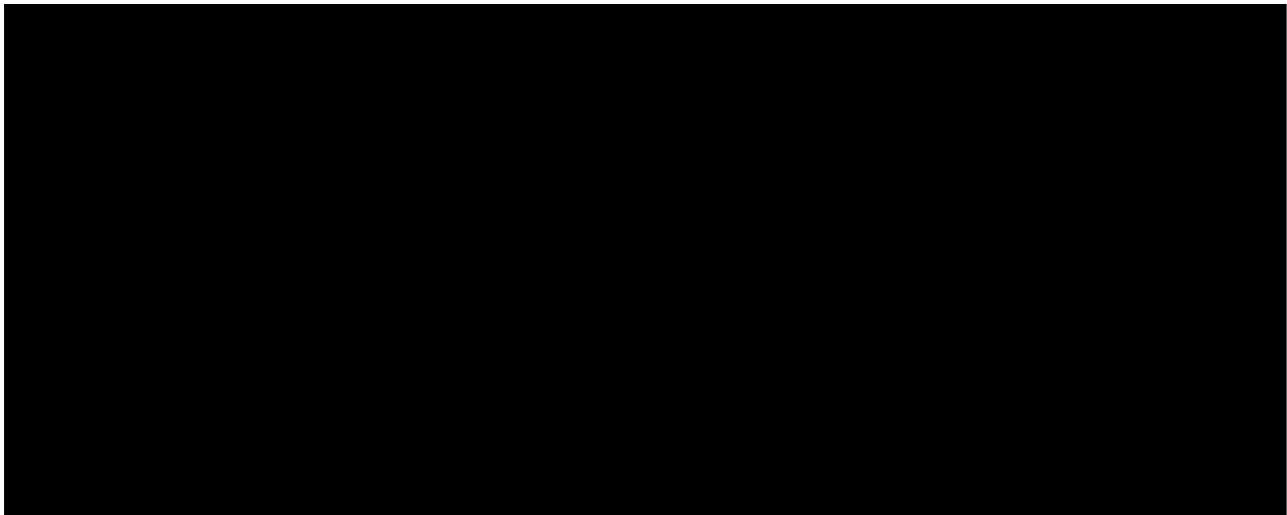
GRADUATE DIVISIONS

of the

UNIVERSITY OF CALIFORNIA SAN FRANCISCO

and

UNIVERSITY OF CALIFORNIA BERKELEY



Date

University Librarian

Degree Conferred: .....

---

## Acknowledgements

---

No undertaking can be completed successfully without preparation and support from those around you, and this dissertation is directly the result of support from my advisers, lab members, and family.

My adviser Sharmila Majumdar is first to be thanked for letting me wander away from her main focus areas into the realm of elastography. She showed incredible faith and courage in my abilities, and remembering this helped during those times I thought I might be irrecoverably lost. There have been many influential and helpful people from the UCSF and Berkeley communities, and in particular I'd like to thank my lab group members David Newitt, Thomas Link, Julio Carballido-Gamio, Roland Krug, Suchandrima Banerjee, Andy Burghardt, Jan Bauer, Gabby Blumenkrantz, Galatea Kazakia, Kayvan Keshari and Xiaojuan Li. Eric Han from GE patiently helped me learn the necessary details of software programming for the scanner, and Lucas Carvajal, Kostas Karpodinis, Duan Xu, and Dan Vigneron helped immensely with technical aspects of running the scanner and getting my elastography hardware built and operational.

My parents, Caroline and Mark, always nurtured my fledgling engineering tendencies, and I thank them deeply for their continuing support. Finally, my wife Claudia has been a pillar of encouragement, helping me in more ways than can be listed, more than anyone, and for this I thank and love her.

Magnetic resonance (MR) elastography has been increasingly attractive for medical research as it provides a non-invasive method of determining the shear mechanical properties of soft tissues, and therefore offers the potential to provide a novel and sensitive measure of tissue changes related to health and disease. The present work develops a MR elastography technique to evaluate ex vivo intervertebral disc tissue samples. The implementation is described across the features of the MR scanner software, necessary experimental hardware, phantom and tissue preparation, and image post-processing.

The system was characterized across several variables, but the focus of the work shows the effect of motion encoding waveform shape as well as the number and frequency of applied motion and motion encoding cycles. The results of this evaluation found that trapezoidal motion encoding gradients perform better than sinusoidal motion encoding gradients. This result is supported by theoretical derivations. In addition, while relatively high frequencies of operation were achieved on the present system, it was found that an operating frequency of 500 Hz provided the best operational compromise.

The method was applied to quantitatively measure the shear modulus of agar gel samples and bovine intervertebral disc nucleus pulposus tissue. The agar gel measurements compared well with those from traditional compressive mechanical testing. The fitted linear regression lines for the shear modulus from the two methods against agar gel concentration were found to be equivalent. For the bovine tissue, the method was found to effectively determine the change in stiffness of the tissue due to enzymatic degradation using papain. The shear modulus was found to significantly decrease from an average value of 60 kPa before injection to 44 kPa after injection. T2

values were found to increase significantly with degradation, while T1 values remained unchanged.

The work presented here details the implementation and validation of an MR elastography system, and its novel application to the study of intervertebral disc tissue. The method is found to be sensitive to tissue changes, and provides a foundation of future work of applying the method for the detection and tracking of early degenerative changes in disc tissue in vivo.

UCSF LIBRARY

---

# Table of Contents

---

|   |             |
|---|-------------|
| <b>Acknowledgements</b> .....   | <b>iii</b>  |
| <b>Abstract</b> .....   | <b>iv</b>   |
| <b>Table of Contents</b> .....  | <b>vi</b>   |
| <b>List of Tables</b> .....   | <b>viii</b> |
| <b>List of Figures</b> .....  | <b>ix</b>   |
| <b>1. Introduction</b> .....  | <b>1</b>    |
| 1.1 Background .....  | 1           |
| 1.2 Elastography literature review.....   | 3           |
| 1.3 Intervertebral disc degeneration .....  | 7           |
| 1.4 Scope and objectives.....   | 8           |
| <b>2. Methods Overview</b> .....  | <b>10</b>   |
| 2.1 MR Physics .....  | 10          |
| 2.2 Theory of velocity encoding .....   | 12          |
| 2.3 Implementation.....   | 14          |
| 2.3.1 <i>Pulse Sequences</i> .....  | 14          |
| 2.3.2 <i>Software</i> .....   | 17          |
| 2.3.3 <i>Hardware</i> .....   | 24          |
| 2.3.4 <i>Sample Preparation</i> .....   | 27          |
| 2.4 Phase image processing.....   | 29          |
| 2.4.1 <i>Phase Difference Calculation</i> .....   | 30          |
| 2.4.2 <i>Phase unwrapping</i> .....   | 32          |
| 2.4.3 <i>Phase to noise ratio</i> .....   | 42          |
| 2.4.4 <i>Strain wavelength estimation</i> .....   | 42          |
| 2.4.5 <i>Directional Filtering</i> .....  | 43          |
| 2.4.6 <i>Local Frequency Estimation (LFE)</i> .....                                       | 45          |
| 2.4.7 <i>Direct Inversion (DI)</i> .....  | 46          |
| 2.4.8 <i>Phase Image acquisition on a GE scanner</i> .....                                | 47          |
| 2.4.9 <i>MREView program</i> .....  | 50          |
| <b>3. Technique comparisons</b> .....   | <b>51</b>   |
| 3.1 Single-variable effects.....  | 51          |
| 3.1.1 <i>Number of Applied Motion Cycles</i> .....  | 51          |
| 3.1.2 <i>Gradient Shape: Trapezoidal v. Sinusoidal</i> .....                              | 53          |
| 3.1.3 <i>High Frequency experiments (&gt;500 Hz)</i> .....                                | 65          |
| 3.2 SE v. GRE with varying MEGs.....  | 69          |
| 3.2.1 <i>SE v. GRE background</i> .....   | 69          |
| 3.2.2 <i>SE v. GRE at 500 Hz</i> .....  | 73          |
| 3.2.3 <i>MR Imaging</i> .....   | 75          |
| <b>4. Applications</b> .....  | <b>89</b>   |
| 4.1 Embedded Gel samples.....   | 89          |
| 4.1.1 <i>Pilot Study of Agar Stiffness with Elastography and Mechanical Testing</i> ..... | 90          |
| 4.1.2 <i>Comprehensive Agar Stiffness Study</i> .....                                     | 100         |
| 4.2 Ex vivo Bovine Cervical Intervertebral Disc.....                                      | 108         |
| 4.2.1 <i>T1 and T2 maps of bovine cervical intervertebral disc</i> .....                  | 108         |
| 4.2.2 <i>Elastography of bovine cervical intervertebral disc</i> .....                    | 109         |
| 4.3 Pilot Study of Ex Vivo Bovine Caudal Intervertebral Disc Elastography.....            | 112         |

|       |  |     |
|-------|--|-----|
| 4.3.1 | <i>Comparison of elastography acquisition method</i> .....   | 114 |
| 4.3.2 | <i>Comparison of embedding material: Purified Water and PBS</i> .....  | 116 |
| 4.4   | <b>Comprehensive Study of Ex Vivo Bovine Caudal Intervertebral Disc Elastography with Swelling and Digestion</b> ..... | 117 |
| 4.4.1 | <i>Sample preparation: swelling and latex coating</i> .....  | 117 |
| 4.4.2 | <i>Papain Digestion Injection</i> .....  | 120 |
| 4.4.3 | <i>Elastography, T1 and T2 mapping</i> .....   | 120 |
| 4.4.4 | <i>Results</i> .....   | 121 |
| 4.4.5 | <i>Discussion</i> .....  | 126 |
| 5.    | <b>Conclusion and Future Plans</b> .....   | 127 |
|       | <b>References</b> .....  | 130 |

UCSF LIBRARY

---

## List of Tables

---

|  |     |
|--|-----|
| TABLE 2-1. SEQUENCE SOFTWARE FEATURES AND CAPABILITIES. ....   | 18  |
| TABLE 3-1. EFFECT OF NUMBER OF MOTION CYCLES ON MEAN PNR.....  | 53  |
| TABLE 3-2. EFFECT OF MOTION CYCLES ON STRAIN WAVELENGTH ESTIMATES.....   | 53  |
| TABLE 3-3. POSTTEST RESULTS FOR THE EFFECT OF ROI ON MEAN STRAIN WAVELENGTH ( $\lambda$ ) ESTIMATE.<br>.....   | 65  |
| TABLE 3-4. STRAIN WAVELENGTH ( $\lambda$ ), WAVE SPEED ( $C_T$ ), AND SHEAR MODULUS (G) ESTIMATES FOR EACH<br>AGAR CONCENTRATION, METHOD, AND NUMBER OF MEGS IN ALL FIVE ROIS COMBINED. .... | 84  |
| TABLE 4-1. SHEAR MODULUS RESULTS FOR DETECTION OF INCLUSIONS EXPERIMENT.....   | 92  |
| TABLE 4-2. T1 AND T2 FOR BOVINE IVD. ....  | 109 |
| TABLE 4-3. EFFECT OF PAPAIN INJECTION ON SHEAR MODULUS, T1 AND T2.....   | 122 |



## List of Figures

|   |    |
|---|----|
| FIGURE 1-1. DYNAMIC RANGE OF SHEAR MODULUS AND PROPERTIES MEASURED BY THE PREDOMINATE IMAGING MODALITIES OF ULTRASOUND, CT, AND MRI (ADAPTED FROM McCracken(6)).    | 3  |
| FIGURE 2-1. ILLUSTRATION OF UNIPOLAR GRADIENT.  | 13 |
| FIGURE 2-2. ILLUSTRATION OF BIPOLAR GRADIENT, A "MOTION ENCODING GRADIENT".   | 13 |
| FIGURE 2-3. PULSE SEQUENCE DIAGRAMS FOR SPIN ECHO (A) AND GRADIENT ECHO (B) ELASTOGRAPHY.   | 16 |
| FIGURE 2-4. PULSE DIAGRAM FOR SPIN ECHO ELASTOGRAPHY SEQUENCE, WITH PULSES LABELED.   | 21 |
| FIGURE 2-5. Z GRADIENT DETAIL OF SPIN ECHO ELASTOGRAPHY SEQUENCE, ILLUSTRATING TIMING VARIABLES.  | 22 |
| FIGURE 2-6. PULSE DIAGRAM FOR SPIN ECHO ELASTOGRAPHY, ABOVE 500 HZ.   | 24 |
| FIGURE 2-7. MOTION ACTUATOR, MOUNTING BRACKET, AND OBJECT FOR SCANNING.   | 25 |
| FIGURE 2-8. PIEZOELECTRIC BENDING ELEMENT.  | 26 |
| FIGURE 2-9. MOTION SIGNAL TIMING AT 500 HZ FOR THE EIGHT OFFSETS BETWEEN THE MOTION AND MOTION-ENCODING GRADIENTS.  | 27 |
| FIGURE 2-10. PHASE DIFFERENCE CALCULATION.  | 31 |
| FIGURE 2-11. PHASE WRAP OF A ONE DIMENSIONAL SIGNAL.  | 33 |
| FIGURE 2-12. SUCCESSFUL PHASE UNWRAPPING WITH ITOH'S METHOD, SNR = 4.   | 36 |
| FIGURE 2-13. UNSUCCESSFUL PHASE UNWRAPPING WITH ITOH'S METHOD, SNR = 4.   | 37 |
| FIGURE 2-14. EXAMPLE OF GOLDSTEIN'S METHOD PHASE UNWRAPPING.  | 39 |
| FIGURE 2-15. EXAMPLE OF QUALITY-GUIDED METHOD PHASE UNWRAPPING.   | 40 |
| FIGURE 2-16. PHASE UNWRAPPING METHOD COMPARISON.  | 41 |
| FIGURE 2-17. RELATION OF SIGNAL, NOISE, AND PHASE FOR PNR CALCULATION.  | 42 |
| FIGURE 2-18. OUTPUT OF DIRECTIONAL FILTER.  | 45 |
| FIGURE 2-19. EFFECT OF DIRECTIONAL FILTER ON LFE INVERSION.   | 45 |
| FIGURE 2-20. PHASE IMAGES AND LINE PROFILES FROM GE SCANNER: PHASE IMAGE (A) AND PHASE FROM REAL AND IMAGINARY IMAGES (B).  | 49 |
| FIGURE 2-21. DETAIL OF PHASE DISTORTION EFFECT FROM "GRAD_WARP" PROCEDURE.  | 50 |
| FIGURE 3-1. COMPARISON OF WAVE IMAGES WITH VARYING NUMBER OF MOTION CYCLES AND ROIS FOR STRAIN WAVE ESTIMATION (NARROW STRIPS) AND PNR CALCULATION (ENTIRE REGION). | 52 |
| FIGURE 3-2. REPRESENTATIVE LINE PROFILES FROM ROI WITH VARYING NUMBER OF MOTION CYCLES.   | 52 |
| FIGURE 3-3. SINUSOIDAL WAVEFORM FREQUENCY AND MAXIMUM SLEW RATE AT DIFFERENT GRADIENT AMPLITUDES.   | 56 |
| FIGURE 3-4. DIGITAL OSCILLOSCOPE SCREENSHOT OF PULSE SEQUENCE WITH TRAPEZOIDAL MEG'S.   | 58 |
| FIGURE 3-5. DIGITAL OSCILLOSCOPE SCREENSHOT OF PULSE SEQUENCE WITH SINUSOIDAL MEG'S.  | 59 |
| FIGURE 3-6. REPRESENTATIVE MAGNITUDE AND PHASE IMAGES FOR TRAPEZOIDAL AND SINUSOIDAL MEG'S.   | 60 |
| FIGURE 3-7. PHASE-TO-NOISE (PNR) RATIO MAPS WITH REGION OF INTEREST FOR MEAN PNR CALCULATION.   | 61 |
| FIGURE 3-8. MEAN PNR FOR SINUSOIDAL AND TRAPEZOIDAL MEGS.   | 62 |
| FIGURE 3-9. REPRESENTATIVE WAVE DIFFERENCE IMAGES WITH ROI'S USED FOR SHEAR WAVELENGTH ESTIMATION.  | 63 |
| FIGURE 3-10. STRAIN WAVELENGTH ESTIMATION PROCEDURE.  | 63 |
| FIGURE 3-11. REPRESENTATIVE COMPARISON OF LINE PROFILES FOR SIN AND TRAP MEG METHODS.   | 65 |
| FIGURE 3-12. EXAMPLE WAVE IMAGES AT HIGH FREQUENCY.   | 67 |
| FIGURE 3-13. PHASE AMPLITUDE FOR STRAIN WAVE AT HIGH FREQUENCIES.   | 67 |
| FIGURE 3-14. ANOVA RESULTS COMPARING MEAN PHASE-TO-NOISE RATIO FOR THE DIFFERENT FREQUENCIES TESTED WITH THE SE METHOD.   | 68 |
| FIGURE 3-15. COMPARISON OF SHEAR WAVE VELOCITY FOR DIFFERENT FREQUENCIES IN 1.0% AGAR WITH THE SE METHOD.   | 69 |
| FIGURE 3-16. COMPARISON OF GRADIENT ECHO AND SPIN ECHO IMAGES   | 72 |

UCSF LIBRARY

|   |     |
|---|-----|
| FIGURE 3-17. REPRESENTATIVE ELASTOGRAPHY IMAGES WITH GRADIENT AND SPIN ECHO METHODS...  | 77  |
| FIGURE 3-18. PULSE DIAGRAM FOR SPIN ECHO-BASED ELASTOGRAPHY SEQUENCE.....   | 80  |
| FIGURE 3-19. PULSE DIAGRAM FOR GRADIENT ECHO-BASED ELASTOGRAPHY SEQUENCE. ....  | 81  |
| FIGURE 3-20. EXAMPLE WAVE IMAGES FOR THE SE (A) AND GRE (B) METHODS AT 500 HZ WITH ROIS<br>FOR STRAIN WAVELENGTH ESTIMATION. ....   | 82  |
| FIGURE 3-21. REPRESENTATIVE WAVE IMAGES WITH ROI LOCATION FOR PNR CALCULATION COMPARING<br>THE SE (A) AND GRE (B) METHODS AT 500 HZ. M, NUMBER OF MEG'S = 15.....                                       | 82  |
| FIGURE 3-22. STRAIN WAVELENGTH ( $\lambda$ ) ESTIMATES FOR THE SE (A) AND GRE (B) METHODS AT 500 HZ<br>IN 1.0% AGAR AND SE (C) AND GRE (D) IN 0.5% AGAR FOR THE FIVE REGIONS OF INTEREST<br>(ROIS)..... | 85  |
| FIGURE 3-23. ANOVA RESULTS COMPARING MEAN PHASE-TO-NOISE RATIO EFFICIENCY FOR THE<br>TECHNIQUES TESTED AT 500 HZ.....   | 86  |
| FIGURE 4-1. MAGNITUDE, DISPLACEMENT AMPLITUDE, AND REPRESENTATIVE WAVE IMAGE FOR AGAR<br>INCLUSIONS.....  | 91  |
| FIGURE 4-2. MAGNITUDE AND SHEAR MODULUS MAPS FOR AGAR INCLUSIONS.....   | 91  |
| FIGURE 4-3. EXAMPLE ROI FOR SHEAR MODULUS MEASUREMENT OF AGAR INCLUSIONS. ....  | 92  |
| FIGURE 4-4. SHEAR MODULUS RESULTS FOR DETECTION OF INCLUSIONS EXPERIMENT.....   | 93  |
| FIGURE 4-5. MAGNITUDE, DISPLACEMENT AMPLITUDE, AND REPRESENTATIVE WAVE IMAGE FOR AGAR<br>INCLUSIONS.....  | 95  |
| FIGURE 4-6. MAGNITUDE AND SHEAR MODULUS MAPS FOR AGAR INCLUSIONS.....   | 96  |
| FIGURE 4-7. EXAMPLE LOAD-DISPLACEMENT CURVE FOR AGAR GEL (1.0%) COMPRESSION TEST. ....  | 99  |
| FIGURE 4-8. SHEAR MODULUS ESTIMATE COMPARISON, LOW CONCENTRATION AGAR.....  | 100 |
| FIGURE 4-9. SHEAR MODULUS ESTIMATE COMPARISON, HIGH CONCENTRATION AGAR.....   | 100 |
| FIGURE 4-10. CYLINDRICAL VIAL CAST FOR AGAR GEL AND REMOVAL. ....   | 101 |
| FIGURE 4-11. REPRESENTATIVE AGAR GEL INCLUSION SHEAR MODULUS DETERMINED BY<br>ELASTOGRAPHY.....   | 103 |
| FIGURE 4-12. REPRESENTATIVE FORCE-DISPLACEMENT DATA FOR AGAR MECHANICAL TESTING. ....   | 104 |
| FIGURE 4-13. SHEAR MODULUS ESTIMATES FROM MECHANICAL TESTING AND ELASTOGRAPHY. ....   | 105 |
| FIGURE 4-14. MEAN SHEAR MODULUS ESTIMATES FROM MECHANICAL TESTING AND ELASTOGRAPHY. ....  | 106 |
| FIGURE 4-15. CORRELATION OF SHEAR MODULUS ESTIMATES FROM MECHANICAL TESTING AND<br>ELASTOGRAPHY.....  | 107 |
| FIGURE 4-16. T1 AND T2 MAPS FOR BOVINE IVD. ....  | 109 |
| FIGURE 4-17. MAGNITUDE, DISPLACEMENT AMPLITUDE, AND REPRESENTATIVE WAVE IMAGE FOR BOVINE<br>CERVICAL IVD. ....  | 111 |
| FIGURE 4-18. MAGNITUDE AND SHEAR MODULUS MAPS FOR BOVINE CERVICAL IVD. ....   | 112 |
| FIGURE 4-19. BOVINE CAUDAL INTERVERTEBRAL DISC.....   | 113 |
| FIGURE 4-20. BOVINE CAUDAL DISC EMBEDDING IN AGAR GEL.....  | 114 |
| FIGURE 4-21. ELASTOGRAPHY OF BOVINE CAUDAL INTERVERTEBRAL DISC. ....  | 115 |
| FIGURE 4-22. SWELLING OF BOVINE NUCLEUS PULPOSUS.....   | 116 |
| FIGURE 4-23. SHEAR MODULUS ESTIMATES IN BOVINE CAUDAL INTERVERTEBRAL DISC.....  | 117 |
| FIGURE 4-24. SWELLING OF NP TISSUE OVER TIME WITH VARYING PEG CONCENTRATION.....  | 118 |
| FIGURE 4-25. FINAL SWELLING AMOUNT FOR INTERVERTEBRAL DISC SAMPLES. ....  | 119 |
| FIGURE 4-26. RELATIVE CHANGE IN T1 OR T2 VERSUS SHEAR MODULUS DUE TO PAPAIN INJECTION. .  | 122 |
| FIGURE 4-27. EFFECT OF SWELLING ON SHEAR MODULUS, T1 AND T2.....  | 124 |
| FIGURE 4-28. EFFECT OF SWELLING ON RELATIVE CHANGE IN SHEAR MODULUS, T1 AND T2 DUE TO<br>PAPAIN INJECTION.....  | 125 |

UCSF LIBRARY

#### 1.1 Background

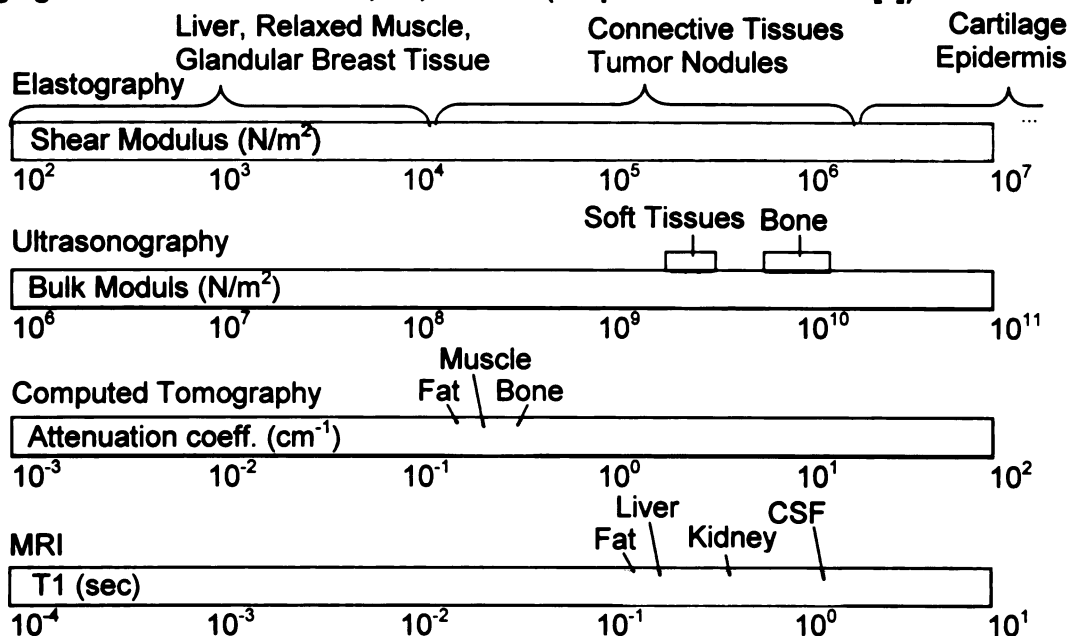
For as long as medicine has been practiced, the use of the sense of touch has played a vital role in evaluation and diagnosis. Changes in tissue stiffness were identified to be related to disease processes such as cancer, and even today the American Cancer Society promotes palpation – either by self-examination or by a health care professional – as a crucial element in the early detection of cancer of the breast, thyroid gland, skin, rectum, testicles, and prostate [1]. Manual palpation has limitations, however, in that the tissue of interest must be accessible and near the surface of the body, and the examiner must rely on qualitative estimates of the tissue stiffness.

Mechanical testing methods for biological tissues have been adopted from traditional material testing methods, for example uniaxial tension or biaxial tension tests, and applied to many tissues of interest, including skin, blood vessels, muscle, bone and cartilage [2]. While these methods have provided a wealth of information into the complex load-stretch response of biological tissues, there remain several difficulties with these methods. Most notably, these methods require meticulous sample preparation which typically requires cutting smaller parts of tissue from a larger organ or tissue sample. For example, in the intervertebral disc, it is common to cut samples from specific regions (for example outer or inner regions) that are oriented either axially or longitudinally to perform testing [3-5]. These methods are therefore destructive to the tissue or organ and define mechanical properties in a piecemeal fashion. Secondly, particular care must be taken to ensure that the methods used to contain or grip the specimen does not contaminate the measured parameters.

While the widespread availability of the latest imaging modalities (ultrasound, computed tomography, magnetic resonance) has allowed unprecedented views into the body to distinguish tissue types and disease states, the dynamic range available in these modalities is dwarfed by the range of the tissue mechanical property of shear modulus [6]. Elastography can be defined as using an imaging modality to non-invasively derived mechanical properties, such as shear modulus. The ranges of measured parameters for different imaging modalities and tissue types are summarized in Figure 1-1. Ultrasound, for example, provides contrast between tissue types via the bulk modulus (a material's resistance to a uniform compression) of the underlying tissues. While bone has a bulk modulus on the order of five times greater than soft tissues, all soft tissues have bulk moduli that are quite similar, ranging only a fraction of an order of magnitude. Shear modulus, on the other hand, has a vastly greater range of values for a variety of soft tissues. The appeal of elastography, therefore, is to capitalize on the dual advantages of the long-standing, high level of specificity for mechanical property changes due to disease, and the inherently large underlying range of mechanical properties that biological tissues display.

UCSF LIBRARY

**Figure 1-1. Dynamic range of shear modulus and properties measured by the predominate imaging modalities of ultrasound, CT, and MRI (adapted from McCracken[6]).**



## 1.2 Elastography literature review

Extensive research has been conducted over the past 15 years to develop and apply elastography methods. Development in the ultrasound field preceded methods in the MR field, but both have enjoyed success. Methods have been applied to biological tissues across the spectrum, in many cases determining tissue mechanical properties in normal and diseased states for the first time. Validation of the elastography method, similar to work presented here, has been completed in both tissue-mimicking objects and biological tissue samples, and continues as research goes forward. Applications continue to be refined and implemented across a range of tissues addressing diseases that continue to plague patients in the US and around the world.

The literature reveals extensive and broad development of elastography methods. In particular, elastography has been most fully developed using either ultrasound or MR imaging. Besides differentiating techniques based on imaging modality, the methods can be separated by loading techniques (quasi-static or dynamic),

UCSF LIBRARY

loading mechanism, measured signal property (magnitude, phase or other signal property), and reconstruction method. In addition to outlining the history of the field, the more recent exciting developments in applications to biological tissues will be summarized. Also, prior research looking to validate the mechanical property measurements made by elastography methods with more traditional, non-image-based, methods will be reviewed.

The development of elastography techniques began in the ultrasound field. A method based on the Doppler effect, originally used for imaging blood flow, was adapted to determine tissue motion under the influence of cyclic compression, and therefore determine mechanical properties [7]. These techniques gave promising results, and were further developed by Lerner [8], Gao [9] and Skovoroda [10]. As an alternative to the Doppler-based method, Ophir and colleagues developed a method of observing the changing locations of tissue interfaces before and after compression by examining the A-lines from ultrasound [11]. An in-depth review of the ultrasound elasticity literature can be found in Gao [12], and a systematic assessment of the progress and challenges in the field has been presented by Parker [13]. More recent developments in the field can be represented by the work of Souchon and colleagues [14].

The ability to image shear strain waves that are driven into an object using a MR imaging system derived from the phase contrast methods developed for imaging blood flow and diffusion [15-18]. The first MR methods were described by Lewa [19, 20] and independently developed and implemented by Muthapillai [21], Fowlkes [22], Sarvazyan [23], and Plewes [24]. The technique described by Muthapillai [25] is unique from the others in that it can be fully described as a dynamic, phase-contrast method. The shear loading is dynamic (usually between 50 and 500 Hz), and the relative displacement or velocity of each image voxel is encoded in the phase of the acquired signal. This is the method adopted in the work presented here. The basic method involves generating

UCSF LIBRARY

cyclic motion in an object that is synchronous with gradients applied by the MR scanner. The result is a stroboscopic representation of shear wave penetration of the object. By combining images of different relative phase between the cyclic motion and imaging gradients, the individual snapshots can be combined to show the transmission of the shear wave through each voxel of the image.

Alternatively, the other methods rely on so-called "quasi-static" loading, which is typically performed at much lower frequencies and generates images that reflect "before" and "after" loading states. The differences in these states are used to derive the mechanical properties of the objects in being imaged. These states can be tracked using "saturation grids" that overlay the unloaded object with a Cartesian grid that is then disrupted when loaded.

A direct comparison of US and MR elastography methods was presented by Dutt and co-workers [26], showing that the resolution achievable with US is not as high as with MR. However, the speed and cost-effectiveness of the US method still make it very attractive for further development and application.

The data collected by elastography methods generally represent a displacement or velocity of the underlying image region. The data is rich and complex, and much effort has been invested in determining reconstruction methods to convert the acquired images into representations of mechanical properties, typically the Young's modulus or shear modulus. Methods have been developed for the dynamic [27-36] and quasi-static [37-40] MR elastography methods that display high performance. While description of all of the methods is beyond the scope of this work, those that have been used in the analysis of acquired images are described in detail in later sections.

The application of determining tissue mechanical properties by elastography has attracted considerable attention due to the potential ability to provide a novel and quantitative contrast mechanism relevant to the detection and tracking of tissue disease.

UCSF LIBRARY

Both *in vivo* and *ex vivo* studies of the mechanical properties of tissues have been undertaken to lead to further understanding of tissue structure and function.

Elastography methods have been applied to a vast array of tissues, with particular focus on detection of tumors or nodules, but with expanding focus as the methods evolve. The work presented here adds to the current literature in elastography by using dynamic MR elastography to examine the mechanical properties of the nucleus pulposus region of the intervertebral disc.

The most developed clinical applications of elastography have focused on detecting and characterizing tumors of the breast and prostate. These cancers are estimated to each cause over 200,000 new cases in the US in the year 2005 [41], the most of any form of cancer. Therefore, the emphasis on bringing new methodologies to aid in detection, diagnosis or treatment tracking is rightly placed. The literature results for breast elastography is extensive [42-49], and recent results have been promising [50, 51] as a method of differentiating benign and malignant tumors. With the relative inaccessibility of the prostate compared to the breast, the studies on prostate elastography have been less widely reported [52-54], but progress shows potential. As new therapies are developed, in particular thermal therapy of the prostate, elastography has been used to track the thermal treatment [55]. This represents a direct measure of the treatment effect, as opposed to using temperature measurements to infer changes in the treated tissues [56-58].

The applications to other tissues includes examining the stiffness change in muscle [59-64] with relaxation and contraction [65-68] and with disease recovery monitoring [69]. The field of intravascular elastography has shown intriguing results for the establishing mechanical properties of plaques in arteries [70-76]. Initial characterizations of tissue mechanical properties using elastography have been shown

UCSF LIBRARY



in the brain [77, 78], heart [79], liver [80], kidney [81], skin[82], heel fat pad [83], and articular cartilage [84].

Investigators in this field undertake a validation step, comparing the mechanical properties found using elastography with traditional mechanical testing methods. Despite the difficulties in direct comparison and unavoidable differences in testing conditions in most cases, the results in general have been favorable. Studies like those presented in this work generally have compared the mechanical properties of gel materials. The gel tests have been with done with traditional compression tests [85], or more sophisticated dynamic testing methods [86-90]. Investigators have produced reliable results comparing the mechanical properties of biological tissue samples [91].

### **1.3 Intervertebral disc degeneration**

For the present work, the nucleus pulposus of the intervertebral disc is investigated as a novel application of elastography methods. The intervertebral disc is a complex structure that both transmits large loads and provides for flexibility of the spine. The disc has three major constituents: water, proteoglycan and collagen [92]. The disc has two identifiable regions, though the transition between the regions is often not crystal clear. The annulus fibrosus is located in the outer ring of the disc, and consists of sheets (or lamellae) of aligned collagen, with the adjacent sheets having alternating angles of alignment of roughly thirty degrees to the transverse plane of the disc [93]. The nucleus pulposus, in contrast, has much higher water content than the annulus, and is often described as “jelly-like” or “fluid-like”, presumed to act as a kind of shock absorber for the vertebral joint. Very little information on the material properties of the nucleus pulposus is available, particularly in regards to changes with aging and degeneration [4].

Extensive work has investigated the role of degeneration of the intervertebral disc on the occurrence of low back pain [3, 4, 93-102]. The complex processes involved generally lead to significant mechanical changes in the cartilage tissue, with degenerative effects causing an increased shear modulus of the nucleus pulposus tissue, by as much as an order of magnitude [4]. As the disc degenerates, gross morphological changes are observed, ranging from minor – such as loss of demarcation between the annulus and nucleus – to major changes – such as loss of nucleus material, disc height, and tears and clefts through the tissue. These changes are categorized in severity by the “Thompson Grading” scheme [103]. Evaluation of the intervertebral disc, and in particular the nucleus pulposus, with MR elastography holds to promise of determining mechanical properties of this complex tissue and its response to degeneration.

#### **1.4 Scope and objectives**

While MR elastography has benefited from over a decade of research by several groups around the world, it is still a relatively uncommon technique. Applying the technique to a specific application involves concerted technical and scientific development. The purpose of the research presented here is to develop strategies for MR elastography of small, stiff tissues on a 3T scanner. The specific outcomes of this work are:

- 1) **Sequence software for elastography based on gradient echo and spin echo techniques. There are three sets of sequence software developed and evaluated. The software includes gradient echo for frequencies up to 500 Hz, spin echo up to 500 Hz, and spin echo for specific frequencies above 500 Hz. Versions of sequence software generally allow robust and extensive modification**

UCSF LIBRARY

of the sequence at run-time on the scanner. For instance, the gradient echo version can alter the elastography parameters controlling the number of motion encoding gradients, their amplitude, and their frequency.

- 2) Experimental hardware for the purposes of elastography consisting of a custom oscillating actuator for use with a power supply and triggered waveform generator.
- 3) Evaluation of elastographic acquisition parameters for the purposes of imaging small, stiff tissues.
- 4) Demonstration of quantitative elastography on agar gel phantoms and ex vivo bovine intervertebral disc tissue.

UCSF LIBRARY

#### 2.1 MR Physics

Magnetic resonance imaging (MRI) is a noninvasive, non-ionizing method that is exquisitely rich in the information it can provide. A brief description of the physics behind the method allows a foundation for understanding the MR elastography (MRE) technique. While the theoretical implementation of MRE requires only a minor change to “traditional” imaging methods, MRE takes advantage of a signal property typically ignored in routine imaging – namely the phase of the acquired signal.

If the nucleus of an atom has an odd number of neutrons, protons, or both, the nucleus will have a net “quantum spin”. Hydrogen, with a single proton in its nucleus, is the typical nucleus of interest for MR imaging. The spin property results in the nucleus having a magnetic dipole behavior, which will respond to strong, external magnetic fields. Hence, MRI requires a large, static magnetic field – referred to as the  $B_0$  field – which is currently commonly achievable at 1.5 Tesla, becoming more common at 3.0 Tesla, and available up to almost 10 Tesla at some research institutions. When an object containing hydrogen molecules (such as water or biological tissues) is placed in this enormous magnetic field, a slight majority of dipoles of the protons align in the same direction of the external field (and the slight minority align in the opposite direction). The alignment of these spins allows a summation of the microscopic nuclear interactions with the magnetic field and applied energy into a macroscopic radiofrequency signal that is detectable by the electronics of the imaging system. This total “spin vector” for a particular signal source, or “voxel”, is referred to as the “magnetization vector”. The three types of magnetic fields that the magnetization vector will interact with are the main field  $B_0$ , the radiofrequency field  $B_1$ , and applied linear gradient fields  $G$  [104]. As

described, the  $B_0$  field has the effect of preparing the spins in a way that they respond in a coherent manner to the next two types of applied magnetic fields,  $B_1$  and  $G$ .

The radiofrequency pulse (rf) field  $B_1$  has the effect of adding energy to the aligned spins. A convenient way to describe this addition of energy is to have the magnetization vector be moved away ("tipped" or "flipped") from its equilibrium position of being aligned with the main  $B_0$  field. As the magnetization vector returns to its equilibrium position, energy is released and signals can be detected that describe the properties of the vector, and hence the chemical environment of the group of spins that compose the magnetization vector.

Two behaviors of the magnetization during its return to equilibrium have been identified as "T1" and "T2". These are time constants which relate the speed at which the magnetization vector recovers its full original alignment with the  $B_0$  field and loses its net magnitude in the plane orthogonal to the  $B_0$  field, respectively. Different physical and chemical environments will alter these time constants, and therefore are the basis of image contrast for MRI. In other words, an imaging method can be devised that accentuates differences in T1 and/or T2 in different tissues such that measurements are made at a point in time when one tissue may have low net signal and another has high net signal.

Images are created by the application of three orthogonal gradients, typically called the "slice selection", "frequency encoding" and "phase encoding" gradients. The sampling of the signal echo is performed in the frequency domain. The typical imaging method is based on the Fourier transform to convert the data between the frequency domain and the image domain. The spacing of the sampling defines the "field of view", or extent of the image in the image domain. The extent of the frequency domain sampling defines the spatial resolution of the image in the image domain.

UCSF LIBRARY

The output of the Fourier transform is a complex number, whose magnitude is typically assigned to each picture element (pixel) of the image. However, the phase of the complex number can also be displayed, but under typical imaging practices will not have additional useful information. However, the development of "velocity encoding" techniques allowed quantitative information about physical motions present in an object to be related in the phase of the image.

## 2.2 Theory of velocity encoding

The effect of motion, particularly due to diffusion, was described in the NMR setting by Carr and Purcell [105]. An early review of the methods for diffusion and flow imaging was done by Singer [16], which includes techniques for charting the phase of each voxel during the evolution of the imaging process. Work by van Dijk [15] applied the flow imaging successfully to cardiac imaging, which required synchronization of the scanning to the cardiac rhythm.

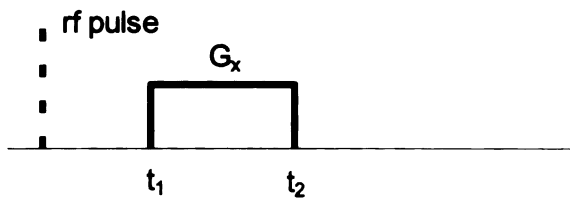
The time-integral of any gradient field times the gyromagnetic ratio of the nuclei will be proportional to the acquired phase of each magnetization vector (or "spin packet" or "spin isochromat"). For a rectangular "unipolar" gradient, the acquired phase is described by

$$\phi = \gamma G_x x (t_2 - t_1) \quad [1]$$

where  $\gamma$  is the gyromagnetic ratio,  $G_x$  is the gradient magnitude in the x-direction,  $x_0$  is the location of the spin isochromat, and  $t_1$  and  $t_2$  are the start and end time of the gradient application, respectively. This is shown graphically in Figure 2-1. If the spin isochromat is stationary, simply substitute  $x = x_0$  into equation 1. For a moving spin that is assumed, for simplicity, to have only a constant velocity,  $x = x_0 + v_x t$ , the relation for the phase becomes

$$\phi = \gamma G_x x_0 (t_2 - t_1) + \frac{\gamma}{2} G_x v_x (t_2^2 - t_1^2). \quad [2]$$

**Figure 2-1. Illustration of unipolar gradient.**



For a bipolar gradient, an equivalent gradient lobe of opposite polarity occurs immediately after the first lobe, as shown in Figure 2-2. Deriving the acquired phase for stationary and moving spin isochromats as before, it is found for stationary spins that

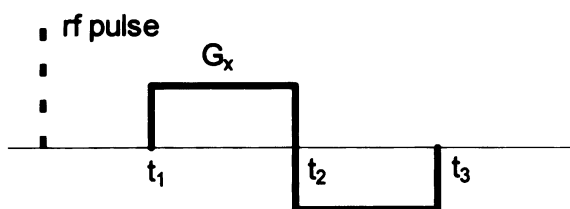
$$\phi_{stationary} = 0 \quad [3]$$

since the integral area of the gradient equals zero. However, for moving spins, the velocity term does not subtract away, leaving the relation

$$\phi_{moving} = \frac{\gamma}{2} G_x v_x (2t_2^2 - t_1^2 - t_3^2). \quad [4]$$

Therefore, at the time of echo, the moving isochromats will have a phase proportional to their velocity. The bipolar gradient can also be referred to as a “motion encoding gradient”.

**Figure 2-2. Illustration of bipolar gradient, a “motion encoding gradient”.**



Denk [18] adapted the method to visualize flow in the cochlea during auditory responses. With these guides providing bases for velocity-dependent phase contrast imaging that is both synchronized (as in cardiac imaging) and at high frequency (as in the cochlea, 2.5 – 4.5 kHz), Muthupillai [21] and co-workers first described the dynamic MRE method, the details of which are described later, particularly in section 3.1.2.

## **2.3 Implementation**

Dynamic MR elastography is accomplished by applying cyclic motion that is phase-locked to motion encoding gradients (MEGs). The implementation of this technique, therefore, involves both software and hardware components. The software modifications required include adding motion encoding gradients to a standard imaging sequence and trigger pulses to synchronize the applied motion signal. The hardware components include the motion actuator, mounting brackets, and driver electronics.

### **2.3.1 Pulse Sequences**

The pulse sequences for gradient echo and spin echo elastography are shown in Figure 2-3. The sequence begins with a trigger signal output within the first 100 microseconds of the repetition time (TR). The trigger commences the motion signal, which is sent to the motion actuator, and is usually set to be the same frequency as the motion encoding gradients (MEGs). The number of cycles of motion,  $N$ , is adjustable according to experimental considerations, but is generally set to start several cycles before the beginning of the MEGs to drive several periods of strain waves into the object before encoding begins. The motion signal ends before or at the same time as the end of the MEGs, as additional motion cycles will not contribute to increased phase modulation once the MEGs are completed.

Both the spin echo and gradient echo sequences begin with an excitation pulse on the RF channel and coincident slice selection gradient. Frequency and phase encoding are done normally, with the addition of MEGs. The MEGs can be played on any of the three imaging axis, but are shown on the slice selection axis. The number of MEGs,  $M$ , is adjustable. For the spin echo method, MEGs are played before and after the 180 degree refocusing pulse. However, since the spins are "flipped" by the 180 degree pulse, the polarity of the MEGs is reversed after the refocusing pulse so that phase modulations due to motion continue to be added to the signal. In this way, the

UCSF LIBRARY



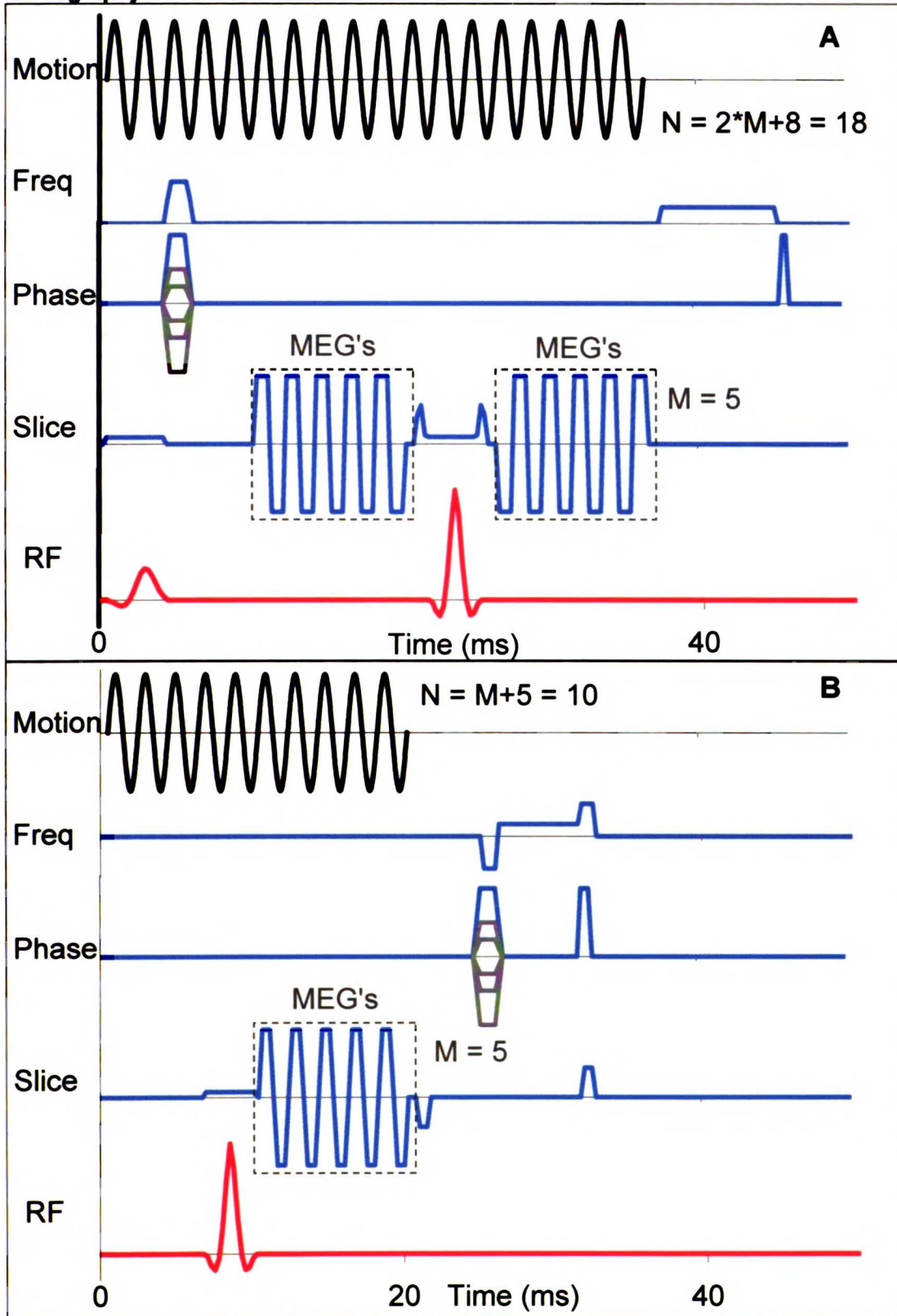
spin echo method produces a single phase image with modulations due to the shear wave motion, or "wave image" that has very little phase background.

For the gradient echo sequence, two repetition times are needed to produce the "wave image", with the MEG polarity reversed for each repetition. The difference of the "positive" and "negative" polarity MEG phase images produces the "wave image".

Figure 2-3B shows only one of the repetition times, with the MEGs having "positive" polarity, for instance.

UCSF LIBRARY

**Figure 2-3. Pulse sequence diagrams for Spin Echo (A) and Gradient Echo (B) elastography.**



UCSF LIBRARY

### **2.3.2 Software**

The strategy of the pulse sequence software development for elastography was to provide adequate flexibility for performing experiments, while limiting the capabilities so that the sequence software development and maintenance was minimized.

Therefore, the pulse sequence was designed to allow specific controls over the motion encoding gradients (MEGs) at the scanner console, to be modified at the time of the experiment. The MEGs could be customized with regard to frequency, number, and amplitude, as well as on which of the three imaging axes the MEGs would be played, and therefore creating phase modulations for motions along that axis.

Elastography pulse sequences were developed from standard, "product", sequences available for the scanner. They were developed in the General Electric-specific language "EPIC", for "Environment Programming in C". In order to allow comparison of echo generation method on the elastography technique, both gradient and spin echo sequences were developed, so that in practice only two sequence code files were finally developed for general application. Further versions of sequences were developed from these base sequences to address specific needs. For instance, a version was created that incorporated sinusoidally-shaped MEGs (as opposed to trapezoidal). Also, for "high frequency" experiments, sequences were written that could execute MEGs above 500 Hz, which required a different strategy compared to the "standard" sequences. The general sequence software capabilities developed are summarized in Table 2-1.

UCSF LIBRARY

**Table 2-1. Sequence software features and capabilities.**

| <b>Feature</b>                    | <b>Range of Capability</b>  |
|-----------------------------------|---|
| Echo generation                   | Gradient and Spin   |
| Motion Encoding Amplitude         | 0 – 4 G/cm  |
| Motion Encoding Axis              | X, Y or Z   |
| Motion Encoding Frequency         | 0 to 500 Hz, inclusive<br>Specific frequencies between 500 Hz and 2000 Hz |
| Number of Motion encoding periods | Unlimited, practical range of 1 to ~20, depending on frequency            |
| Motion Encoding Waveform          | Trapezoidal (with adjustable ramp shape) and Sinusoidal                   |

### **2.3.2.1 Gradient Echo method, 500 Hz and below**

The dynamic elastography method based on gradient echo imaging sequences was first described and validated by the group at the Mayo Clinic [21]. As with normal imaging methods, the advantage of using a gradient echo compared to a spin echo is to achieve a shorter TE. With elastography, the MEGs consume time during the TE, so a compromise must be reached between gaining phase modulation with more MEGs, yet preserving signal by reducing TE. Also, compared to spin echo methods, the underlying phase background varies to a much larger degree, requiring a subtraction strategy to reveal the phase modulations related to voxel motion.

The base code used to develop the gradient echo elastography sequence is "2dfast.e", which is located in the directory "/psd/psd/2dfast/" under the main directory for the development environment (such as "/ESE\_E2M4\_3T/"). The list of changes needed to create an elastography sequence can be summarized as follows, in order of appearance in the software code:

1. Declare, initialize, and calculate CVs ("control variables") to control motion encoding gradients (i.e. "blips") and timing
2. Create blips: "gxu", "gxd", "gyu", "gyd", "gzu", "gzd" according to CVs

UCSF LIBRARY

3. Change calculation of "nreps" since each TR is played two times with blips reversed in polarity
4. Set reconstruction header variables for two times the data and to generate the phase, real and imaginary images
5. Disable "rhhniter", to "disable iterative homodyne recon "
6. Create RSP variables to allow reversing polarity of blips
7. Create trigger pulse to synchronize motion using the "DABOUT6" channel
8. Adjust timing of pulses to create space for blips
9. Change "loadtab" function call due to doubling of acquired data
10. Add a loop in "core(void)" to repeat each TR with blips reversed in polarity

#### **2.3.2.2 Spin Echo method, 500 Hz and below**

The dynamic elastography method based on spin echo imaging sequences was first described and validated by Hamhaber [85]. As with normal imaging methods, the advantage of using a spin echo compared to a gradient echo is to achieve a very homogeneous phase background, as the dephasing of magnetization due to imaging gradients is refocused.

The base code used to develop the spin echo elastography sequence is "memp.e", which is located in the directory "/psd/psd/csmemp/" under the main directory for the development environment (such as "/ESE\_E2M4\_3T/"). The list of changes needed to create an elastography sequence can be summarized as follows, in order of appearance in the software code:

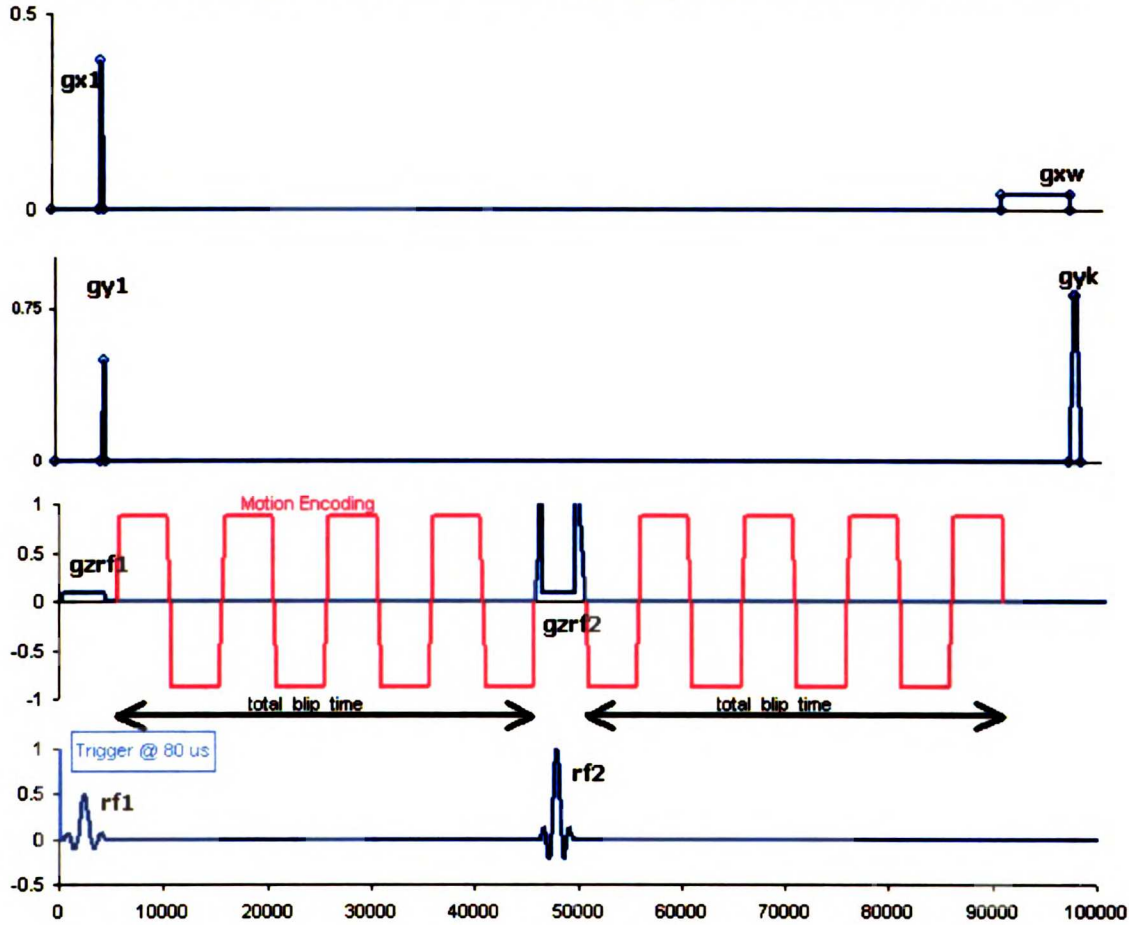
1. Declare, initialize, and calculate CVs ("control variables") to control motion encoding gradients (i.e. "blips") and timing

2. Create blips: "gxu", "gxd", "gyu", "gyd", "gzu", "gzd" according to CVs
3. Create RSP variables to allow reversing polarity of blips
4. Create trigger pulse to synchronize motion using the "DABOUT6" channel
5. Adjust timing of pulses to create space for blips
6. Add motion encoding gradients.
  - a. Allow adjusting frequency, number, amplitude
  - b. Polarity before and after 180 pulse need to be opposite
7. Create trigger pulse to synchronize motion using the "DABOUT6" channel
8. Ensure that time gap for 180 pulse is an integer multiple of mechanical motion period

The changes needed are less than the gradient echo-based sequence due to the fact that the amount of data collected remains the same (whereas the data doubles for the gradient echo sequence due to repeating each TR twice). Therefore, changes to the "loadtab" function call and the loop in the "core" section are not needed.

While the number of changes to the spin echo sequence is less than those for the gradient echo, the spin echo sequence presents a particular challenge for the timing of the MEGs. The MEGs before and after the 180 refocusing pulse must maintain the same phase relationship to the applied motion, and so special care must be taken to adjust the timing accordingly. Figure 2-4 shows the pulse diagram of the spin echo elastography sequence with the non-MEG pulses labeled according to the convention of provided in the "memp.e" source code, and one of the timing variables, "total\_blip\_time", shown.

**Figure 2-4. Pulse diagram for Spin Echo Elastography sequence, with pulses labeled.**

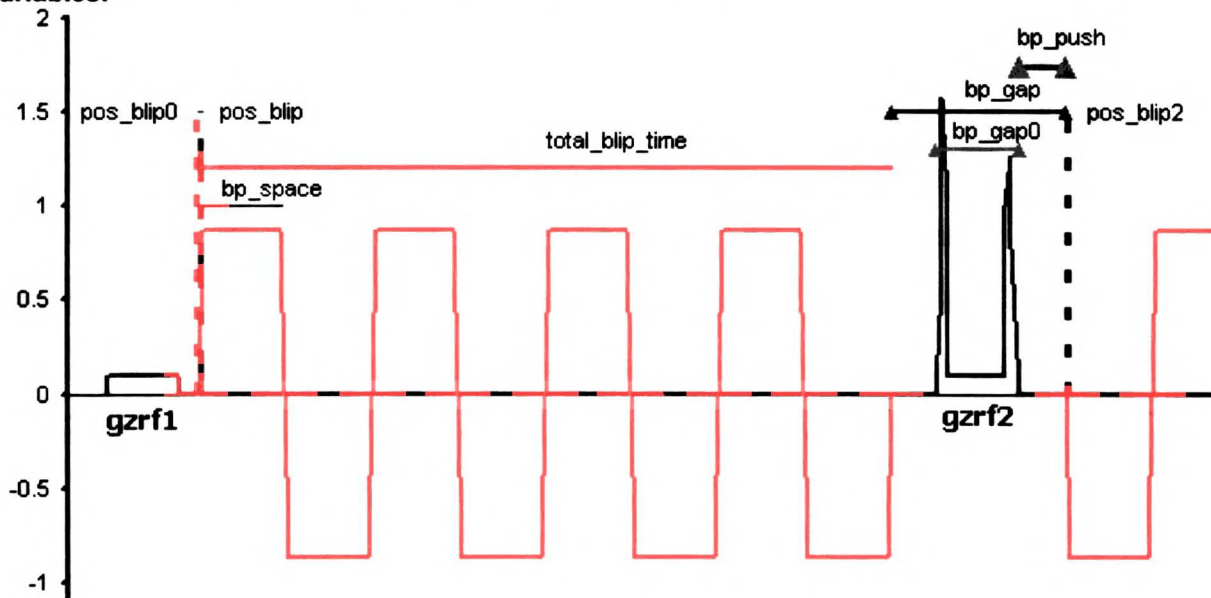


More detail of the timing variables is shown in Figure 2-5. In order to ensure that the relative phase between the motion and both sets of MEGs is maintained, the start time of the first MEGs, "pos\_blip", and the second MEGs, "pos\_blip2", must be exactly a whole integer multiple of the MEG period apart from each other. Another constraint is that the space between the MEGs, "bp\_gap", must be at least the duration of the slice selection gradients associated with the 180 refocusing pulse. This minimum value is determined by finding the time difference between the start of the attack ramp for the crusher gradient before the 180 refocusing pulse ("gzrf211a") and the end of the decay ramp for the crusher after the rf2 pulse ("gzrf2r1d"). This time is defined as "bp\_gap0", and has a value of 4.89 ms. The total time between the MEGs, "bp\_gap" is found by adding to "bp\_gap0" the minimum time needed to create a whole integer number of

UCSF LIBRARY

periods of applied motion. At 500 Hz, the “bp\_gap” value would be 6.0 ms, or three motion periods. One half of the difference of “bp\_gap” and “bp\_gap0” is defined as “bp\_push”, which is used to adjust the timing of the 180 refocusing pulse and the start of the second set of MEGs, “pos\_blip2”.

**Figure 2-5. Z Gradient detail of Spin Echo Elastography Sequence, illustrating timing variables.**



### 2.3.2.3 Spin Echo method, above 500 Hz

With the goal of creating elastographic images of small, stiff tissue, it is necessary to have pulse sequences that can have high frequency MEGs. However, in order to increase the MEG frequency above 500 Hz, it was necessary to take an alternate approach to generate the gradient waveforms. Except for the increase in MEG frequency, the final pulse sequence is identical to the prior spin echo method, as shown in Figure 2-6.

While the MEGs had been generated using the “TRAPEZOID” function in EPIC for frequencies below 500 Hz, when the frequency is set above 500 Hz, an error occurs that describes a timing conflict. In order to avoid this problem, the MEGs were

UCSF LIBRARY

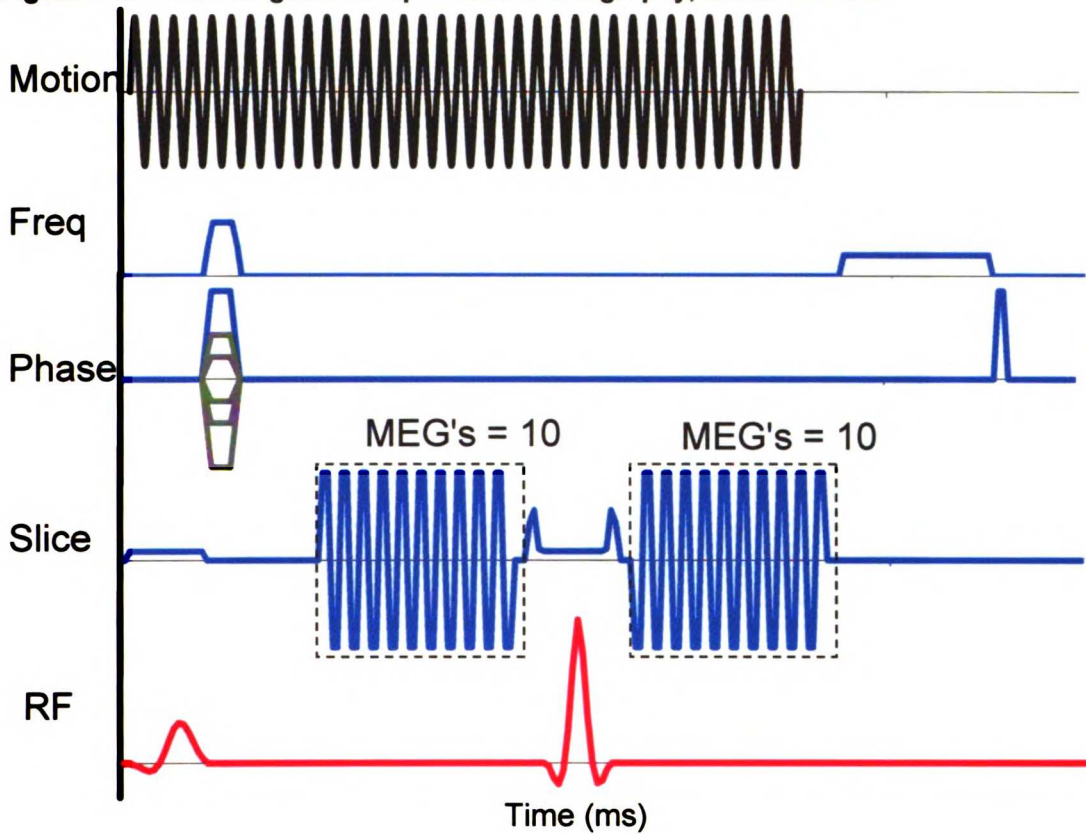


implemented as “external waveforms”, using the “EXTWAVE” function. The list of changes needed to create the elastography sequence from the original spin echo elastography sequence can be summarized as follows:

1. Declare and initialize CVs (“control variables”) to describe the duration and number of points in the external gradient waveforms
2. Replace “TRAPEZOID” commands with “EXTWAVE” commands to create blips
3. Remove RSP variables that allow reversing polarity of blips and logic used to reverse polarity

The external waveforms are stored in files that are read by the sequence, with different files for the “positive” and “negative” polarity MEGs. The frequency is fixed in this implementation, with a different pulse sequence needed for each. However, the number and amplitude of the MEGs is adjustable in each sequence.

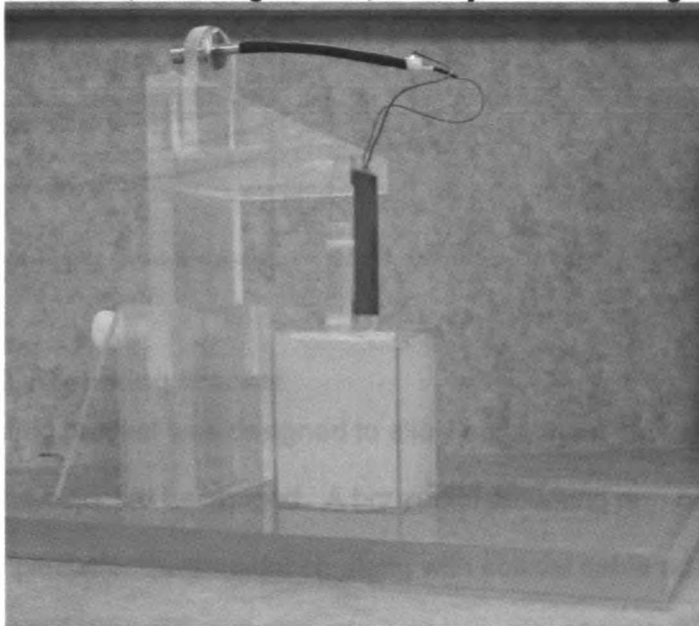
**Figure 2-6. Pulse diagram for Spin Echo elastography, above 500 Hz.**



### 2.3.3 Hardware

To create cyclic shear waves in the object being scanned, specific hardware is needed. The hardware components include the motion actuator, mounting brackets, and driver electronics. A piezoelectric bending element is mounted to an adjustable bracket that allows the contact plate to be placed on the surface of the object to be scanned, shown in Figure 2-7.

**Figure 2-7. Motion actuator, mounting bracket, and object for scanning.**

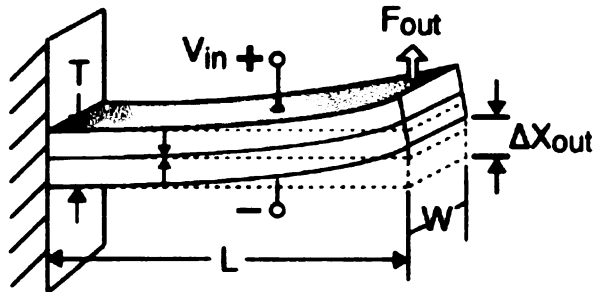


#### **2.3.3.1 Piezoelectric actuator**

Cyclic motion is powered at the surface of the object by a piezoelectric bending element (D220-A4-503YB, “Double Quick-mount Bender, 5A4E, 0.020” T, “503” size, Piezo Systems, Cambridge, MA). It has two layers of piezoelectric crystal, which will change shape due to an applied voltage across the material. The crystal layers are manufactured and electrically wired such that an applied voltage will cause one layer to contract and the opposing layer to expand. This results in a bending action, as shown in Figure 2-8. The device has a length (L) of 2.50 in., width (W) of 1.25 in., and thickness (T) of 0.02 in. It has a reinforcing layer between the piezoelectric layers that is made from non-magnetic material. This device has been evaluated previously [106], which found adequate performance for elastography.

UCSF LIBRARY

**Figure 2-8. Piezoelectric bending element.**



### **2.3.3.2 Mounting bracket**

The mounting bracket was designed to allow adjustment of the height of the contact plate on the object to be imaged. A horizontal mounting arm has taps to allow attachment of the piezoelectric transducer, along with coaxial cable adapter to power the actuator. The horizontal mounting arm is attached to a vertical back that can be raised and lowered inside of a “sleeve” attached to the base. Two plastic thumb screws are used to tighten the mounting arm in place. It is manufactured from acrylic sheets of at least 0.25 in. thick. The entire unit fits within a standard GE head coil during scanning.

### **2.3.3.3 Driving electronics**

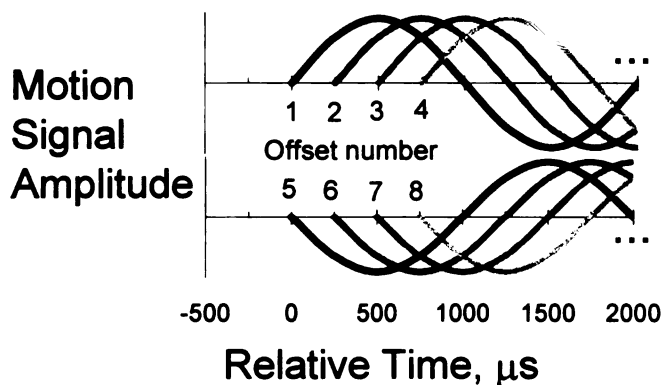
The cyclic motion of the piezoelectric bending element is controlled by an externally triggered, programmable, digital waveform generator (Model 33250A, Agilent, Palo Alto, CA) connected to a high-voltage amplifier (A-303, A.A. Lab Systems, Kennett Square, PA). The synchronization trigger pulse from each repetition time output from the scanner (the “DABOUT6” channel) is connected to the external trigger input of the waveform generator. The waveform generator can be programmed to output a sinusoidal waveform that, for the purposes of elastography, can have adjustments made to initial phase, delay, frequency, number of periods, and amplitude. The initial phase and delay are used to adjust the relative phase between the MEGs and the shear wave motion. Typically, there are four, eight, or sixteen relative phase differences, evenly spaced over the period (or, in some cases, half-period) of the shear motion. An example

UCSF LIBRARY

of eight phase difference offsets over one half-period at 500 Hz is shown in Figure 2-9. Four offsets start with zero initial phases, and four start with an initial phase of 180 degrees.

The number of periods, or cycles, of shear motion signal depends on the desired experimental conditions. However, the number of cycles is typically set to begin several periods before the MEGs, and end at the same time as the MEGs. The frequency is matched to that of the MEGs for the experiment.

**Figure 2-9. Motion signal timing at 500 Hz for the eight offsets between the motion and motion-encoding gradients.**



The output amplitude of the motion signal is amplified by the high voltage amplifier. The high-voltage amplifier is needed due to the high capacitance of the piezo device. The amplifier has a fixed gain of 20, and a bandwidth of 350 kHz. It is capable of driving capacitive loads at up to  $\pm 200$  V at currents up to  $\pm 200$  mA. Typically the waveform generator output is set to 7 V, peak-to-peak, which powers the piezoelectric bending element at 140 V, peak-to-peak.

#### 2.3.4 Sample Preparation

The experiments presented in this work use agarose gels as a tissue-mimicking material for the development and validation of the elastography system. For the study of

biological tissue mechanical properties, ex vivo bovine intervertebral disc tissue was embedded in agarose for elastographic evaluation.

#### **2.3.4.1 Agar gel phantoms**

Agarose has been used extensively as an MR imaging phantom material [107] as well as an elastography phantom material [24]. It has the benefits of being easy to use, non-toxic, and relatively inexpensive. It has low viscoelasticity, which is both a benefit and a challenge. The benefit is that as an almost purely elastic material, it has very good shear wave transmission properties. The challenge, however, of working with agar as an elastography phantom material is that it does not fully represent the difficulties found when performing experiments on actual tissue. The pronounced viscoelasticity of most biological soft tissues poses an additional barrier to driving shear waves of sufficient amplitude into the object of interest to enable estimation of shear moduli. With these limitations in mind, however, agarose provides a good material for development of elastographic methods.

For the experiments presented here that use agarose phantoms, the preparation of the phantom is generally the same. Agarose phantoms have been used with concentrations between 0.5% and 3%. Below this the agarose is too soft to mimic the biological tissues of interest, while above 3% the agarose may not dissolve fully and excessive bubbles tend to be present in the phantom.

All agarose phantoms were made with de-ionized water, normal saline, or phosphate-buffered saline. The phantoms had 0.5 mM Gd-DTPA for additional contrast (1mL of Magnevist® per 100 mL of phantom). The agarose and solvent are stirred together, and put in the microwave until the agarose is fully dissolved (solution becomes clear and begins to boil). The Gd-DTPA is added, the solution is stirred, and it is placed into a vacuum chamber at 20 inches of Hg for approximately 1 minute. The vacuum

UCSF LIBRARY

allows bubbles to rise out of the solution. The phantom is poured into the desired mold and allowed to cool at either room temperature or in the refrigerator. Often the final phantom mold contains two or more layers of agar gel, to provide regions of different stiffness within the same object.

#### **2.3.4.2 Ex vivo tissue samples**

Bovine intervertebral disc specimens were harvested from tissue acquired at a local butcher shop. The tissue was frozen at -80 degrees Celsius for storage, and then thawed before preparation by embedding in agar gel.

In order to properly suspend the tissue in the agar gel, a two-layer technique was developed. One half of the mold was filled with agar solution and allowed to solidify with the lid attached securely and the mold lying on its side. Once the first layer of material solidified, the tissue was placed onto the agar, and additional agar solution was poured into the mold until full. The second agar solution was cooled until just above the freezing point of the gel, approximately 43 degrees Celsius, to minimize any heat-induced tissue changes in the bovine disc material. Once the second layer solidified with the mold on its side, the completed phantom could be stood upright with the disc tissue suspended in the central region of the agar.

## **2.4 Phase image processing**

As described in section 2.2, the application of the bipolar motion encoding gradients creates changes in the phase of the acquired signal from each voxel that relates directly to the cyclic motion the voxels undergo. Since the voxel motion is the transmission of the shear waves in the material, analysis of the shear wave properties provides quantitative information of the shear mechanical properties of the material. In this section, methods for evaluating the quality of the phase information and estimating the shear wavelength are described in detail. For the gradient echo method, the phase

UCSF LIBRARY

difference image must be found for the phase images with opposite polarity of the bipolar gradients. In addition, before phase information can be correctly analyzed, the data must be checked for “wrapping” artifacts, and corrected to the best ability possible.

#### 2.4.1 Phase Difference Calculation

The gradient echo method requires finding the difference of the phase encoded images with opposite bipolar gradients to remove the underlying phase background. The phase difference can be found on a pixel-by-pixel basis, revealing the phase contribution due solely to the velocity of the voxel induced from the transmitted strain wave. The method is straightforward, however, care needs to be taken regarding the order of operations to reveal the optimum difference image [108].

If the same pixel in two images,  $Z_1$  and  $Z_2$  are denoted by the complex values

$$Z_1 = x_1 + iy_1 = \rho_1 e^{i\phi_1} \quad [5]$$

$$Z_2 = x_2 + iy_2 = \rho_2 e^{i\phi_2} \quad [6]$$

then the phase difference can be found by:

$$\Delta\phi = \arctan\left(\frac{y_1}{x_1}\right) - \arctan\left(\frac{y_2}{x_2}\right) = \phi_1 - \phi_2. \quad [7]$$

However, this implementation requires two arctangent operations per pixel. While this is computationally inefficient, worse, it can lead to image artifacts. These artifacts are shown in Figure 2-10. The acquired phase images,  $\phi_1$  and  $\phi_2$ , are shown in

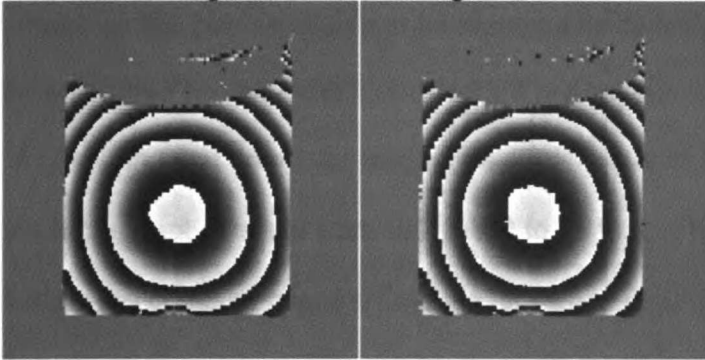
UCSF LIBRARY



**Figure 2-10. Phase difference calculation.**

A – Positive-Negative

B – Negative-Positive



C – Phase Difference

D – Complex Difference

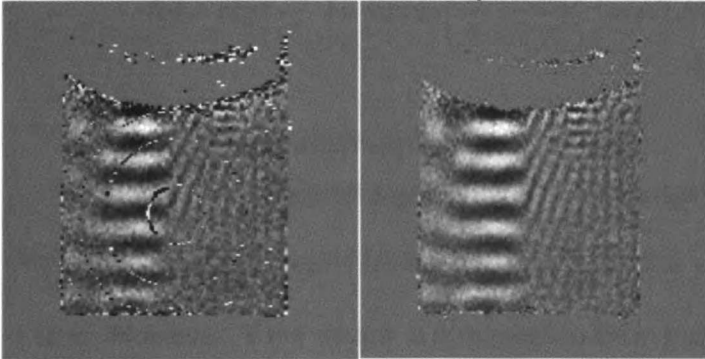


Figure 2-10A and B, while the difference image with two arctangent operations,  $\Delta\phi$ , is shown in Figure 2-10C. Obvious artifacts are present at the phase wrap transitions, or “fringes”. At these locations, the two phase values are very close to the value of  $\pi$  (which is equal to  $-\pi$ ). If the phase values are assumed to be equal, with a small deviation  $\varepsilon$  added or subtracted, an incorrect difference will be found, such as:

$$\Delta\phi = (\pi + \varepsilon) - (\pi + \varepsilon) = (\pi + \varepsilon) - (-\pi + \varepsilon) = 2\pi . \quad [8]$$

This artifact can be removed by recasting the order of operations, and only performing the arctangent procedure once. The phase difference can be computed by the finding the argument of the complex ratio

$$\Delta\phi = \arg\left(\frac{Z_1}{Z_2}\right) = \arctan\left(\frac{\text{Im}(Z_1/Z_2)}{\text{Re}(Z_1/Z_2)}\right) . \quad [9]$$

The complex conjugate and the inverse of the complex number  $Z_2$  have the same phase, so the inverse of  $Z_2$  can be replaced by its conjugate. Also, further artifacts can be prevented by using the four-quadrant arctangent operator, commonly referred to as "ATAN2" in most computer languages. This expands the dynamic range of the output of the arctangent operator from  $-\pi/2$  to  $\pi/2$  to  $-\pi$  to  $\pi$ . Therefore, the final formulation for finding the complex phase difference, shown in Figure 2-10D to have no artifacts, is

$$\Delta\phi = \arg\left(\frac{Z_1}{Z_2}\right) = \arctan\left(\frac{\text{Im}(Z_1 Z_2^*)}{\text{Re}(Z_1 Z_2^*)}\right) = \text{ATAN2}[\text{Im}(Z_1 Z_2^*), \text{Re}(Z_1 Z_2^*)]. \quad [10]$$

#### 2.4.2 Phase unwrapping

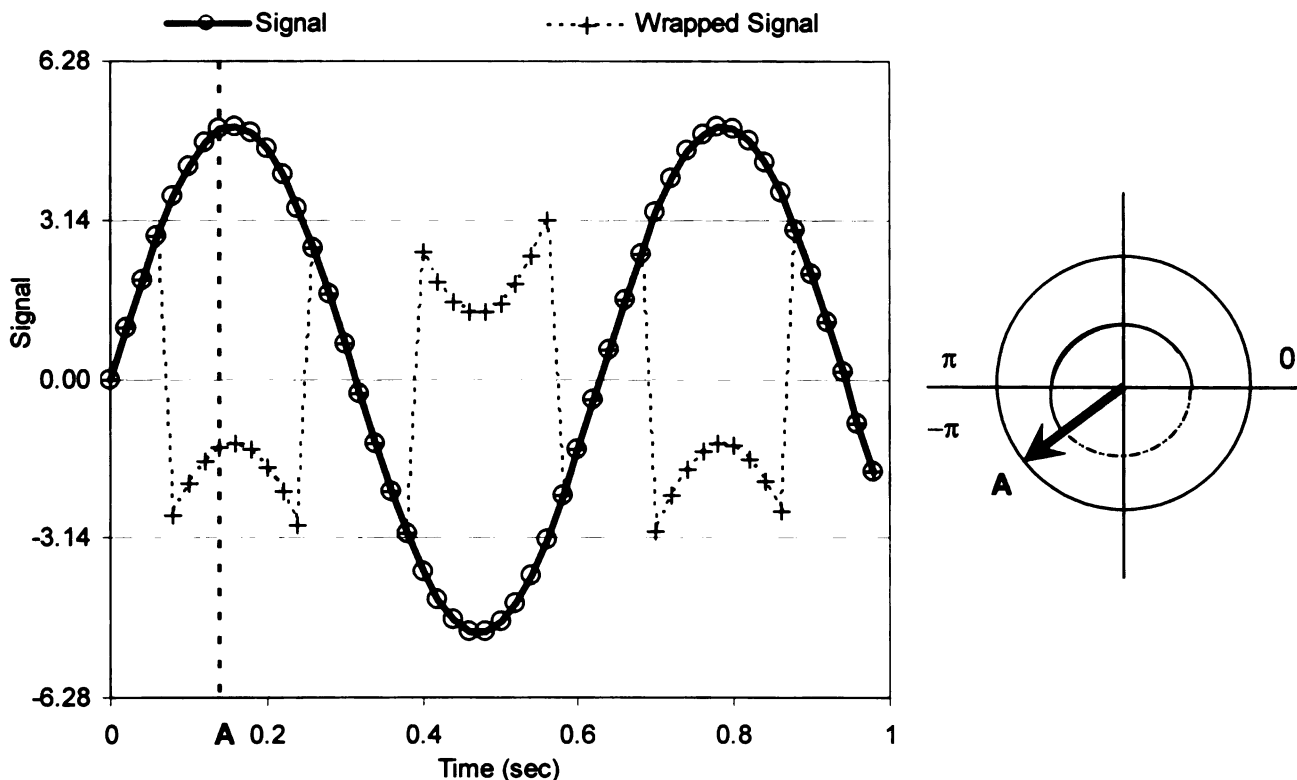
If a one dimensional signal vector is imagined to be normalized onto the unit circle, its phase can clearly be seen to only have the values from 0 to  $2\pi$ , or alternatively,  $-\pi$  to  $\pi$ . However, if the vector is imagined to be in motion, rotating about the unit circle, then the cumulative, or total, phase of the signal can exceed this range once a complete rotation has been completed. In other words, the total phase that a signal acquires is found by knowing not only its current position, but also its route to arrive at the current position relative to some arbitrary starting point. If the route includes at least one full rotation around the unit circle, the accumulated phase is said to have "wrapped" around, leading to "phase wrap". The process of "phase unwrapping" is to determine the total accumulated phase of the signal. Note that the total accumulated phase will always be at least the observed, measured phase plus or minus an integer multiple of  $2\pi$ .

Figure 2-11 shows an example of a wrapped phase signal for the range  $-\pi$  to  $\pi$ . At a particular point, say point "A", the original signal has a value outside the range of  $-\pi$  to  $\pi$ , so the value is wrapped back into the range. An alternate visualization is shown by having the phase mapped onto the unit circle. The actual route of the phase was in the

UCSF LIBRARY

counterclockwise direction (solid line), leading to an actual positive phase value greater than  $\pi$ . However, the wrapped phase value is determined in the range  $-\pi$  to  $\pi$ , which

**Figure 2-11. Phase wrap of a one dimensional signal.**



assumes the shortest, and in this case clockwise, path (dotted line) was traversed. The point on the unit circle 180 degrees from 0, where the phase changes abruptly from  $\pi$  to  $-\pi$  can be called the “phase transition point” or “phase wrap point”. Numerous phase unwrapping algorithms have been developed to remove the spurious phase transitions. The methods detailed here include Itoh’s method, Goldstein’s method, and the quality-guided method.

#### 2.4.2.1 Itoh’s method

A concise algorithm for directly unwrapping a series of phase measurements was presented by Itoh [109]. He described how the original phase values can be recovered by a simple three-step process of differentiating, wrapping, and integrating. However, the limitation is that the process breaks down if the absolute value of the change in

UCSF LIBRARY

consecutive underlying phase measurements is greater than  $\pi$ , either due to noise, undersampling, or both.

Itoh's method is instructive for later methods, in that it introduces the basic techniques used to identify, and correct, phase wrap transitions. The presentation will review Itoh's original formulation, along with a description of an implementation that can be done on a spreadsheet.

Itoh describes a differentiating operator,  $\Delta$ , and a wrapping operator,  $\Phi$ . The differentiating operator is defined as

$$\Delta s(n) = s(n) - s(n-1) \quad (n = 0, 1, \dots, N). \quad [11]$$

where  $s(n)$  is the sequence of measured (and therefore wrapped) phase values. The wrapping operator is defined as

$$\Phi_l s(n) = s(n) + 2\pi k_l(n) \quad (n = 0, 1, \dots, N), \quad [12]$$

where  $l$ , is a label, and  $k_l$  is a sequence of integers such that

$$-\pi < \Phi_l s(n) < \pi \quad (n = 0, 1, \dots, N). \quad [13]$$

In terms of implementation, the sequence  $k$  must be determined, which Itoh does not explicitly describe. The value of  $k$  indicates the number and direction of phase wraps necessary to bring the original signal into the measured range of  $-\pi$  to  $\pi$ . The  $k$  sequence can be found by

$$k_l(n) = \text{int}\left(\frac{\Delta s(n)}{\pi}\right) - \text{int}\left(\frac{\Delta s(n)}{2\pi}\right) \quad (n = 0, 1, \dots, N) \quad [14]$$

where  $\text{int}(\dots)$  returns the integer part of the argument. Therefore, given the measured, wrapped phase sequence  $\Phi_l s(n)$ , the unwrapped sequence can be recovered with

$$s(m) = s(0) + \sum_{n=1}^m \Phi_2 \Delta \Phi_1 s(n). \quad [15]$$

Equation 15 reveals the simple elegance of the method. The unwrapped signal,  $s(m)$ , can be recovered from the wrapped measured signal  $\phi_1 s(n)$ , by simply taking the difference ( $\Delta$ ), wrapping the result ( $\phi_2$ ) and finding the cumulative sum.

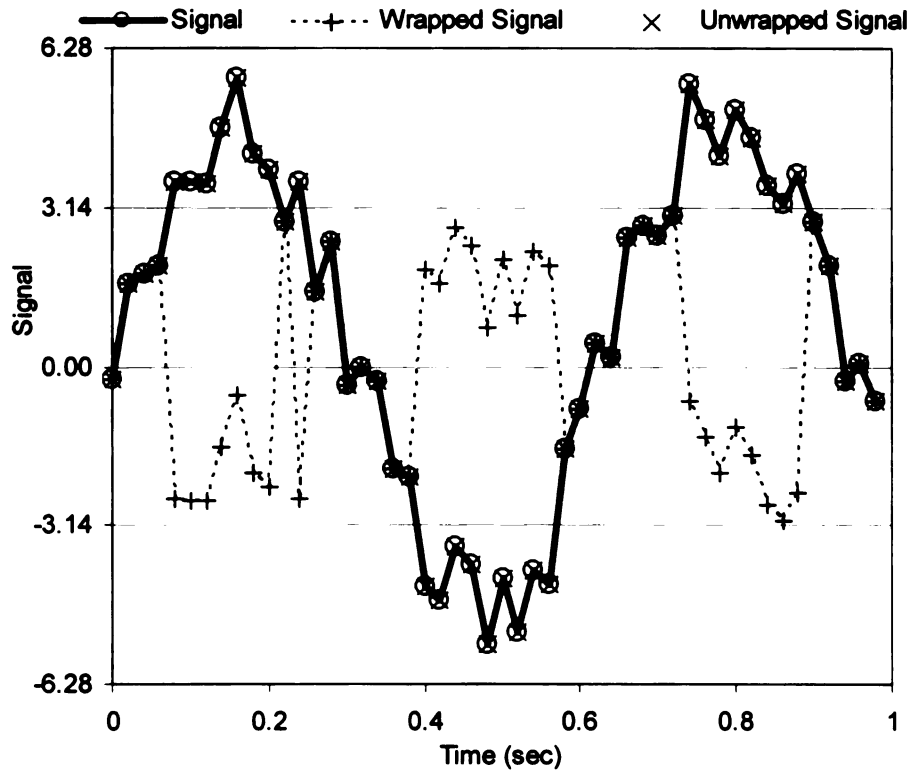
This method is robust in the presence of noise up to the point that the condition

$$-\pi \leq \Delta s(n) < \pi \quad [16]$$

is not violated. In practice this relates to an SNR of approximately four, assuming the sampling frequency is sufficient to prevent aliasing. A successful phase unwrapping is shown in Figure 2-12. If the noise causes a signal change that is greater than  $\pi$  or less than  $-\pi$ , then incorrect phase unwrapping will occur, as shown in Figure 2-13. In this case the second-to-last signal change has a value of  $-1.06\pi$ , thus the last two phase values are incorrectly assigned to be  $2\pi$  greater than the actual values.

UCSF LIBRARY

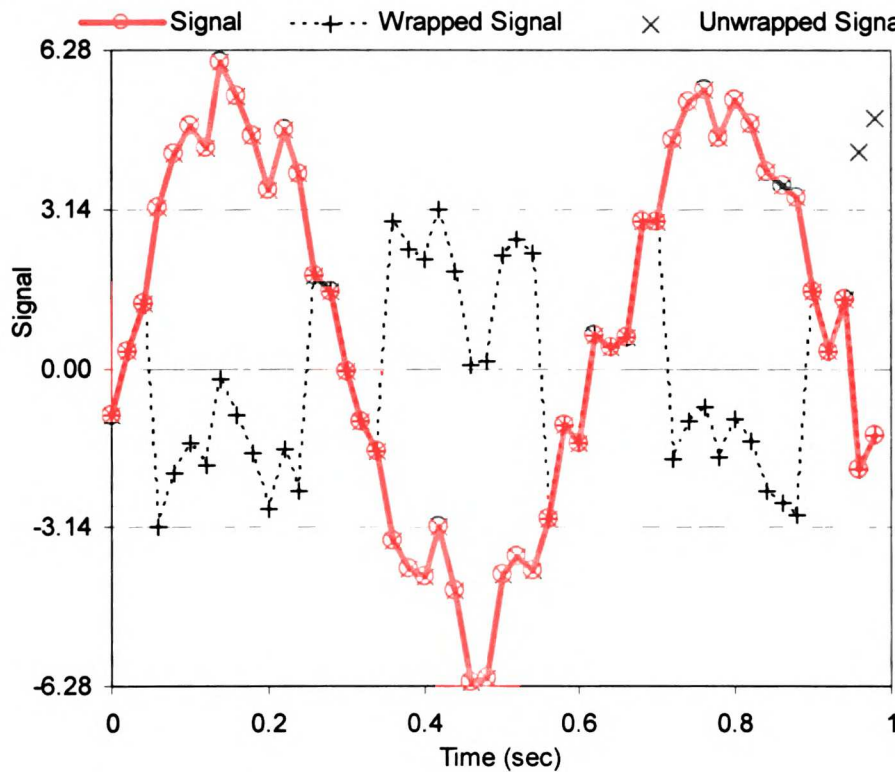
**Figure 2-12. Successful phase unwrapping with Itoh's method, SNR = 4.**



Itoh's method can be applied in 2D, by applying the method to the rows and then columns of the 2D matrix (or columns followed by rows). This method is available in Matlab with the "unwrap" function. However there are other, more sophisticated methods suited for 2D phase unwrapping that perform well with noisy phase measurements. These methods include Goldstein's method and the quality-guided method.

UCSF LIBRARY

**Figure 2-13. Unsuccessful phase unwrapping with Itoh's method, SNR = 4.**



#### **2.4.2.2 Background of path-following phase unwrapping methods**

The basic steps of Itoh's method – differentiate, wrap, and integrate – breaks down in the presence of noise. The process of identifying large phase changes as wrap locations, and adjusting the phase accordingly, becomes “path dependent”. In the ideal case, choosing a path through a 2D image, the integral of the phase around the path will be zero, so adjustments are made to the phase to result in a zero path integral. However, noise will cause cases where the phase value at a particular pixel will be calculated differently depending on the path chosen to arrive at that location, thus “path dependence”. The strategy of path following methods is to restrict the paths chosen for the unwrapping process that results in the remaining paths to be “path independent”, and thus no inconsistencies in phase corrected values will be computed.

UCSF LIBRARY

The path-following algorithms, referred to as "Goldstein's method" and the "quality-guided method" [110] use different methods to limit the available paths for the unwrapping process. Source code for these algorithms were obtained from [110] and adapted into image processing steps with Matlab. Goldstein's method identifies so-called "residues", and from these determines "branch cuts" which act as roadblocks to the unwrapping paths. The quality-guided method estimates "bad" pixels by calculating the local variance of the wrapped phase values, and avoids these in the unwrapping paths.

#### **2.4.2.3 Goldstein's Method**

The fundamental processes for Goldstein's method of phase unwrapping is to identify "residues", which then guide the placement of "branch cuts", which phase unwrapping paths cannot cross. A residue is found at the center of a 2x2 pixel loop (the smallest loop possible) that has a non-zero line integral result, but either  $2\pi$  or  $-2\pi$ . The loop integral is calculated in the counter-clockwise direction by convention, and the "polarity" of the residue is the sign of the integral result. If branch cuts are placed which connect residues of opposite polarity, then all remaining unwrapping paths will be "path independent", and any unwrapping path will succeed. Hence, Goldstein's algorithm attempts to optimize the branch cut placement.

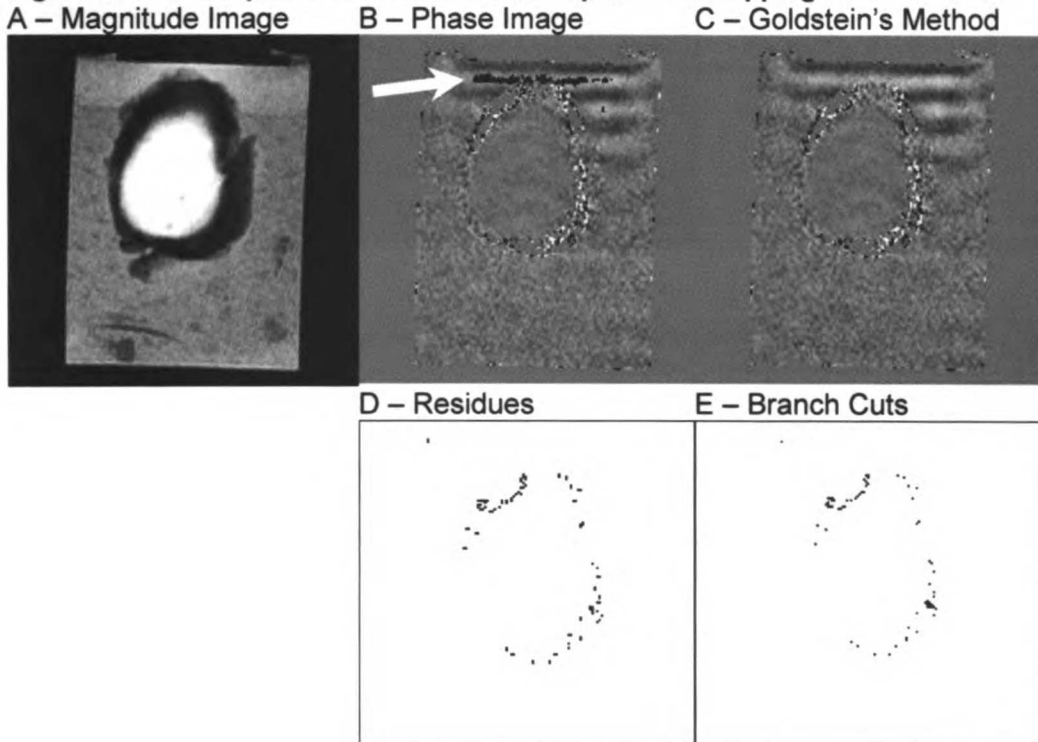
The branch cut placement is not trivial. The guiding requirements are to minimize the total length of all the branch cuts, and to prevent isolating regions in the image. If a region or regions are isolated, there will be no reference to how the phase values transition between regions, and hence the image will not be fully unwrapped.

An example of the results of using Goldstein's algorithm is shown in Figure 2-14. The phase wrap region in the original phase image, highlighted by the arrow, is removed in the unwrapped image, Figure 2-14C. The residues and resulting branch cuts (Figure



2-14D and E) show the concentration in the noisy region of the annulus. These areas will prove to be problematic, and the source of phase correction errors, for Itoh's method.

**Figure 2-14. Example of Goldstein's method phase unwrapping.**

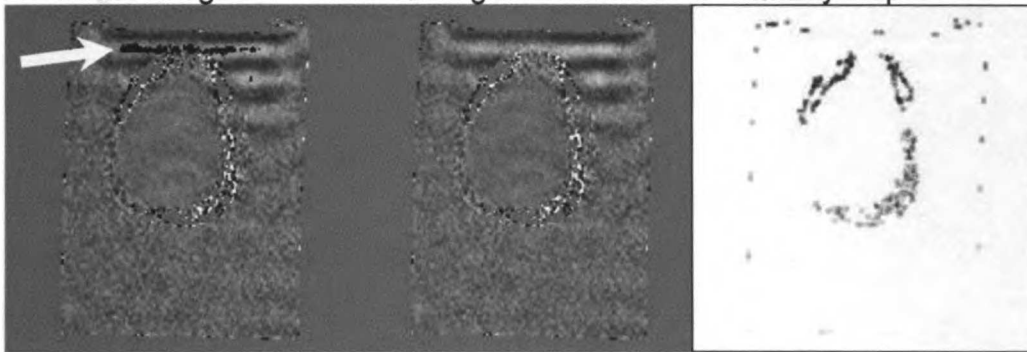


#### 2.4.2.4 Quality-guided Method

An alternative path-following phase unwrapping method is the "quality-guided" method. The basic approach to the quality-guided method, as the name implies, is to determine a measure of "quality" or "goodness" of the phase values, and exclude those that appear exceedingly noisy. In theory, any number of measures may be used to assess phase measurement quality. For the purposes here, however, a measure of phase derivative variance was used. The measure is a root-mean-square measure of the variances of the partial derivatives in the x and y directions over a 3 x 3 window. An example of the quality-guided unwrapping algorithm and the quality map used to mask the unwrapping path is shown in Figure 2-15.

UCSF LIBRARY

**Figure 2-15. Example of quality-guided method phase unwrapping.**  
A – Phase Image      B–Qual.-guided method      C – Quality map



Other phase unwrapping methods have been investigated, including Flynn's minimum discontinuity method and the Lp-norm methods [110]. While very satisfactory results have been found with these methods, the Goldstein's and Quality-guided methods gave equivalent results in much less computational time, up to ten times faster in some cases.

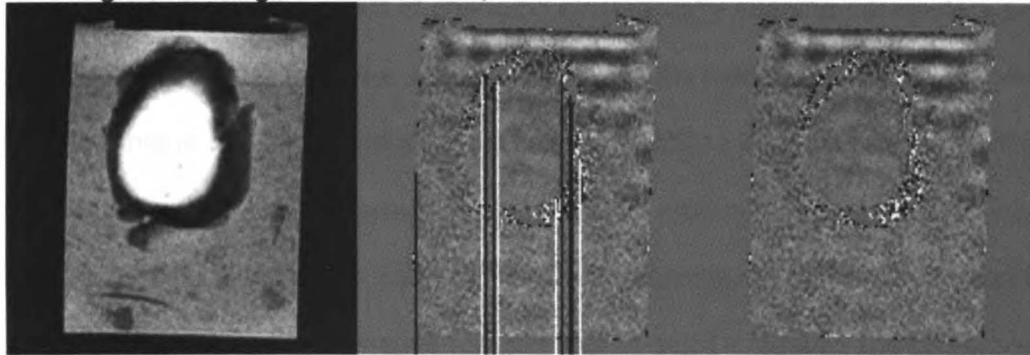
#### **2.4.2.5 Phase unwrapping comparison**

The phase unwrapping algorithms were applied to a bovine intervertebral disc specimen embedded in 1.0% agar. The magnitude and phase images are shown in Figure 2-16A and Figure 2-16B, with a region of phase wrap indicated by the arrow. The phase wrap region is in the first peak of the shear wave that is emanating from the top surface of the object.

UCSF LIBRARY

**Figure 2-16. Phase unwrapping method comparison.**

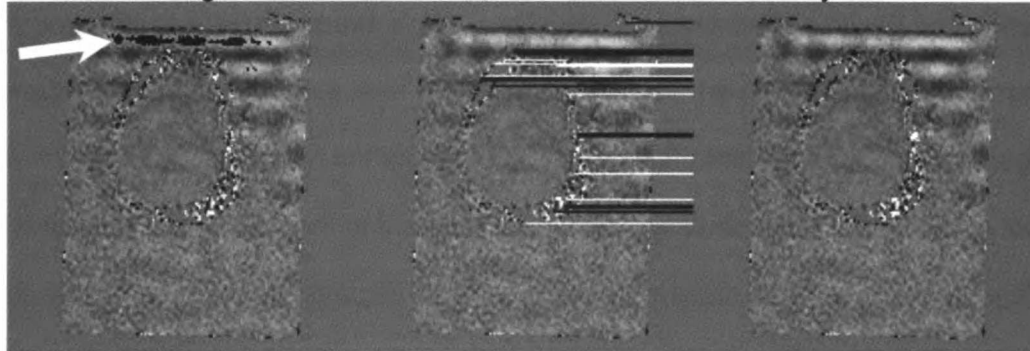
A – Magnitude Image    C – Itoh's, column-wise    E – Goldstein's Method



B – Phase Image

D – Itoh's, row-wise

F – Quality-Guided



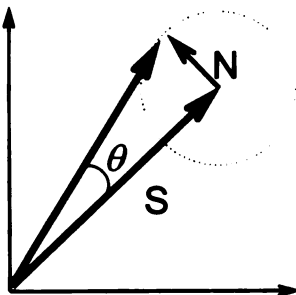
In the annular region of the disc there is very low signal, which results in noise in the phase image. This noisy region presents a challenge to the phase unwrapping algorithms. If Itoh's method is applied to the image, either down the columns or across the rows (or both, in series), a single incorrectly identified phase transition due to noise disrupts the entire column or row. The phase wrap region is corrected; however, the noise creates obvious "streaking" artifacts, as shown in Figure 2-16C and Figure 2-16D. Both Goldstein's and the quality-guided methods successfully unwrap the image, with no evidence of artifacts, as shown in Figure 2-16E and Figure 2-16F. Further tests comparing these methods found very few differences between them, including execution time. Cases were found that defeat the one method and not the other, but no systematic preference could be determined. Hence having both methods provides the ability to unwrap nearly all cases found in experiments to date.

UCSF LIBRARY

### 2.4.3 Phase to noise ratio

To compare the effect of changing elastography imaging parameters on the ability to encode shear waves, a phase-to-noise ratio measurement can be performed. This technique directly assesses the efficiency of phase encoding by the particular elastography method, and provides a quantitative method of comparing techniques. To calculate PNR, an absolute maximum intensity projection is performed across the available wave difference images (usually four or eight images). The projection image represents the largest phase signal available. To estimate the phase noise, the magnitude signal to noise ratio (SNR) is used, since the phase estimation error is related to the SNR as illustrated in Figure 2-17. To calculate PNR, the projection image is divided by the arctangent of the inverse of the magnitude SNR. The SNR is found by dividing the magnitude images by the standard deviation of the signal in a region of air for each offset acquired, and averaging across the offsets. The distribution of PNR values in comparable regions of interest (ROIs) can be compared between the elastography techniques by analysis of variance (ANOVA).

Figure 2-17. Relation of signal, noise, and phase for PNR calculation.



### 2.4.4 Strain wavelength estimation

While PNR comparisons are beneficial for evaluating different elastography techniques, the actual measure of interest is the transmitted shear wave. For several experiments to be presented, the strain wavelength is estimated by using an ROI similar to that used to calculate the mean PNR, yet further divided into vertical columns five voxels wide. For each ROI, the median phase signal was found along its length. The

UCSF LIBRARY

UCSF LIBRARY

median phase signal along the length of the ROI (and direction of propagation of the shear wave) was zero-filled by a factor of 20, and the frequency power spectrum was calculated by the Fourier transform. The maximum of the power spectrum in the spatial frequency range corresponding to wavelengths of 0 to 2 cm was chosen as the characteristic shear wavelength ( $\lambda$ ) for the ROI. This method provides a basic measure of shear stiffness for large, homogeneous objects that contain several strain wavelengths. In order to calculate more spatially precise shear modulus estimates, a direction filtering procedure is done before either a "local frequency estimation" procedure or a "direct inversion" procedure. Both result in voxel-sized estimates of shear modulus in the image.

#### **2.4.5 Directional Filtering**

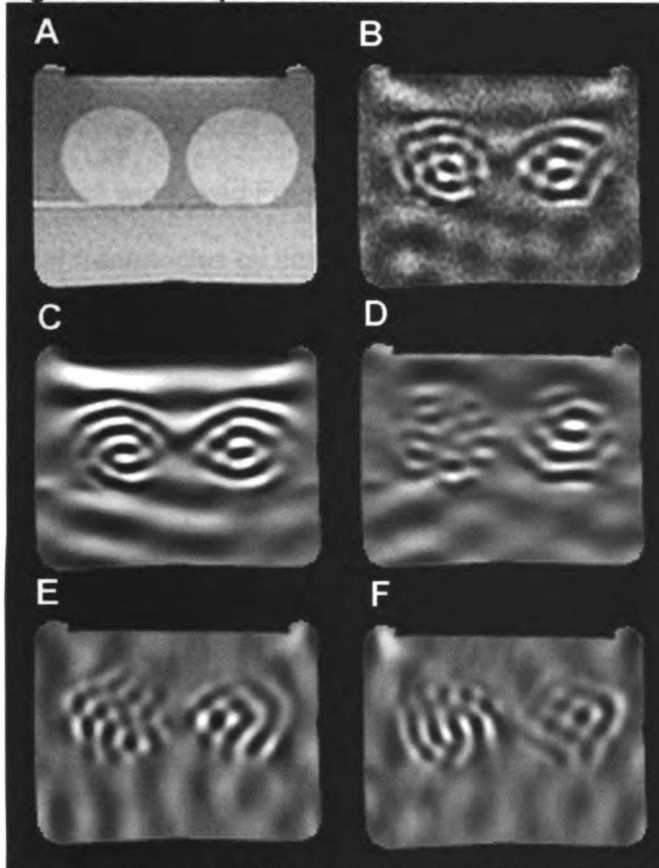
Work by Manduca [27] provides a directional filtering preprocessing method for improving the inversion of wave images into shear modulus maps. In particular, inversion techniques can be sensitive to areas of low motion amplitude due to wave interference from reflections and refractions in the object. The local frequency estimation (LFE) technique, to be used in the present work, can be susceptible to these problems. The approach, therefore, is to directional filter the wave images to attempt to remove some of the interference patterns, individually invert the set of filtered images, and then combine these inversions into a final estimate.

The filters are described briefly here, and examples of their action are shown. The filters are a product of spatially directional and radial components. The radial components of the filters are Butterworth bandpass filters that remove very low and very high frequencies. This improves the image since low frequencies typically arise from unwanted bulk motion or longitudinal wave propagation, while high frequencies typically contain noise. The implementation used in this work is to have four orthogonal filters, in

the “up-down”, “down-up”, “left-right” and “right-left” directions. An example is shown in Figure 2-18. The original phase difference image is shown in Figure 2-18B, with noticeable speckling due to noise. The four directional filter output images in Figure 2-18C-F shows the effective removal of the high frequency noise, and the separation of the waves traveling in different directions. The downward wave has the highest amplitude, since this is the input wave to the object from the contact plate at the top. Significant wave focusing is seen in the cylindrical inclusions that are less stiff than the surrounding material.

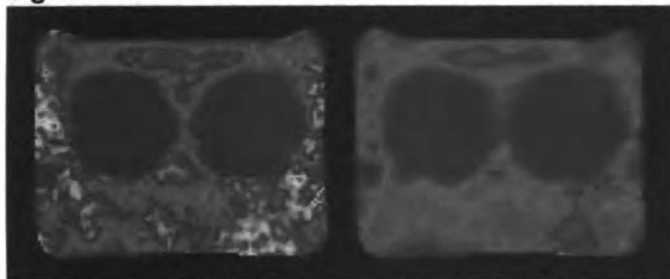
The effectiveness of the directional filtering on the local frequency estimation inversion technique (“LFE”, see section 2.4.6) can be seen in Figure 2-19. The filtering removes a sizable amount of noise and inhomogeneity in the shear modulus map without sacrificing spatially significant features, such as edges of the inclusions.

Figure 2-18. Output of directional filter.



A – Magnitude, B – Phase difference, C – Downward wave, D – Upward wave, E – Rightward wave, F – Leftward wave. Images C to F are at the same window and level.

Figure 2-19. Effect of directional filter on LFE inversion.



Shear modulus images with no direction filter (left) and four orthogonal directional filters (right). The images are windowed from 0 to 60 kPa.

#### 2.4.6 Local Frequency Estimation (LFE)

The “local frequency estimation” (LFE) technique introduced by Knutsson [111] was adapted to the MR elastography problem by Manduca [112]. As opposed to determining a regional shear stiffness estimate in a homogeneous region as described in section 2.4.4, the LFE approach allows estimating the shear wavelength at each voxel

given several wave images with different relative phase between the applied motion and motion encoding gradients

As opposed to the more well-known approaches of estimating frequency locally, such as windowed Fourier transforms and Gabor transforms, the LFE method estimates local frequencies by combining estimates over a large number of scales. The filter can be described as a lognormal quadrature wavelet that is a product of radial and directional components. By summing the output of orthogonally-oriented filters at one scale, an estimate of signal strength is found. In addition, the ratio of the output magnitude between two filters at different scales can be used to find an estimate of instantaneous frequency. In practice, the range of the filters is set wide to include all potential spatial frequencies, and then a weighted sum is calculated corresponding to the strength of the signal that each filter encounters. Once the estimate of instantaneous frequency is found, or rather, its inverse of instantaneous wavelength, then an estimate of shear modulus may be computed from  $f^2 \lambda^2 \rho$ , where  $f$  is the excitation frequency,  $\lambda$  is the instantaneous wavelength, and  $\rho$  is the material density. The density is assumed to be equal to water for tissues and tissue-equivalent phantom materials.

#### **2.4.7 Direct Inversion (DI)**

A second inversion technique used in this work was developed by Oliphant [31]. Named the "Algebraic Inversion of the Differential Equation" (AIDE) or "Direct Inversion" (DI), the technique models the equations of motion that are experienced in a MRE experiment and solves for the material parameters. In a comprehensive comparison of reconstruction methods by Manduca [29], the DI method was found to create sharper shear modulus estimates at interfaces compared to the LFE method. However, the DI method is more susceptible to regions of low shear wave amplitude, resulting in typically



more artifacts than the LFE method. In this work, the DI method will always be used only in conjunction with the LFE method to allow a comparison and double-check of the LFE results.

#### **2.4.8 Phase Image acquisition on a GE scanner**

The elastography method described in this work uses information encoded in the phase of the magnetization vector in the spatial domain. This section describes the details of properly acquiring the phase information from the GE scanner.

The GE MR scanner will normally reconstruct and save only the spatial domain magnitude image; however it can be adjusted to reconstruct the phase, real and imaginary images as well. This is accomplished with the variable “rhrctrl”, which is a 5-bit, bit-wise flag variable. The most significant bit is always 1, while the four least significant bits control which of the four spatial domain images are reconstructed. The order of the flags is, from least to most significant, magnitude, phase, real, imaginary. In practice, then, “rhrctrl” has a value of 17 to reconstruct only the magnitude image. If the phase image is also wanted, the value is 19, and “rhrctrl = 31” will reconstruct all four images.

The obvious choice, for elastography, then, is to have the scanner reconstruct the magnitude and phase images only. The first challenge with this approach, however, is to decipher how the signed, integer dynamic range of the phase values is related to the actual phase dynamic range from negative  $\pi$  to positive  $\pi$ . By first approximation, a factor of ten thousand would scale values in the range of  $-\pi$  to  $\pi$  to just under -32767 to 32767, for a 16-bit dynamic range. However, the phase is expected to “wrap” at the values of  $\pi$  and  $-\pi$ , the phase images qualitatively appeared to be wrapping at approximate 3,276 and -3,276, or by scaling by one thousand. Detailed analysis of the phase images revealed while it would be expected that, no matter the value of the

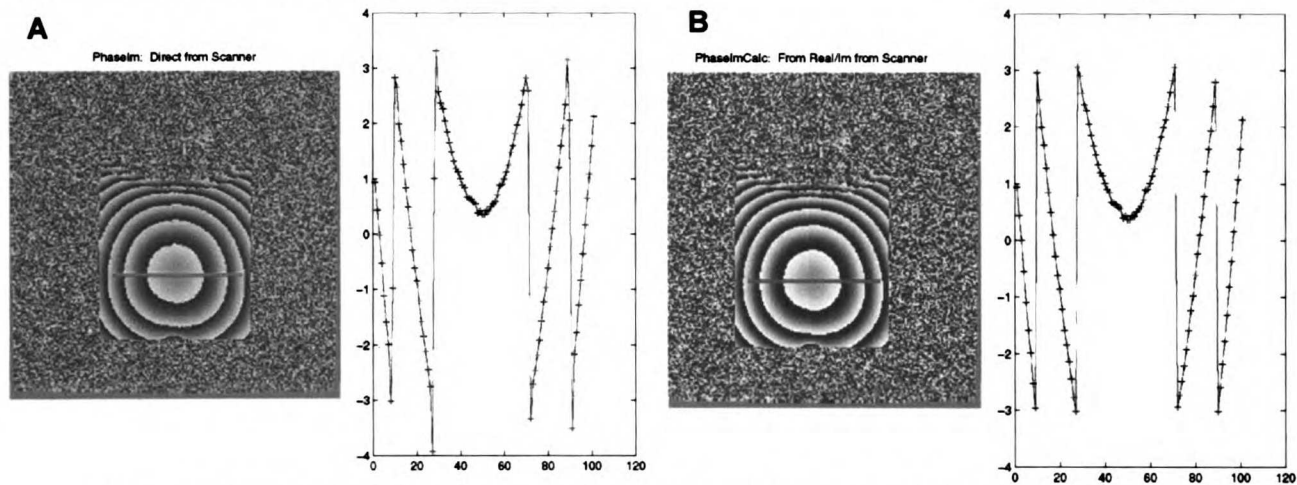
conversion factor, the presence of noise over the full dynamic range of phase values should result in absolute maximum values near  $\pi$ , where wrap should occur. Despite this logic, it was found that quite a bit of scatter of the maximum and minimum values found in the images. So the question existed, how are the expected “wrap values” of  $\pi$  and  $-\pi$  not consistent though the image?

To address this question, an experiment was done with the gradient echo elastography sequence, which shows extensive phase wrap of the background phase. In the experiment, all of the spatial domain images were collected, and the phase image from the scanner was compared to the phase image derived from the real and imaginary images, using the relation:

$$\phi = \arctan \frac{\text{Im}}{\text{Re}} \quad [17]$$

The resulting images and a representative line profile are shown in Figure 2-20. Using the results of the experiment, it was found that the conversion the GE uses to store the phase values is to multiply by the factor  $(\pi/32767)*10$ , which is just less than  $1/1000$ , approximately 0.0009588. This factor produces excellent agreement on almost all phase values. However, it was obvious from the results that some sort of blurring was occurring at the phase wrap transitions, as shown in the detail of the comparison of the line profiles in Figure 2-21. Rather than a single-point phase wrap transition from  $-\pi$  to  $\pi$ , as shown in the “PhaseCalc” series (derived from the real and imaginary images), the phase image reconstructed by the scanner has a three, and sometimes four, pixel “transition zone”.

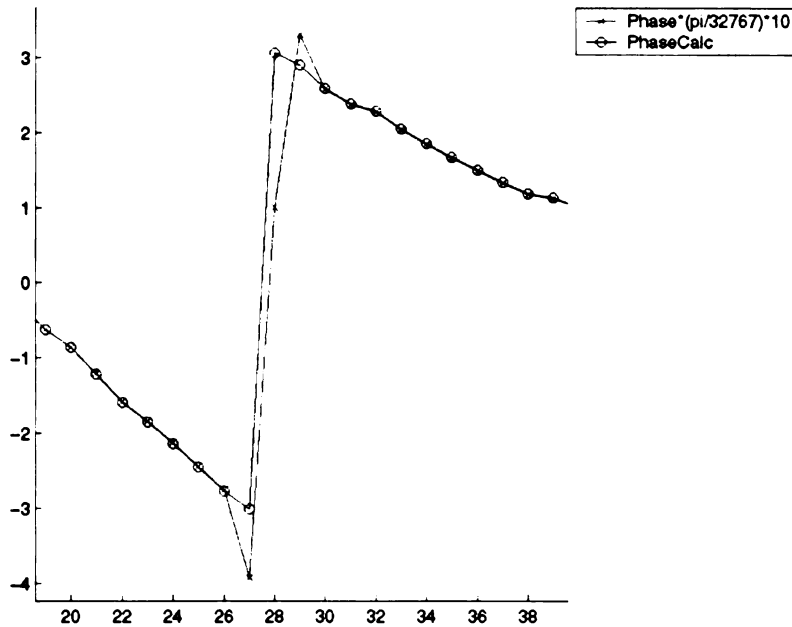
**Figure 2-20. Phase images and line profiles from GE scanner: Phase image (A) and phase from Real and Imaginary images (B).**



The “phase wrap transition zone” has characteristics of a blurring artifact, given that instead of a single step transition, there are three pixels that undershoot, land in the middle of the transition, and finally, overshoot the final value. Explaining these findings to GE engineers, it was discovered that this is an outcome of post-processing of the spatial domain images. An algorithm called “gradwarp” is implemented on GE scanners to compensate for the fact that the gradients are not perfectly linear in practice. The algorithm involves a convolution process which causes the “ringing” at the phase wrap transitions, which renders the images impossible to unwrap with “phase unwrapping” algorithms. The solution to the problem is to collect the real and imaginary images and derive the phase image from them, rather than using the phase image directly reconstructed by the scanner.

UCSF LIBRARY

**Figure 2-21. Detail of phase distortion effect from “grad\_warp” procedure.**



#### **2.4.9 MREView program**

A custom, Windows-based software program, “MREView”, was developed by Richard Ehman’s lab at the Mayo Clinic (Rochester, MN) for the purposes of analyzing dynamic MR elastography data. This program was provided to me for use with my experimental data. The primary purpose was to use the implementations of the direction filtering and wave image inversion, specifically using the local frequency estimation and direct inversion methods.

The typical inputs to the program include the magnitude and phase (or “wave image”) volumes, along with experimental parameters. The experimental parameters necessary to perform the inversion include FOV, MEG/excitation frequency, number of MEGs, and MEG amplitude. For all processing, the direction filters were applied in 2D in four evenly spaced directions, in other words up-down, down-up, right-left, and left-right.

---

### Technique comparisons

---

#### 3.1 Single-variable effects

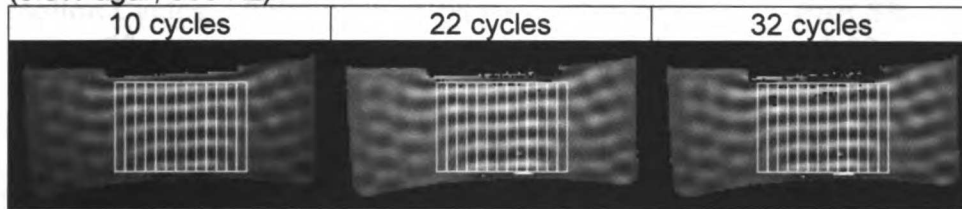
Experiments were done to evaluate the important factors for generating suitable wave images. Three experiments in particular formed the basis of appropriate methods for later application to quantify shear modulus in agarose and tissue samples. The important factors investigated were the number of motion cycles, MEG waveform shape, and motion/MEG operating frequency. First, the number of motion cycles imparted on the object was evaluated for both the effect on the phase to noise ration (PNR) and shear wave velocity estimate. Second, the shape of the motion encoding gradient (MEG) was evaluated, comparing trapezoidal and sinusoidal waveforms and their resulting PNR. Finally, the PNR and shear wave velocity estimates for the frequency range of 500 Hz to 1000 Hz was evaluated.

##### 3.1.1 Number of Applied Motion Cycles

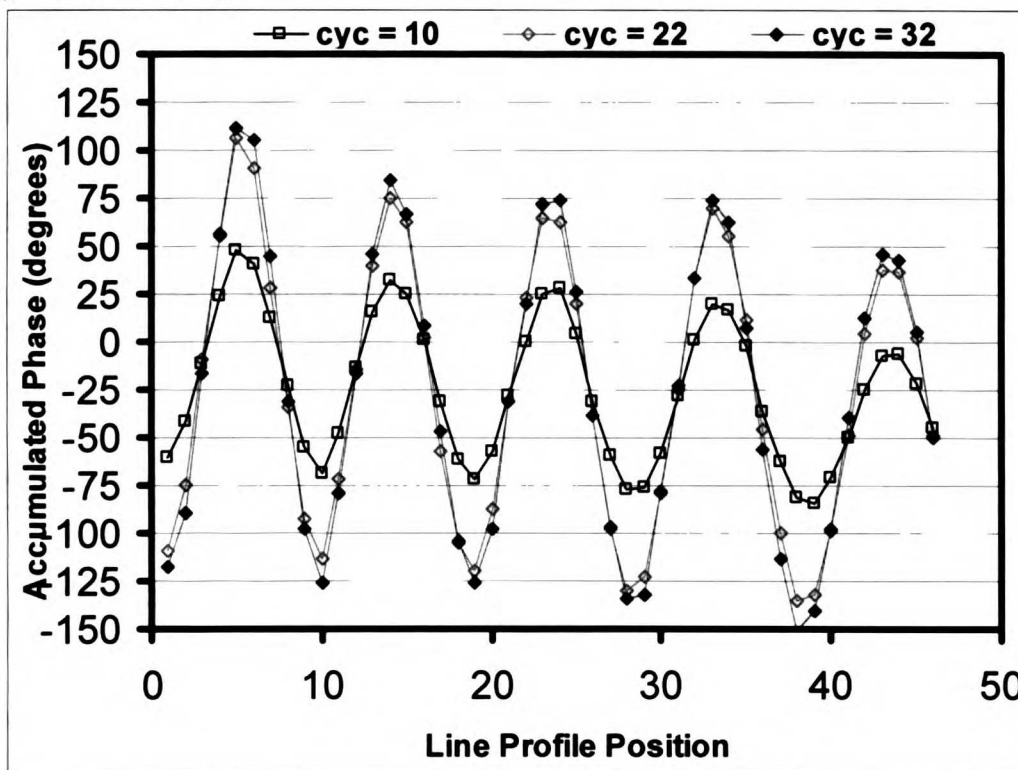
The effect of the number of motion cycles on the accumulated phase of the transmitted strain wave was evaluated by varying the number of cycles at 10, 22, and 32 cycles while the number of MEG's was fixed at 10. Example wave images and the ROIs used for the PNR and shear wave velocity analysis are shown in Figure 3-1. The entire ROI region was used for the PNR analysis (as described in section 2.4.3), while each 5-voxel-wide subregions was evaluated for shear wave velocity as described in section 2.4.4. A comparison of the median phase signal from one of the shear wave velocity ROI's is shown in Figure 3-2.

UCSF LIBRARY

**Figure 3-1. Comparison of wave images with varying number of motion cycles and ROIs for strain wave estimation (narrow strips) and PNR calculation (entire region).**  
 (0.5% agar, 500 Hz)



**Figure 3-2. Representative line profiles from ROI with varying number of motion cycles.**  
 (4<sup>th</sup> ROI from left)



The distributions of PNR values for the voxels in the ROIs were generated and summarized in Table 3-1. Analysis of variance determined that the condition of ten motion cycles had a significantly lower ( $p < 0.05$ ) mean PNR compared to the conditions with 22 and 32 motion cycles.

UCSF LIBRARY

**Table 3-1. Effect of number of motion cycles on mean PNR.**

| Motion Cycles | Statistically significant groups | PNR Mean | PNR SE |
|---------------|----------------------------------|----------|--------|
| 22            | A                                | 24.3     | 0.30   |
| 32            | A                                | 23.3     | 0.29   |
| 10            | B                                | 14.8     | 0.17   |

Levels not connected by same letter are significantly different

In the next stage of analysis, the shear wave velocity was determined in each of the 5-voxel-wide ROIs. The results from this analysis are shown in Table 3-2. Despite the significantly lower PNR for the 10 motion cycles condition, there was still adequate signal to determine the same shear wave velocity as the other conditions. No significant difference was found between the three conditions tested.

**Table 3-2. Effect of motion cycles on strain wavelength estimates.**

| Motion Cycles | Statistically significant groups | $\lambda$ Mean | $\lambda$ SE |
|---------------|----------------------------------|----------------|--------------|
| 10            | A                                | 4.56           | 0.059        |
| 22            | A                                | 4.55           | 0.045        |
| 32            | A                                | 4.53           | 0.046        |

Levels not connected by same letter are significantly different

### 3.1.2 Gradient Shape: Trapezoidal v. Sinusoidal

The encoding of phase in a time-varying magnetic field  $G_r(t)$  of a nuclear spin whose motion is described by  $r(t)$  over a time period  $\tau$  has been shown [21] to be:

$$\phi(\tau) = \gamma \int_0^{\tau} \vec{G}_r(t) \bullet \vec{r}(t) dt \quad [18]$$

where  $\gamma$  is the gyromagnetic ratio for the nucleus of interest (protons in all cases described here). A gradient waveform that switches in polarity at the same frequency as the spin motion can selectively encode the motion in the phase of the acquired signal. If that gradient waveform is square-shaped (though, in practice, it must be trapezoidal, but

UCSF LIBRARY

the ramp times are assumed to be negligible), then the “motion encoding gradient” (MEG) waveform is:

$$\vec{G}_r(t) = \begin{cases} +G; & t \in [nT, (2n+1)T/2) \\ -G; & t \in ((2n+1)T/2, (n+1)T] \end{cases} \quad [19]$$

where  $n = 0, 1, 2, \dots, N-1$ ,  $T = 2\pi/\omega$ ,  $\omega$  is the angular frequency of the harmonic mechanical spin motion, and  $G$  is the gradient amplitude in Gauss/cm. For sinusoidal spin motion, the position of each spin can be described by:

$$\vec{r}(t) = \vec{r}_0 + \vec{\xi}_0 \exp(j(\vec{k} \cdot \vec{r} - \omega t + \alpha)) \quad [20]$$

where  $\vec{r}_0$  is the mean position of the spin,  $\alpha$  is the phase offset between the mechanical motion and gradient waveforms,  $\vec{k}$  is the wave number, and  $\vec{\xi}_0$  is the peak displacement of the spin. Substituting into the equation above yields

$$\phi(\vec{r}, \alpha) = \gamma \int_0^{=NT < TE} \vec{G}_r(t) \cdot \vec{\xi}_0 \exp(j(\vec{k} \cdot \vec{r} - \omega t + \alpha)) dt \quad [21]$$

where  $TE$  is the echo time of the sequence,  $N$  is the number of gradient cycles. The solution for this case of having trapezoidal MEG's with negligible ramp times is therefore

$$\phi_{trapezoidal}(\vec{r}, \alpha) = \frac{2\gamma NT(\vec{G}_r \cdot \vec{\xi}_0)}{\pi} \sin(\vec{k} \cdot \vec{r} + \alpha) \quad [22]$$

As a second case, the MEG's may have a sinusoidal shape, where



$$\bar{G}_r(t) = \begin{cases} \bar{G}_0 \cos(\omega t); & t \in [0, NT) \\ 0 & \text{otherwise} \end{cases} \quad [23]$$

Substitution for the equation for the acquired phase gives

$$\phi_{\text{sinusoidal}}(\bar{r}, \alpha) = \frac{\gamma NT (\bar{G}_0 \bullet \bar{\xi}_0)}{2} \cos(\bar{k} \bullet \bar{r} + \alpha) \quad [24]$$

Assuming that the experimental conditions are controlled to match for the two methods, then the ratio of the acquired phase for sinusoidal to trapezoidal gradient waveforms can be simplified to:

$$\frac{\phi_{\text{trapezoidal}}}{\phi_{\text{sinusoidal}}} = \frac{2\gamma NT (G_r \bullet \xi_0)}{\frac{\pi}{\gamma NT (G_0 \bullet \xi_0)}} = \frac{4}{\pi} \quad [25]$$

and the relative increase in acquired phase will be:

$$\frac{\phi_{\text{trapezoidal}} - \phi_{\text{sinusoidal}}}{\phi_{\text{trapezoidal}}} = \frac{4/\pi - 1}{4/\pi} = 0.2146 \quad [26]$$

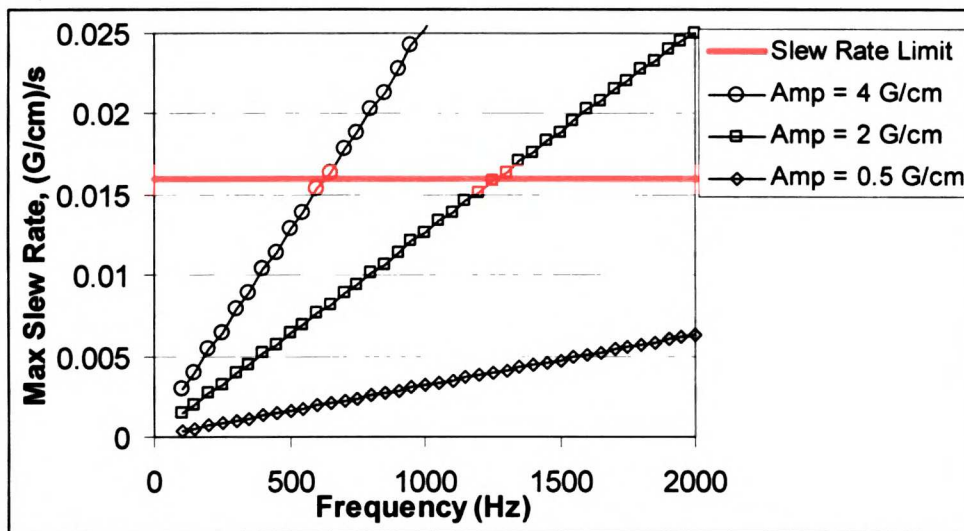
Therefore, theory suggests expecting sinusoidal gradients to be 21.5% less efficient at encoding phase due to cyclic motion compared to trapezoidal gradients.

The sinusoidal gradient waveform shape has some practical advantages from the standpoint of the gradient amplifier electronics. A sinusoidal waveform requires a continually changing slew rate, which tends to be less taxing on the amplifiers compared to a trapezoidal waveform. For a trapezoidal gradient, the maximum slew rate is required until the maximum amplitude is reached, whereas for the sinusoidal gradient the maximum slew rate would be required for a very short time, in the region of zero amplitude. However, depending on the frequency and maximum amplitude of the

UCSF LIBRARY

desired waveform, the sinusoidal shape will reach the maximum slew rate at lower frequency and amplitude compared to the trapezoidal waveform, which simply becomes more triangular in shape. The dependence of sinusoidal frequency and maximum gradient amplitude is shown in Figure 3-3. The sinusoidal waveform at full gradient strength (4 G/cm) will exceed the slew rate limit of 0.016 (G/cm)/s at a frequency of 650 Hz. Since the limit is inversely linearly related to the gradient amplitude, the slew rate limit is reached at 1300 Hz at a gradient amplitude of 2 G/cm.

**Figure 3-3. Sinusoidal waveform frequency and maximum slew rate at different gradient amplitudes.**



The effect of the MEG waveform shape was examined by comparing pulse sequences with trapezoidal and sinusoidal MEG's. For this experiment, a horizontally-aligned 0.5%/1.0% agar phantom was used. A contact plate located at the top of the phantom was attached to the piezoelectric bending element to produce shear motion. Six cycles of motion were applied at 100 Hz. Eight offsets of 0, 1.25, 2.5, 3.75, 5.0, 6.25, 7.5, and 8.75 ms of delay between the motion and MEGs were acquired. Two bipolar motion encoding gradients with amplitudes of 0.5 G/cm and frequency of 100 Hz were played on the z-axis. Spin echo-based sequences were used, with TE/TR = 20/300 ms, bandwidth = 15.6 kHz, FOV = 12 cm, slice thickness = 5 mm, matrix size =

UCSF LIBRARY

256 x 160 (frequency x phase), NEX = 1 and Axial imaging plane. The frequency direction for the sinusoidal MEG experiment was R/L, however it was A/P for the trapezoidal MEG experiment. This difference was unintended, but is expected to have negligible effect.

In order to implement the experiment, two pulse sequences were needed. First, the trapezoidal sequence was achieved with a sequence that used the "TRAPEZOID" command in EPIC to create the desired pulse waveforms. However, to achieve sinusoidal-shaped MEG's, the pulse sequence was modified to read in external waveform files. This sequence uses the "EXTWAVE" command to access the waveform file that is played by the scanner when the MEG is required. Digital oscilloscope screenshots of the two pulse sequences are shown in Figure 3-4 and Figure 3-5.

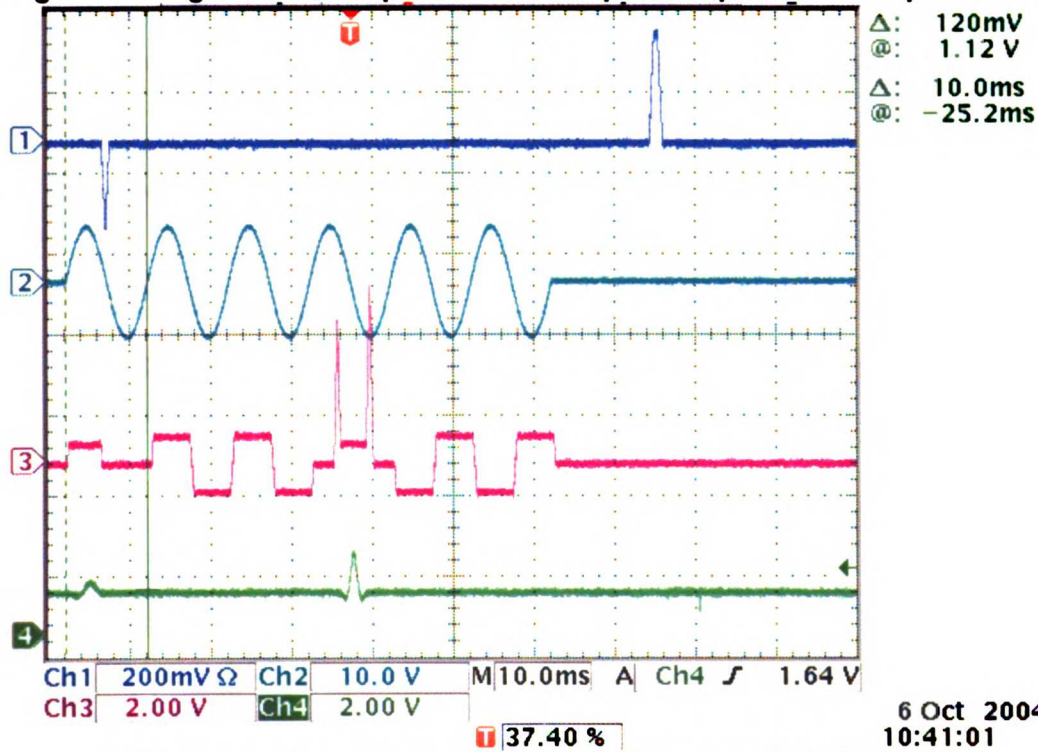
Representative magnitude and phase images are shown in Figure 3-6 for the trapezoidal and sinusoidal motion encoding gradient methods. The phantom is oriented with the 1.0% agar region on the left, and at the applied frequency of 100 Hz, the strain wavelengths are approximately the length of the phantom material. Therefore, very slight, if any, strain wave peak and trough are visible in this part of the phantom. However, on the right side, in the 0.5% agar, approximately four periods of strain waves can be visualized, decreasing in amplitude as the wave moves away from the contact plate. The strain wave images contain background phase that varies between sequences. To remove the background phase variation, the difference of wave images offset in time by one-half period (5.0 ms) was found, resulting in four wave difference images. These four images for each sequence were used in all subsequent analyses.

The two methods are evaluated by a phase-to-noise (PNR) calculation (see section 2.4.3) in a region of interest (ROI) and by strain wavelength estimates (see section 2.4.4). Figure 3-7 shows the ROIs used to estimate signal-to-noise (SNR) and PNR. To calculate PNR, an absolute maximum intensity projection was performed

UCST LIBRARY

across the four wave difference images. This was divided by the arctangent of the inverse of the magnitude signal to noise ratio, which was found by dividing the magnitude images by the standard deviation of the signal in a region of air (Figure 3-7A) and averaging across the four offsets. The PNR in the ROI (Figure 3-7B) was compared between the two methods with a t-test.

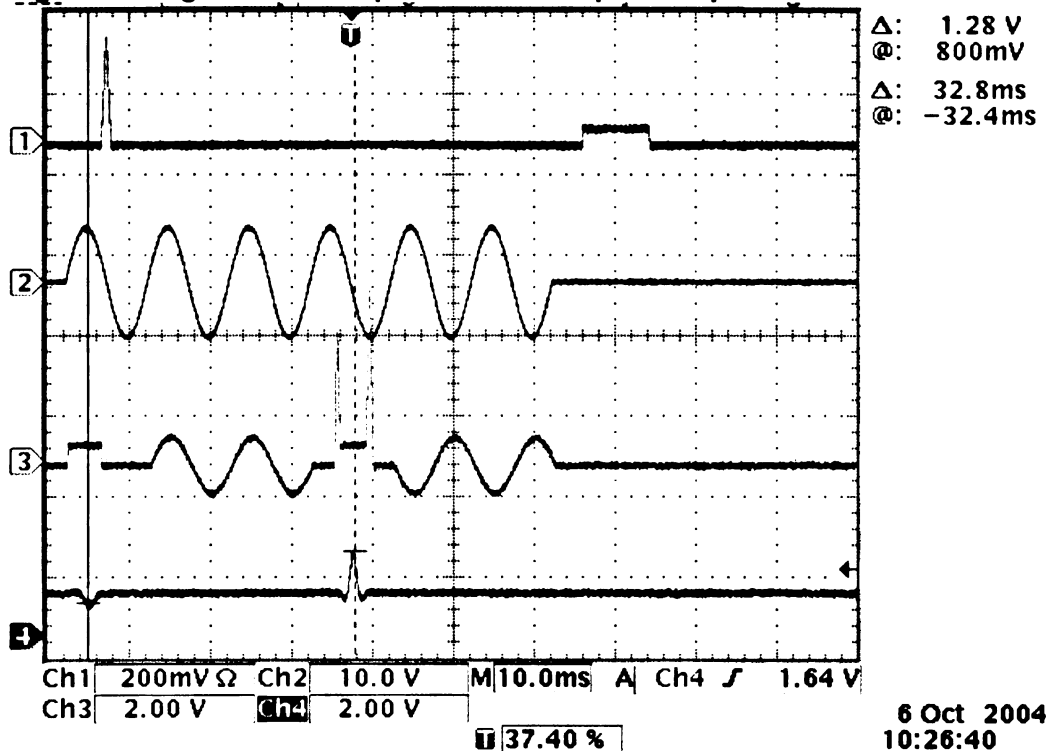
Figure 3-4. Digital oscilloscope screenshot of pulse sequence with trapezoidal MEG's.



\* Ch 1 = y gradient, Ch 2 = motion signal, Ch 3 = z gradient, Ch 4 = RF.

UGST LIBRARY

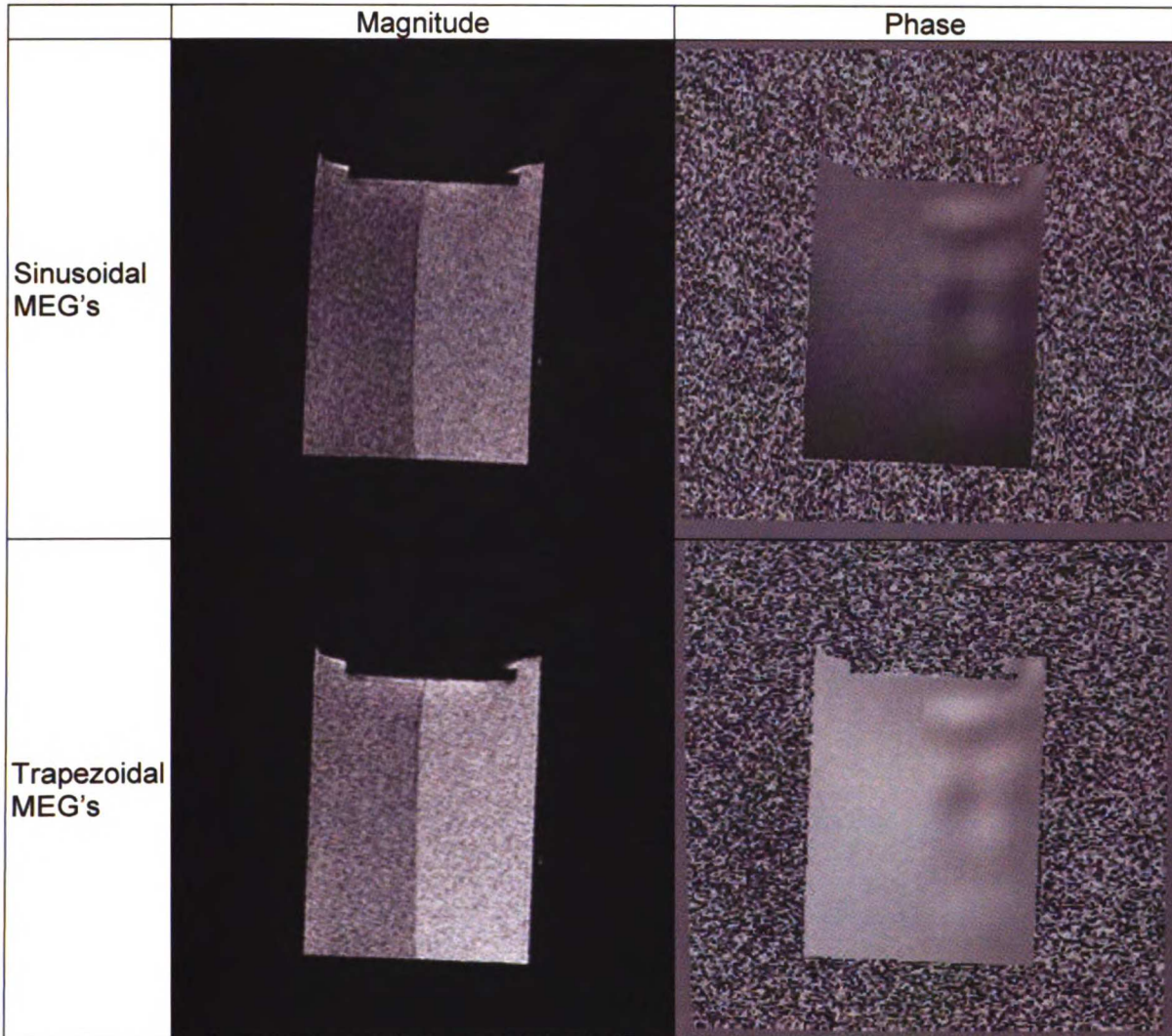
Figure 3-5. Digital oscilloscope screenshot of pulse sequence with sinusoidal MEG's.



\* Ch 1 = x gradient, Ch 2 = motion signal, Ch 3 = z gradient, Ch 4 = RF.

UGST LIBRARY

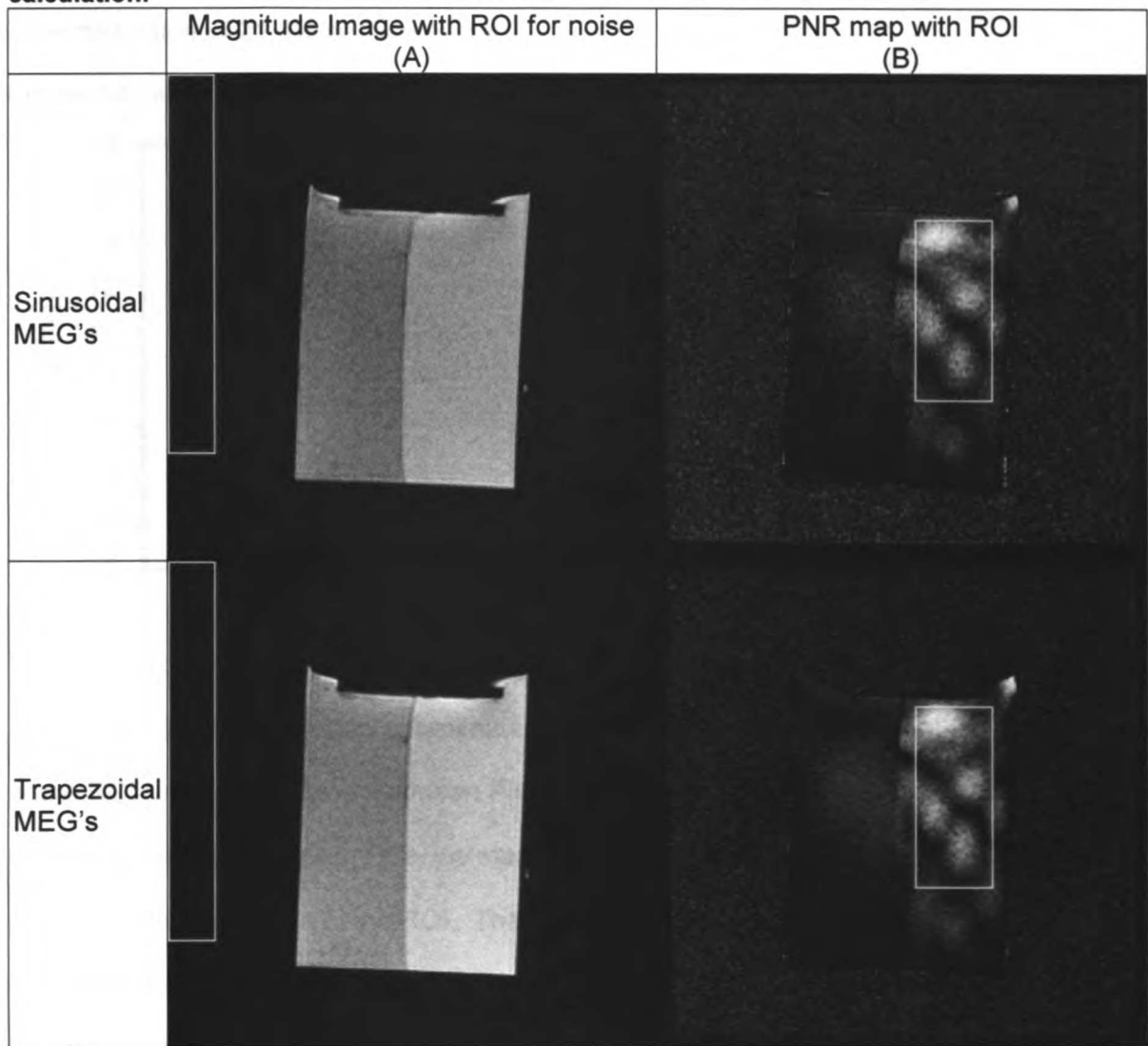
**Figure 3-6. Representative Magnitude and Phase images for Trapezoidal and Sinusoidal MEG's.**



\* Axial view of 0.5% (right) and 1.0% (left) Agar phantom.

WEST LIBRARY

**Figure 3-7. Phase-to-noise (PNR) ratio maps with region of interest for mean PNR calculation.**

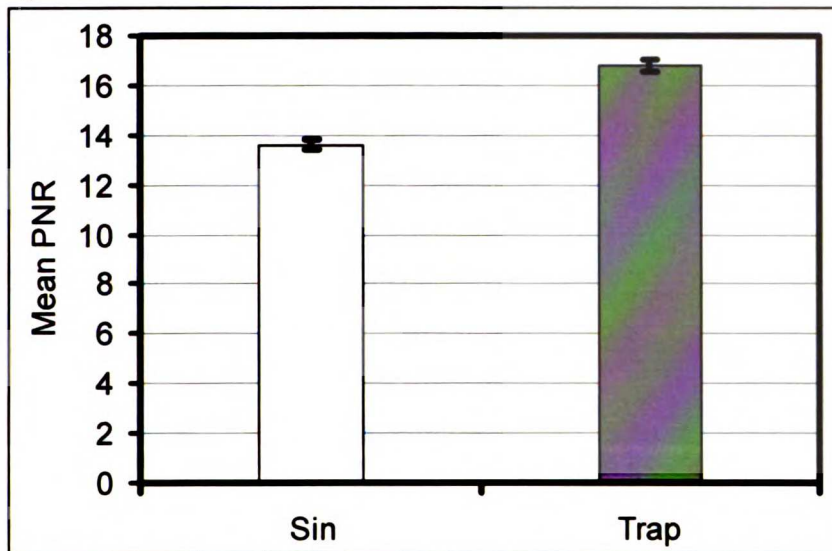


The mean PNR for the two methods is shown in Figure 3-8 with the error bars representing the 95% confidence interval of the estimate of the mean. The trapezoidal gradients achieved a mean PNR of 16.8, compared to 13.6 for the sinusoidal MEG's. The results of the t-test found that the mean difference in PNR of 3.2 was highly significant ( $p < 0.001$ ). Therefore, the trapezoidal waveforms are found to achieve more efficient encoding of motion into the phase of the acquired signal compared to the sinusoidal waveforms. The relative empirical PNR difference –  $(16.8 - 13.6)/16.8$  – of

UCSF LIBRARY

19.1% (95% confidence interval: 17.1% to 21.0%) compares almost exactly with the expected value of 21.5% derived earlier.

**Figure 3-8. Mean PNR for Sinusoidal and Trapezoidal MEGs.**



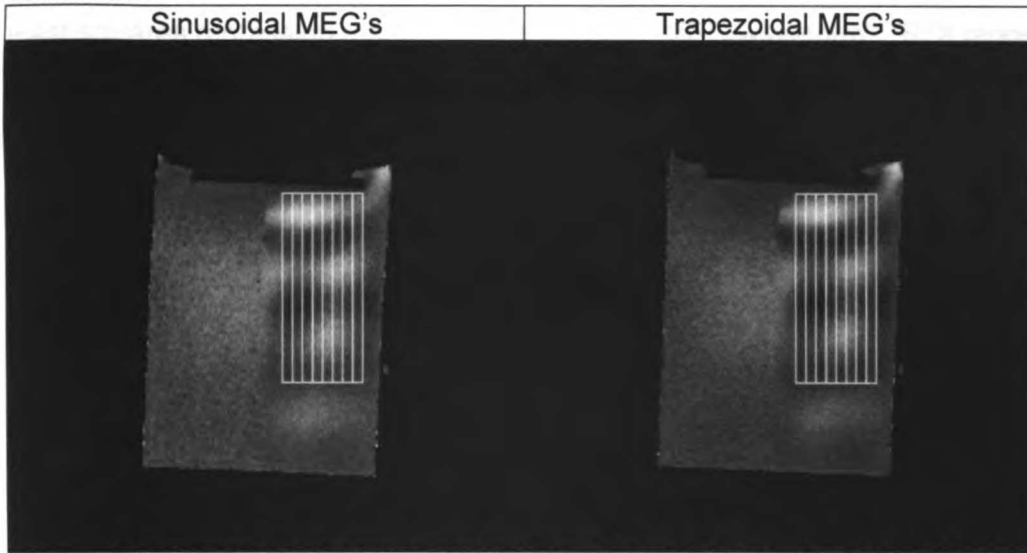
\* Error bars are 95% confidence interval for mean PNR value

To compare the ability to estimate strain wavelength for the two methods, the same ROI used to calculate the mean PNR was divided into vertical columns five voxels wide (Figure 3-9). For each ROI, the median phase signal was found along the length across the five elements of the ROI. The median phase signal along the length of the ROI (and direction of propagation of the shear wave) was zero-filled by a factor of 20, and the frequency power spectrum was calculated by the Fourier transform. The maximum of the power spectrum in the spatial frequency range corresponding to wavelengths of 0 to 2 cm was chosen as the characteristic shear wavelength ( $\lambda$ ) for the ROI (Figure 3-10).

ULST LIBRARY

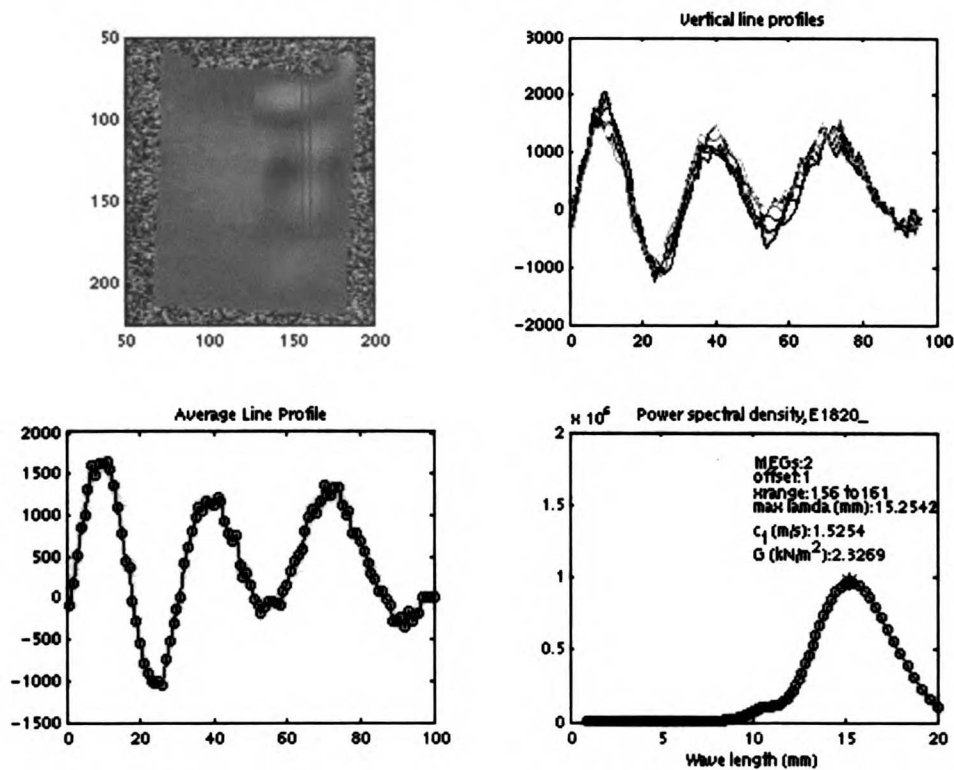


Figure 3-9. Representative wave difference images with ROI's used for shear wavelength estimation.



\* ROI's are labeled left-to-right by x-axis boundaries, the leftmost is "134 to 139".

Figure 3-10. Strain wavelength estimation procedure.



The shear wavelength,  $\lambda$ , was estimated in each of eight ROIs for the four wave difference images (at different delay offsets) for the two methods (sinusoidal and

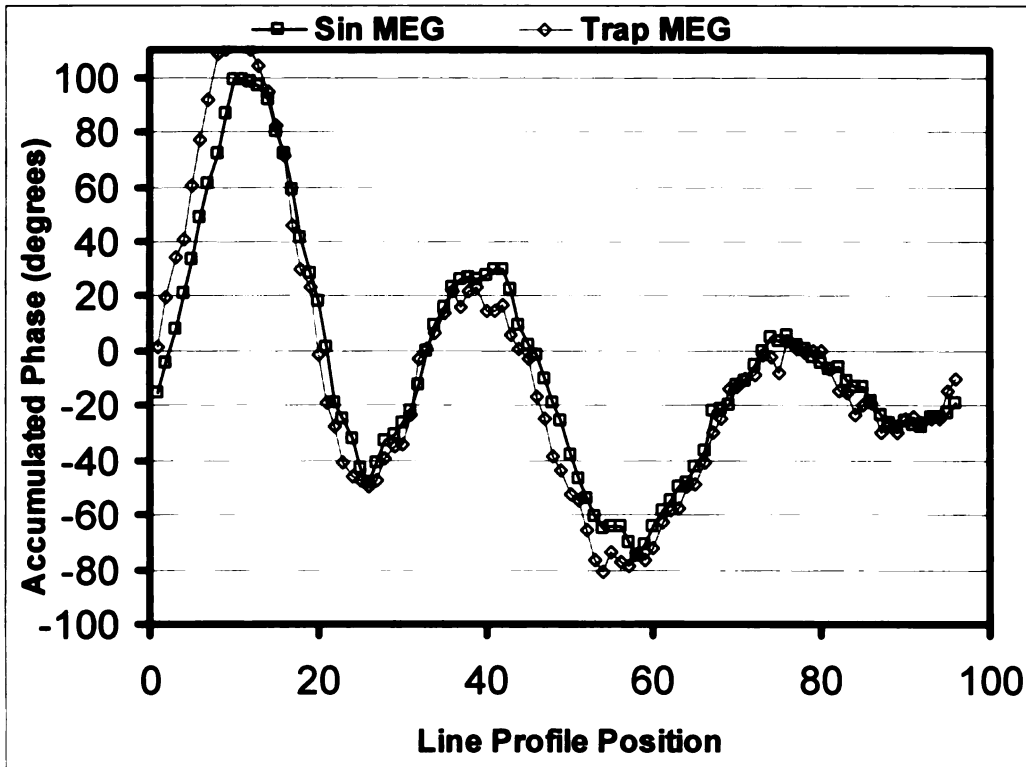
UNIVERSITY LIBRARY

trapezoidal MEG waveforms). These 64 measurements of  $\lambda$  were analyzed by a linear least squares regression model with the terms of "MEG waveform", "ROI range", and the first-order cross-term. Posttests using the Student's t-test were performed on significant effects.

Comparing the line profiles of the sinusoidal and trapezoidal MEG methods shows slightly greater amplitude of the accumulated phase due to the strain wave for the trapezoidal MEGs (Figure 3-11). The results of the linear regression model, however, did not find a significant difference in strain wavelength estimates for the sinusoidal and trapezoidal MEGs. The only significant effect for the model was the "ROI Range", and the posttest results in Table 3-3 revealed a decreasing strain wavelength (and therefore decreased shear stiffness) as the ROI region moved away from the side of the phantom. The strain wavelengths decreased from 15.7 mm near the side of phantom to approximately 14.7 mm near the center of the phantom. A possible explanation for the increase in shear stiffness towards the sides of the phantom may simply reflect the influence of the agar being in contact with the extremely stiff plastic container, thus making the boundary regions stiffer, or creating an artificial shear stiffness gradient across this homogeneous region of the phantom. Further experiments are required, but it is speculated that this effect is frequency dependent, and will decrease as the excitation frequency is increased. At higher frequencies, and therefore lower wavelengths, the "sphere of influence" that affects the local displacements could be decreased.

U.S. LIBRARY

**Figure 3-11. Representative Comparison of Line Profiles for SIN and TRAP MEG methods.**



\* Median value for ROI 2 (second from left), delay = 0 ms

**Table 3-3. Posttest results for the effect of ROI on mean strain wavelength ( $\lambda$ ) estimate.**

| Position relative to side of phantom | ROI Range  | Statistically significant groups | Mean $\lambda$ |
|--------------------------------------|------------|----------------------------------|----------------|
| 1                                    | 169 to 174 | A                                | 15.71          |
| 2                                    | 164 to 169 | A B                              | 15.48          |
| 3                                    | 159 to 164 | B C                              | 15.27          |
| 4                                    | 154 to 159 | C D                              | 15.06          |
| 5                                    | 149 to 154 | D E                              | 14.89          |
| 8                                    | 134 to 139 | E                                | 14.80          |
| 6                                    | 144 to 149 | E                                | 14.80          |
| 7                                    | 139 to 144 | E                                | 14.67          |

\* ROIs not connected by same letter are significantly different,  $p < 0.05$ .

### 3.1.3 High Frequency experiments (>500 Hz)

In order to investigate the effectiveness of increasing the frequency – and therefore extending the potential upper shear stiffness measurement range – the effect of increasing the excitation frequency up to 1 kHz was examined with the SE method. These experiments were performed with the with excitation frequencies of 625, 672,

UNIVERSITY LIBRARY

731, 800, 865, and 1000 Hz. These frequencies were chosen to span the range of 500 to 1000 Hz, and to minimize digitization timing errors due to the 4 microsecond time interval of the scanner. For these “high frequency” experiments, M =10 MEG’s were used, with motion cycles of N = 30, 31, 32, 32, 34, and 35 for the respective frequencies. The TE’s were  $0.02 + 20*(1/f)$  sec, where f is the frequency of excitation and the TR = 175 ms. The NEX was set to 4, and eight offsets between the phase of the mechanical motion and MEG’s were acquired. Each offset had a scan time of 1m 50s.

For the high frequency experiments, two vertically-oriented ROI’s were analyzed in the 1.0% agar region. A one-way ANOVA and Student’s t-tests for posttests was used to examine the effect of motion frequency on PNR. All image processing was performed with Matlab (Mathworks, Natick, MA) and all statistical analyses were performed with JMP (SAS Institute, Cary, NC).

At frequencies above 500 Hz with the SE method, strain waves became less prominent as the frequency increased (Figure 3-12). The one-way ANOVA of PNR for SE experiments at frequencies of 500 to 1000 Hz fit the data with a high level of significance ( $p < 0.0001$ ). The PNR was found to be significantly different ( $p < 0.05$ ) for all frequencies tested except that 731 and 800 Hz were found to be statistically equivalent (Figure 3-14). It is notable that the reduced shear motion amplitude at higher frequency relates directly to reduce PNR. It is unclear, however, why the 865 Hz condition results in lower PNR than the 1000 Hz condition.

Figure 3-12. Example wave images at high frequency.

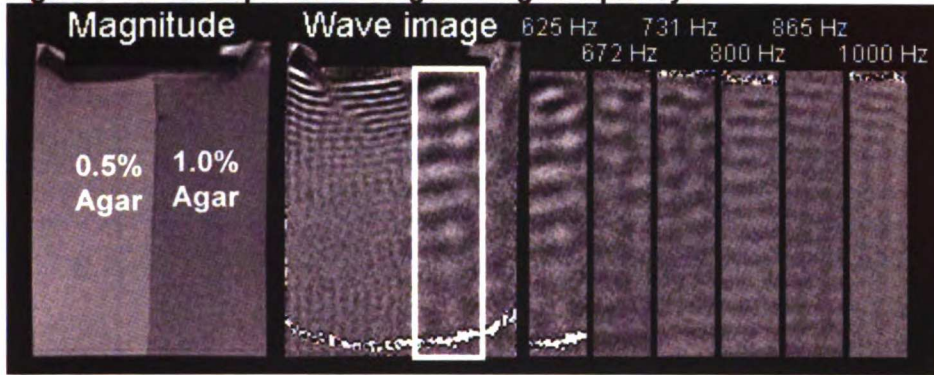
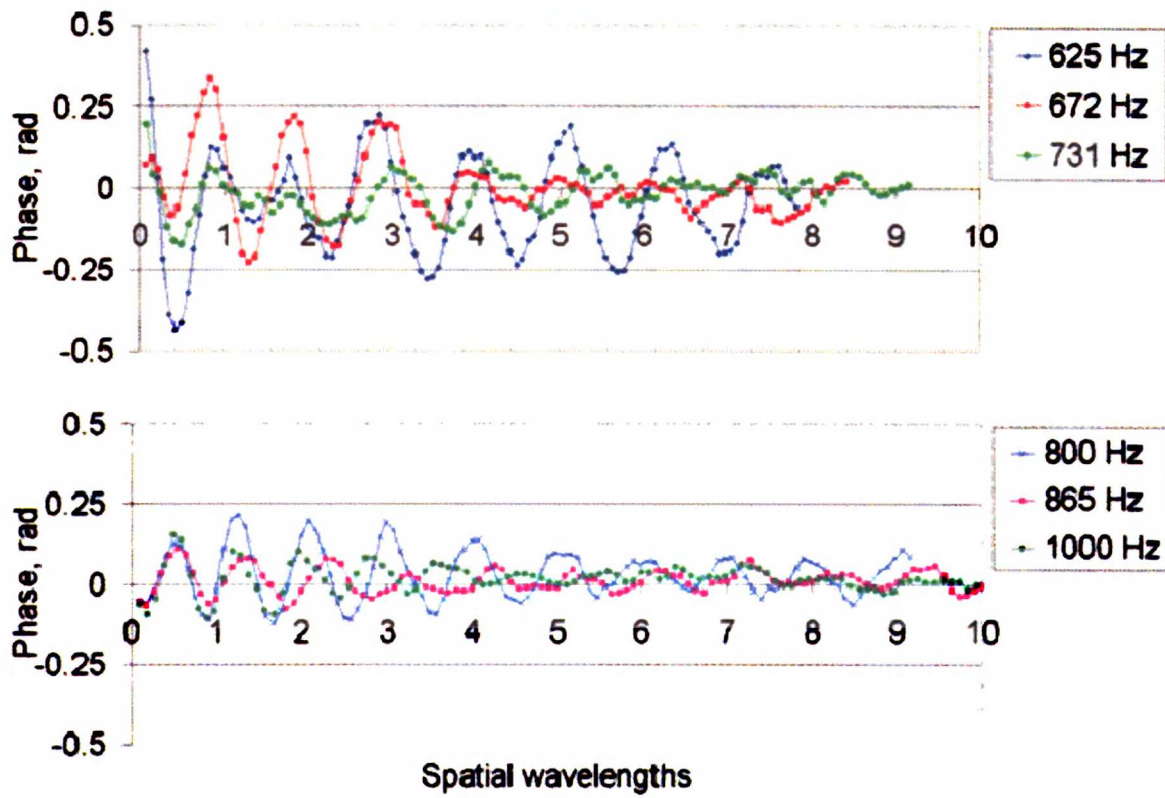


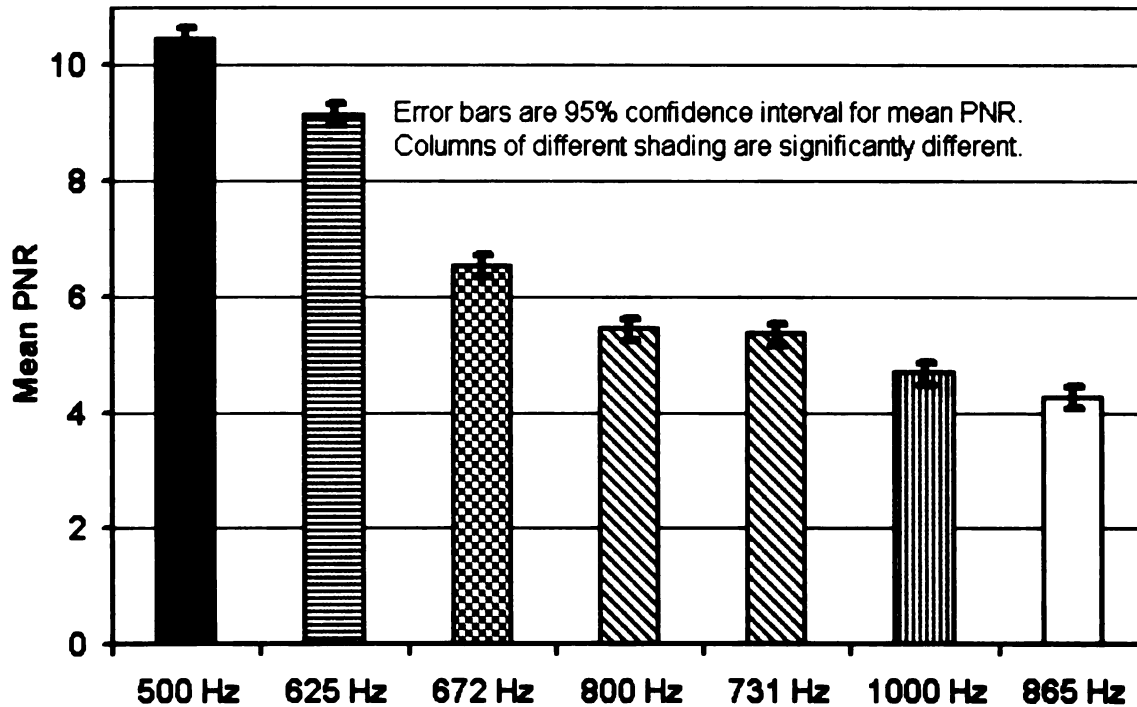
Figure 3-13. Phase amplitude for strain wave at high frequencies.



ULST LIBRARY

**Figure 3-14. ANOVA results comparing mean Phase-to-Noise Ratio for the different frequencies tested with the SE method.**

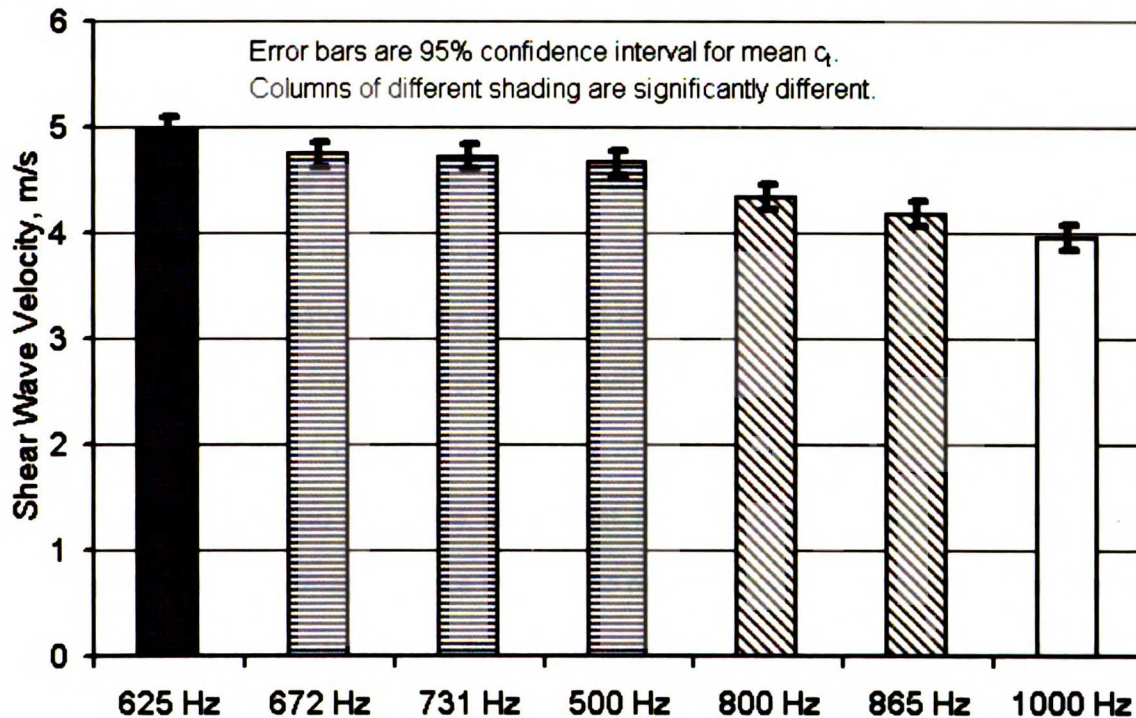
Note NEX = 1 at 500 Hz, NEX = 4 for all others.



The PNR regions of interest were also analyzed with the method described in section 2.4.4 for shear wave velocity. Therefore, the effect of increasing motion and MEG frequency on the ability to resolve the underlying shear wave velocity (and therefore shear modulus) can be assessed. The one-way ANOVA of shear wave velocity for SE experiments at frequencies of 500 to 1000 Hz fit the data with a high level of significance ( $p < 0.0001$ ). At 800 Hz and above, the shear wave velocity was found to be significantly ( $p < 0.05$ ) lower than that determined at 500 Hz as shown in Figure 3-15. The results show that the reduced shear motion amplitude at frequencies above 731 Hz negatively affects the ability to estimate the shear wave velocity.

ULST LIBRARY

**Figure 3-15. Comparison of shear wave velocity for different frequencies in 1.0% Agar with the SE method.**



### 3.2 SE v. GRE with varying MEGs

An experiment was designed to assess the detectability of shear waves using alternate pulse sequences (spin echo or gradient echo) with a varying number of motion encoding gradients (MEGs). By determining the optimal method for elastography, the method can then be applied to a more difficult situation of assessing the shear modulus of ex vivo intervertebral disc tissue under different states of hydration and degeneration.

#### 3.2.1 SE v. GRE background

The spin echo MRI technique was the first successful imaging technique. Its advantage lies in its robustness in the face of field inhomogeneities. Field inhomogeneities have the effect of dephasing the signal in each imaging voxel, which derives from the summation of the spin magnetization vectors located in the voxel. Each

spin will have a slightly different rate of precession, thus causing the dephasing to increase with time. In other words a “dephasing envelope” continues to grow as faster precessing spins advance relative to slower precessing spins. The simple yet effective method of the spin echo allows the dephasing to proceed, and then cause a “refocusing” by a second RF pulse, a  $180^\circ$  pulse. This will rotate all spin magnetization vectors such that the spins which had the fastest precession rate are placed at the “end”, and those with the slowest precession rate are now found at the “beginning” of the dephasing envelope. All the spin magnetization vectors will become coherent at the echo, thus producing a strong signal despite the presence of field inhomogeneities.

The gradient echo technique, in contrast, requires a very homogeneous field to successfully create an image. Since there is no refocusing pulse, and that the gradients used for imaging are by definition a field inhomogeneity, the acquired signal will have signal with phase values that vary across the imaging object.

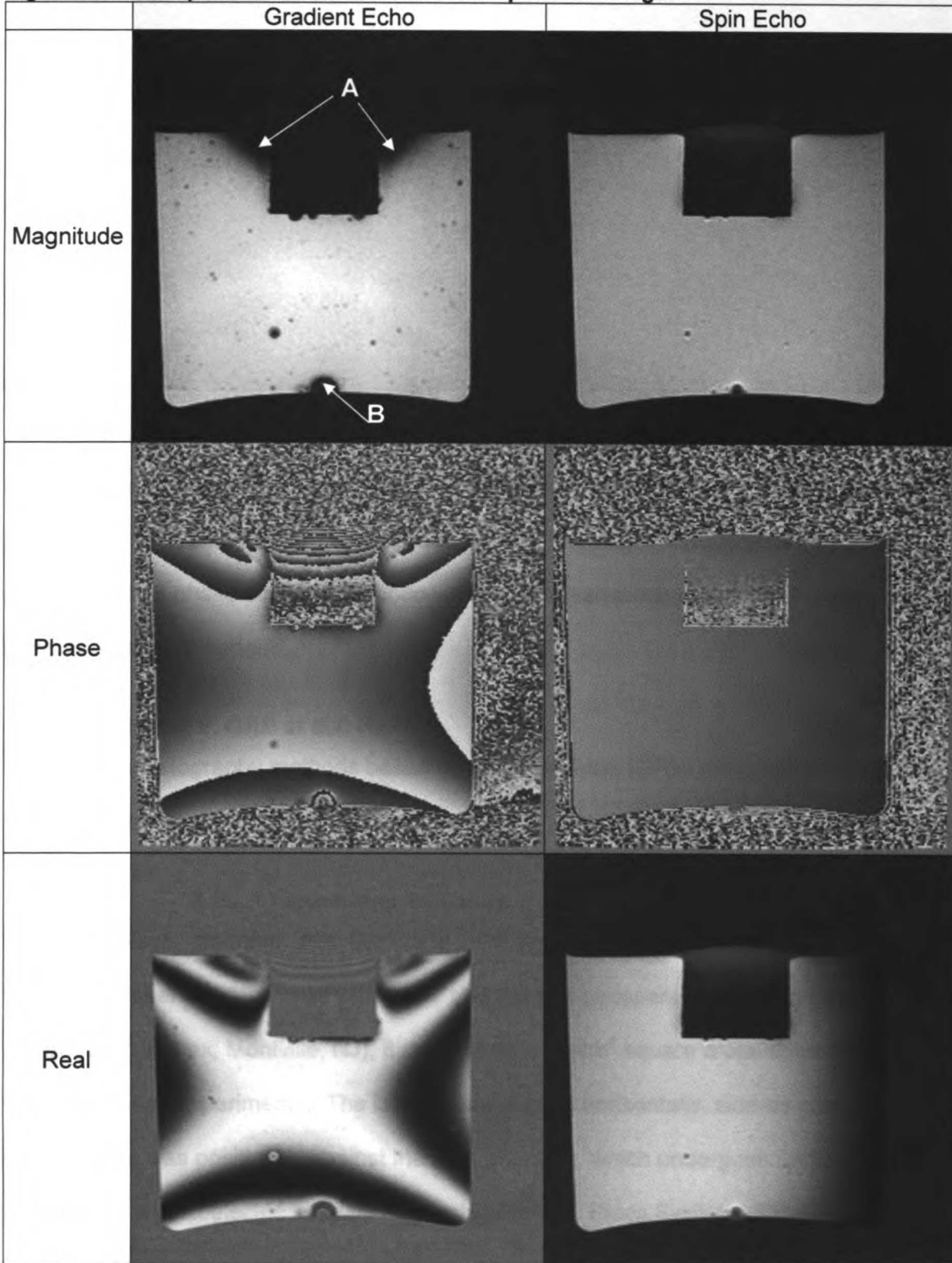
The contrast of the two imaging techniques is shown in Figure 3-16, which has all four possible views of the acquired signal (the magnitude, phase, real and imaginary images) of a gel phantom with a piezoelectric bending element attached to a plastic piece that is inserted into the phantom. The magnitude image shows some characteristic differences between gradient echo and spin echo images. The gradient echo’s vulnerability to field inhomogeneities is clearly visible around the piezoelectric bending element (arrow A) and air bubbles (arrow B). The air bubbles appear much larger on the gradient echo image due to inhomogeneities from susceptibility differences between the gel and air. In addition there is a visible shading across the gradient echo compared to the spin echo image.

In the phase image, the spin echo displays the effect of the refocusing that creates a homogeneous phase background. In contrast, the gradient echo image has a strongly varying phase across the image leading to phase wrap. The source of this

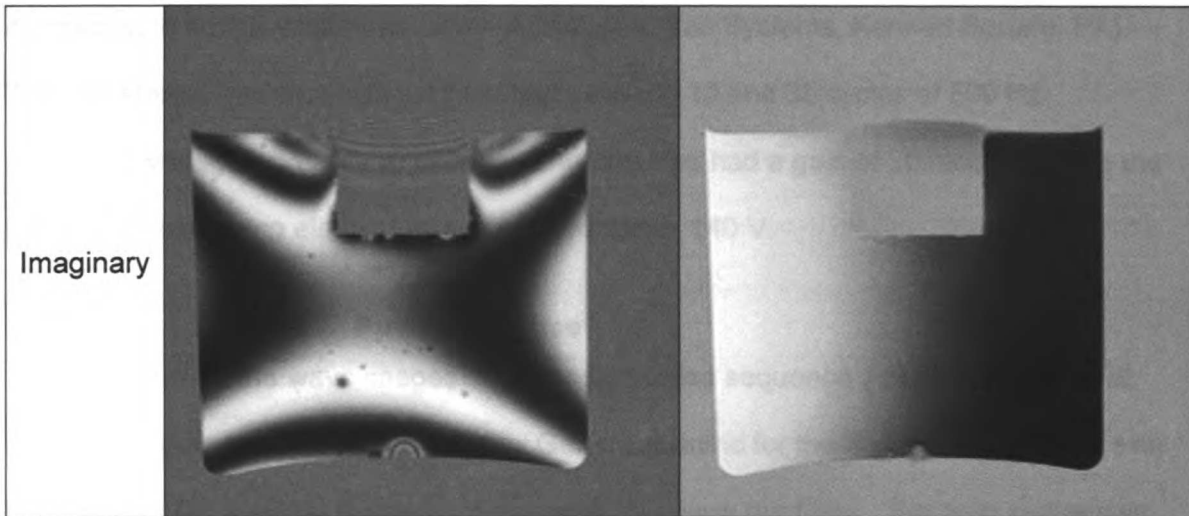


variation is seen in the real and imaginary images, which themselves have a strong variation across the object. The real and imaginary images for the spin echo technique, on the other hand, are slowly varying.

Figure 3-16. Comparison of Gradient Echo and Spin Echo images



WOLF LIDKANYI



For the purposes of MRE in 2D, it is clear that the spin echo method will have significant advantages over a gradient echo technique. Most obvious are the resistance to distortion from susceptibility effects causing field inhomogeneities and having a stable, nearly constant phase background upon which phase variations due to strain wave transmission will be added.

### 3.2.2 SE v. GRE at 500 Hz

MR elastography methods based on Gradient Echo (GRE) and Spin Echo (SE) techniques using an excitation frequency of 500 Hz were compared.

#### 3.2.2.1 Experimental set-up

A bi-layer phantom, with 0.5% and 1.0% agar (Sigma-Aldrich, St. Louis, MO, Product Number A9539) mixed with water and 0.5 mM gadopentetate dimeglumine (Magnevist®, Berlex, Montville, NJ), 8 cm tall with a 16 cm<sup>2</sup> square cross-sectional area, was used for all experiments. The layers were aligned horizontally, side-by-side. A contact plate was positioned against the agar phantom, which undergoes cyclic motion powered by a piezoelectric bending element (EPA-104, Piezo Systems, Cambridge, MA), similar to a previous technique [106]. The cyclic motion is controlled by a programmable, digital waveform generator (Model 33250A, Agilent, Palo Alto, CA)

connected to a high-voltage amplifier (A-303, A.A. Lab Systems, Kennett Square, PA). The waveform generator was set to output between 10 and 38 cycles of 500 Hz sinusoidal voltage with a 7V amplitude. The amplifier had a gain of 20, and therefore the piezoelectric bending element was energized with  $\pm 140$  V.

### **3.2.2.2 Pulse Sequence**

To create the wave images, the standard pulse sequence software for the GRE and SE imaging techniques provided by General Electric for the Signa EXCITE 3.0 Tesla MR system (GE Medical Systems, Waukesha, WI) were modified. For both sequences, several modifications were needed. First, an output trigger signal was added to be sent to the waveform generator. This was done using one of the data acquisition board output channels available on the Combined Exciter Receiver Data acquisition board of the scanner. The trigger signal was programmed to start at the same location at the beginning of each TR of the scan. Additional adjustments to the timing of the motion signal (delay time and initial phase) were controlled by the programmable waveform generator.

Bipolar, balanced trapezoidal motion encoding gradients (MEG's) were added to the sequences. These were added so that user-modifiable "control variables" could be changed at the time of the scan to adjust the number, amplitude, and axis (frequency, phase, or slice selection) of the motion encoding gradients. For the experiments comparing the SE and GRE methods, the frequency was 500 Hz, the amplitude was 3.5 Gauss/cm with ramp times of 250  $\mu$ s, and the axis was the slice selection direction. The number of gradients (M) was set to be 5, 10 and 15.

For the SE technique, M bipolar gradients were added before the refocusing pulse to have positive-then-negative lobes, while after the refocusing pulse the M gradients had negative-then-positive lobes (Figure 3-18). The timing of the waveform

generator trigger was set so that five motion cycles would be completed once the MEG's started. The software ensures that the start of the negative-then-positive lobes is exactly a whole integer number of wavelengths from the start of the positive-then-negative lobes. This is done by adding "wait time" around the refocusing pulse when no gradients are played. At 500 Hz, the total time of the "wait time" and the refocusing pulse was 6 ms, or 3 wavelengths. A single set of magnitude and phase images is created for each scan with the SE technique. A single scan with no motion was acquired and subtracted from all offsets for the SE technique to correct for background phase variations.

For the GRE technique, the bipolar gradients were added immediately after the RF pulse. The timing of the waveform generator trigger was set so that five motion cycles would be completed once the MEG's started (Figure 3-19A). On alternate TR's, the polarity of the MEG's was reversed (Figure 3-19B). The scanner was programmed to reconstruct the acquired data from the alternate TR's as two separate images, resulting in two magnitude and phase image pairs for each scan. One pair has motion encoded with positive-then-negative MEG's, while the second pair is encoded with negative-then-positive MEG's. The final wave image is the difference of these phase images. Note that these experiments were performed before the real and imaginary images were acquired to calculate the phase images that are not blurred by the GE software (see section 2.4.8).

### **3.2.3 MR Imaging**


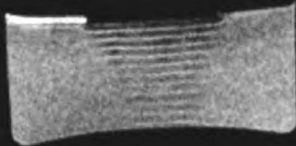
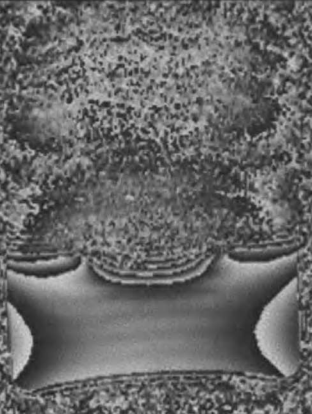
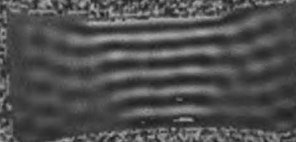
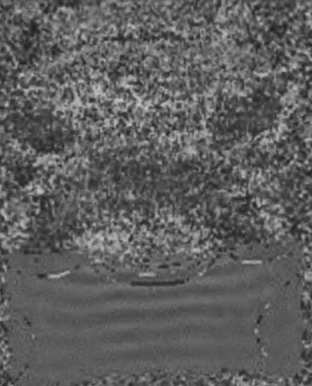
Scanning was performed on a General Electric Signa EXCITE 3.0 Tesla MR system with a maximum gradient amplitude and slew rates of 40 mT/m and 150 mT/m/ms. The agar phantom and piezoelectric actuator were placed inside a standard head coil, with the bending action of the actuator along the direction of the main field. Coaxial cable connected the actuator to a filtered pass-through connection in the wall of

the scanner room. On the other side of the wall, the amplifier and waveform generator were connected by coaxial cable.

For both the GRE and SE methods at 500 Hz, the TR was 175 ms. The TE's were 20, 30, and 40 ms for the GRE method for  $M = 5, 10, \text{ and } 15$ , respectively. For the SE technique, the TE's were 40, 60, and 80 ms for  $M = 5, 10, \text{ and } 15$ , respectively. The number of motion cycles,  $N$ , was set equal to  $M+5$  for the GRE and  $2M+8$  for the SE techniques. To achieve multiple samples of the motion in the object, eight offsets between the phase of the motion and motion encoding gradients were used. The offsets of the sinusoidal motion signal were at relative times of 0, 250, 500, 750 microseconds, with initial phase of  $0^\circ$  and  $180^\circ$ . This method limits the difference in time that the shear waves propagate into the phantom to less than one-half wavelength. Each offset had a scan time of 30 s for the SE method, and 60 s for the GRE method. For both techniques, the bandwidth was 15.6 kHz, FOV = 12 cm, 5 mm slice thickness, 256 x 160 matrix, NEX = 1, and the acquisition plane was axial. The flip angle for the GRE method was  $30^\circ$ . Representative magnitude, phase, and phase difference images are shown in Figure 3-17.

UWOT LIBRARY

**Figure 3-17. Representative elastography images with gradient and spin echo methods.**

|                  | Gradient Echo   | Spin Echo   |
|------------------|---|---|
| Magnitude        |    |   |
| Phase            |   |  |
| Phase Difference |  | n/a   |

UJOT LIDIANI

### 3.2.3.1 Image analysis

To compare the pulse sequence techniques, two sets of analyses were done. The phase difference wave images were analyzed to estimate the shear wavelength (section 2.4.4) and to determine phase-to-noise ratio efficiency (section 2.4.3). Shear wavelength was determined in vertically-oriented – away from the contact plate – regions of interest (ROI's) with dimensions of 5 by 100 voxels. Five adjacent ROI's were analyzed in both the 1.0% and 0.5% agar regions of the phantom across all eight offsets and both methods, SE and GRE, at 500 Hz (Figure 3-20A-B). For each ROI, the median phase value across the 5-voxel width for each of the 100 length positions was determined. The median phase signal was zero-filled up to a length of 2000, and the frequency power spectrum was calculated by the Fourier transform. The maximum of the power spectrum in the spatial frequency range corresponding to wavelengths of 0 to 2 cm was chosen as the characteristic shear wavelength ( $\lambda$ ) for the ROI. The shear wavelength was converted to shear wave velocity ( $c_i$ ) and shear modulus ( $G$ ) by

$$c_i = f * \lambda \quad [27]$$

$$G = \rho * c_i^2 \quad [28]$$

where  $f$  is the excitation frequency (500 Hz) and  $\rho$  is density of the object, assumed to be that of water.

Least squares linear regression models were used to evaluate differences in shear wavelength and shear wave velocity estimates for the different elastography techniques and ROI's. Specifically, for the experiments at 500 Hz the 0.5% and 1.0% agar regions were analyzed separately. The effects of pulse sequence (either the GRE or SE-based sequence), number of MEGs, ROI location, all first-order cross-terms and the second-order cross term on shear wavelength estimates were evaluated. For the experiments at different frequencies, the effects of ROI location, motion frequency and

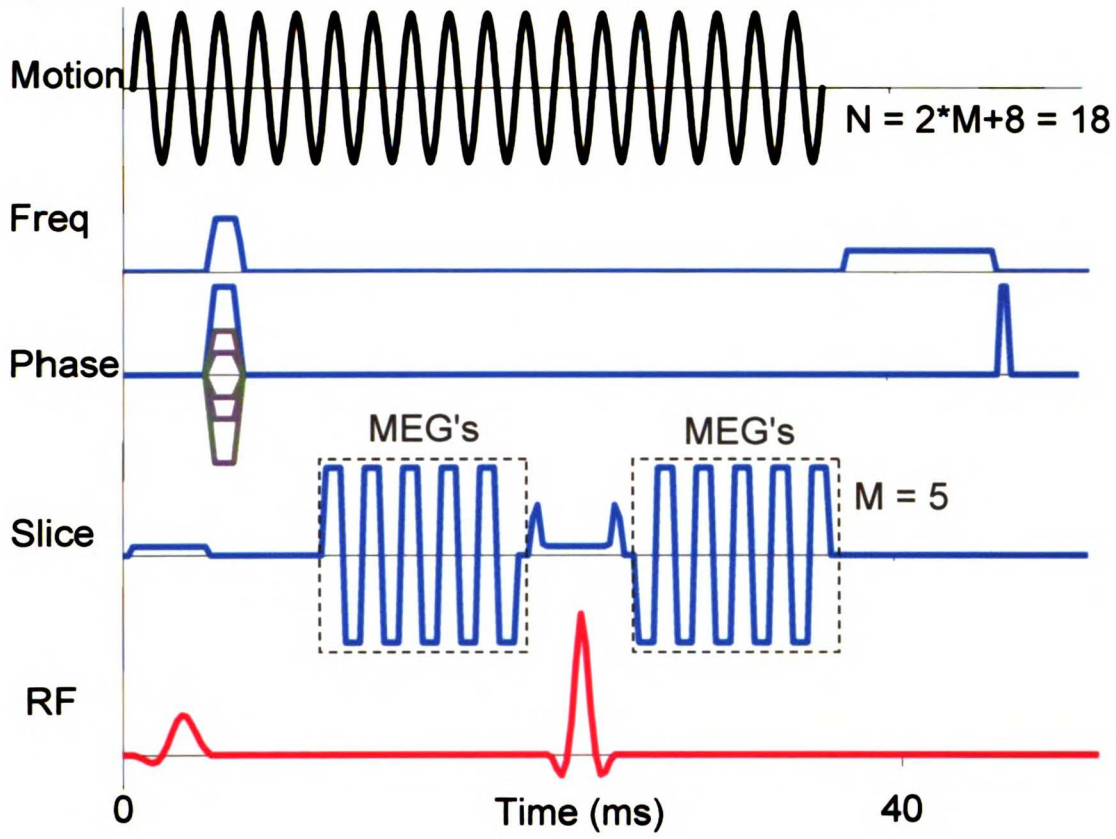
UWST LIDIANI



the cross-term on shear wave velocity were analyzed. Posttests were performed with the Student's t-test.

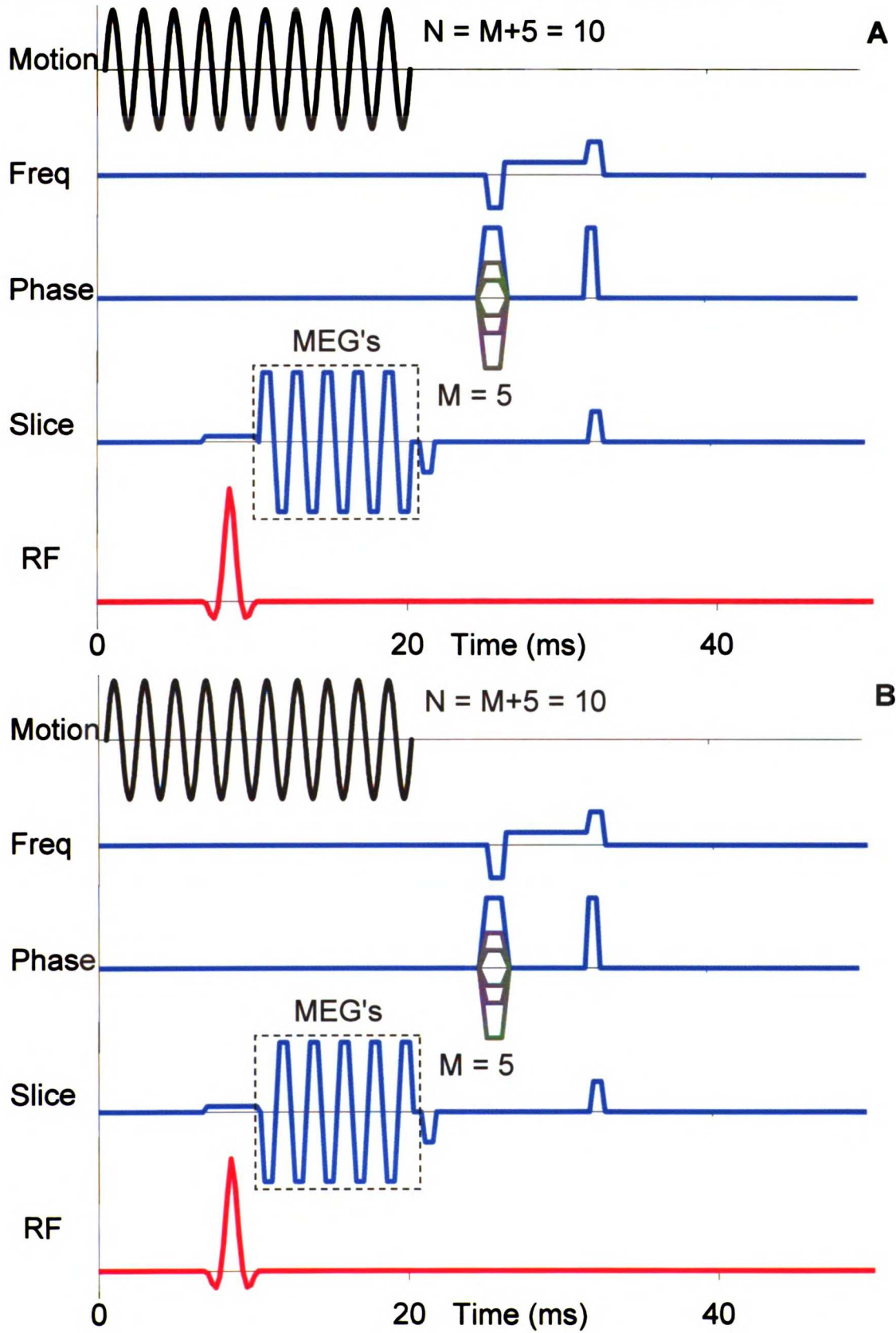
The relative performance of each technique was also determined by phase-to-noise ratio (PNR) maps. To calculate PNR, an absolute maximum intensity projection was performed across the eight wave images. This was divided by the arctangent of the inverse of the magnitude signal to noise ratio, which was found by dividing the magnitude images by the standard deviation of the signal in a region of air and averaging across the eight offsets. When comparing the SE and GRE methods at 500 Hz, the PNR was divided by the square root of the scan time to calculate PNR efficiency. Finally, a single region of interest (ROI) was chosen in the 1.0% agar region to compare the SE and GRE techniques (Figure 3-21A-B). Due to the artifacts with the GRE method, the ROI was chosen to be approximately 3 cm from the surface, beyond the region of signal loss. Phase wrap artifacts were removed by thresholding PNR values greater than 30 to be equal to zero for the GRE technique. At 500 Hz, the mean PNR efficiency in the ROI for the 6 experimental conditions was analyzed by a two-way ANOVA and Student's t-tests for posttests. All image processing was performed with Matlab (Mathworks, Natick, MA) and all statistical analyses were performed with JMP (SAS Institute, Cary, NC).

Figure 3-18. Pulse diagram for spin echo-based elastography sequence.

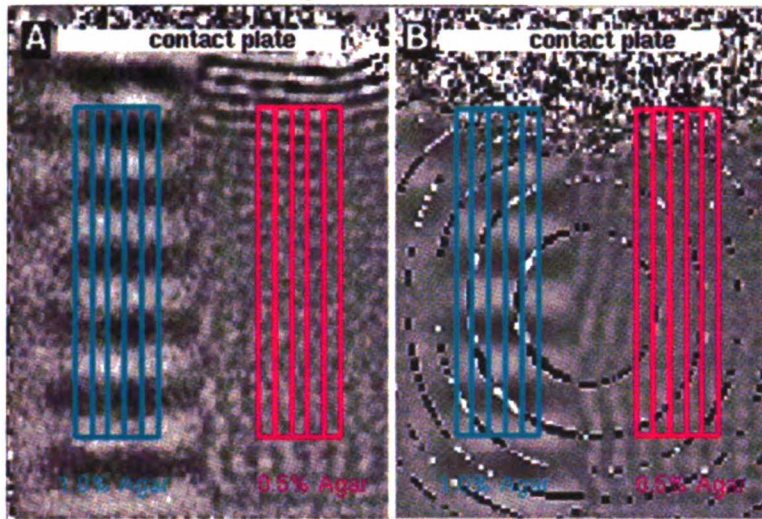


UJOT LIDIVAN I

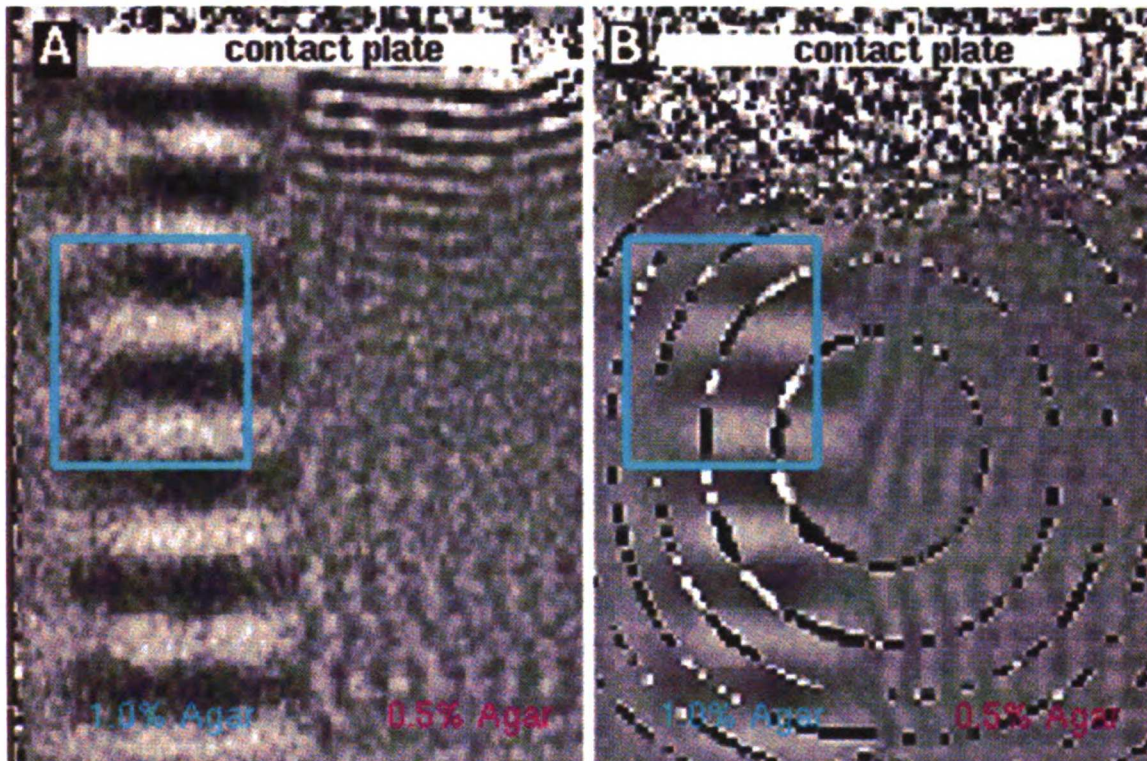
**Figure 3-19. Pulse diagram for gradient echo-based elastography sequence.**



**Figure 3-20. Example wave images for the SE (A) and GRE (B) methods at 500 Hz with ROIs for strain wavelength estimation.**



**Figure 3-21. Representative wave images with ROI location for PNR calculation comparing the SE (A) and GRE (B) methods at 500 Hz. M, number of MEG's = 15.**



### 3.2.3.2 Results

Shear waves were plainly visible in the wave images. Unlike a prior demonstration [106], the piezoelectric element was found to produce image artifacts for

the GRE technique to a depth of approximately 1 cm. The underlying phase distortions for the GRE method created several fringe lines of phase wrap which effectively removed any strain wave velocity information from those pixels. These two issues need to be addressed to make the GRE technique useful in practice, and are not present for the SE method. However, as found later, deriving the phase image from the acquired real and imaginary images solves this problem.

The estimates of strain wavelength ( $\lambda$ ), wave speed ( $c_s$ ), and shear modulus ( $G$ ) for each agar concentration, method, and number of MEGs combined across all five ROIs are shown in Table 3-4. The least squares linear regression model for the strain wavelength ( $\lambda$ ) for the effects of method, MEGs and ROIs in the 1.0% agar fit the data with a high level of significance ( $p = 0.0005$ ). A significant interaction of method and ROI was found ( $p = 0.0056$ ). Examination of the posttests found that while the SE method had no significant differences in estimates of  $\lambda$  (least squares mean = 9.58 mm) across different ROIs, the GRE method had significantly different  $\lambda$  estimates in different regions (Figure 3-22A and B). ROI 1, farthest from the center of the phantom, had  $\lambda$  estimates significantly higher ( $p < 0.05$ ) than ROIs 4 and 5. In addition,  $\lambda$  estimates in ROI 5 was significantly ( $p < 0.05$ ) lower than all other ROIs. Overall, the GRE least squares mean estimate of  $\lambda$  was 9.08 mm, and was significantly different than the SE method ( $\lambda = 9.57$ ,  $p < 0.05$ ).

The least squares linear regression model for the strain wavelength ( $\lambda$ ) for the effects of method, MEGs and ROIs in the 0.5% agar fit the data with a high level of significance ( $p = 0.0294$ ). Only the effect of method was found to be significant ( $p < 0.0001$ ), with the least squares mean estimate of  $\lambda$  of 2.81 mm for the SE method and 5.21 mm for the GRE method. No effect of ROI was found (Figure 3-22C and D).

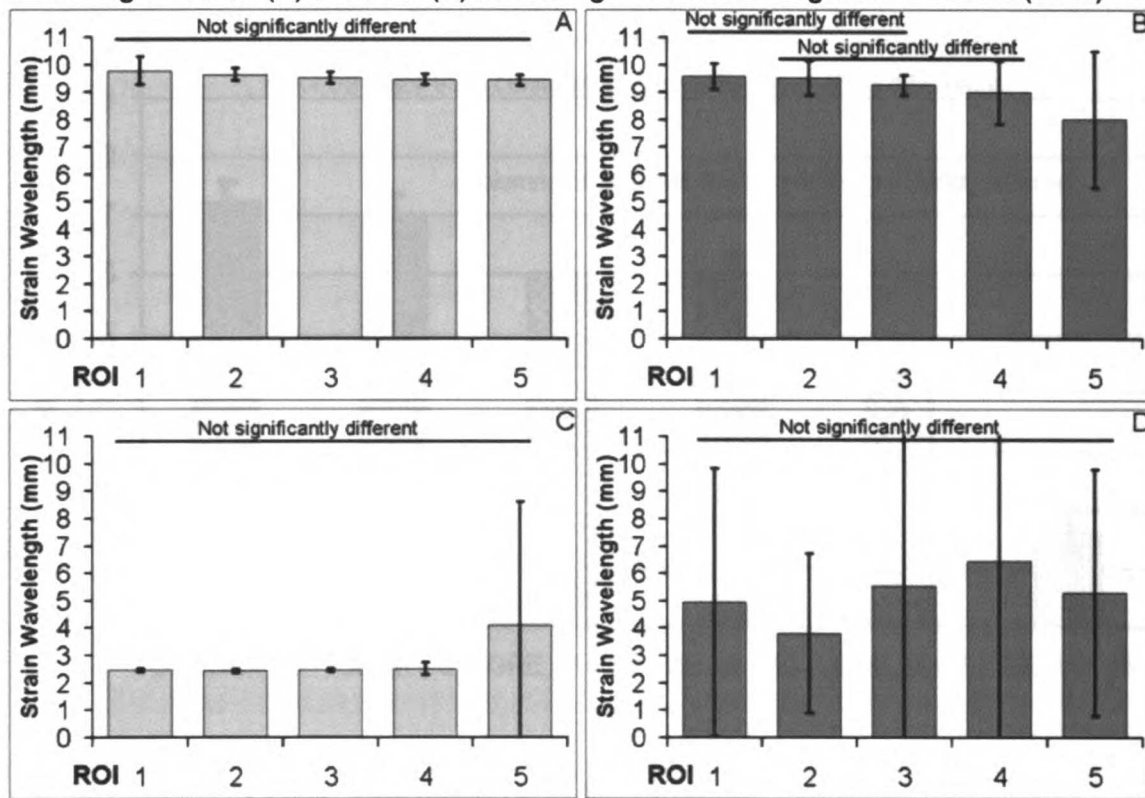
The model for the strain wave velocity ( $c_t$ ) for the effects of motion frequency and ROIs fit the data with a high level of significance ( $p < 0.0001$ ). Only the effect of frequency was found to be significant ( $p < 0.0001$ ), with four significantly different groups of shear wave velocities, ranging from 4.97 m/s to 3.96 m/s (Figure 3-15).

For the phase-to-noise ratio efficiency calculation, the comparison of PNR efficiency in the ROI for the different methods found significant differences (Figure 3-23). The "GRE, M=10" and "SE, M = 5" had significantly higher PNR efficiency compared to all other conditions ( $p < 0.05$ ). This result shows that the same PNR efficiency can be achieved with one half the number of motion encoding gradients and a longer TE by the SE technique compared to the GRE technique. The PNR efficiency of the "GRE, M = 15" and "SE, M = 10" conditions were statistically equivalent, and significantly higher than the "GRE, M = 5" and "SE, M = 15" conditions ( $p < 0.05$ ). The "SE, M = 15" condition had the lowest PNR efficiency, and was significantly lower than the "GRE, M = 5" condition ( $p < 0.05$ ).

**Table 3-4. Strain wavelength ( $\lambda$ ), wave speed ( $c_t$ ), and shear modulus (G) estimates for each agar concentration, method, and number of MEGs in all five ROIs combined. Values are (average  $\pm$  1 standard deviation).**

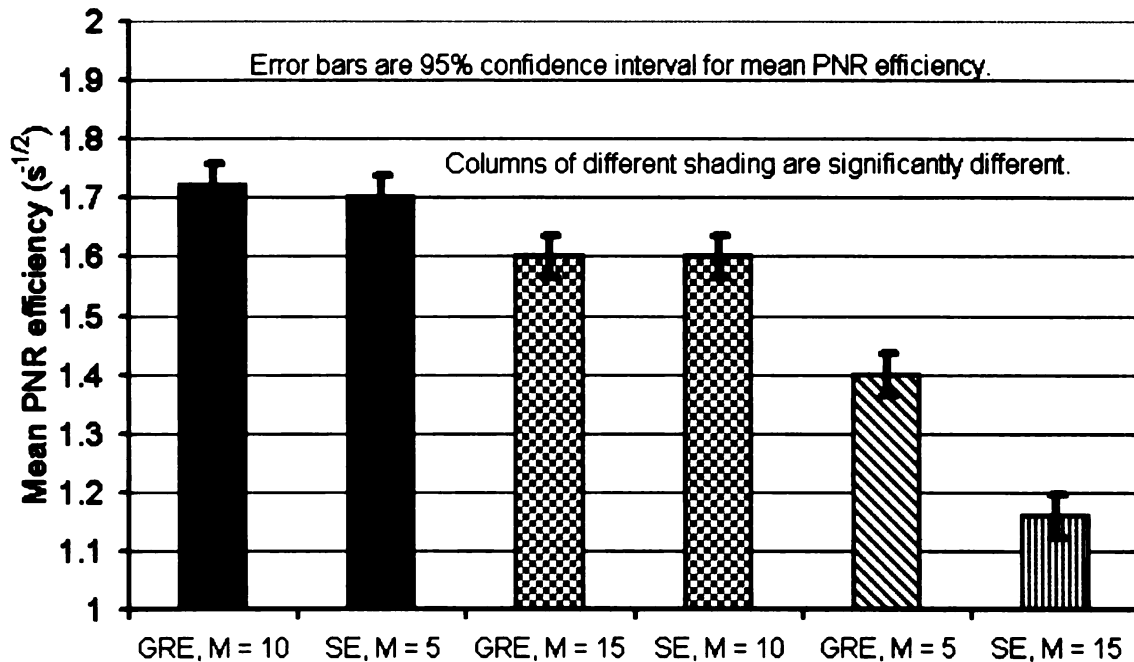
| Agar          |        |      |                 |                 |                   |
|---------------|--------|------|-----------------|-----------------|-------------------|
| Concentration | Method | MEGs | $\lambda$ (mm)  | $c_t$ (m/s)     | G (kPa)           |
| 0.5%          | GRE    | 5    | 4.69 $\pm$ 5.35 | 2.34 $\pm$ 2.67 | 12.51 $\pm$ 28.79 |
|               |        | 10   | 5.63 $\pm$ 5.83 | 2.81 $\pm$ 2.91 | 16.24 $\pm$ 28.49 |
|               |        | 15   | 5.31 $\pm$ 4.54 | 2.65 $\pm$ 2.27 | 12.1 $\pm$ 20.75  |
|               | SE     | 5    | 3.52 $\pm$ 3.54 | 1.76 $\pm$ 1.77 | 6.17 $\pm$ 17.57  |
|               |        | 10   | 2.49 $\pm$ 0.17 | 1.24 $\pm$ 0.08 | 1.56 $\pm$ 0.24   |
|               |        | 15   | 2.41 $\pm$ 0.13 | 1.2 $\pm$ 0.06  | 1.46 $\pm$ 0.15   |
| 1.0%          | GRE    | 5    | 8.92 $\pm$ 1.57 | 4.46 $\pm$ 0.78 | 20.52 $\pm$ 5.26  |
|               |        | 10   | 9.2 $\pm$ 1.15  | 4.6 $\pm$ 0.57  | 21.5 $\pm$ 3.94   |
|               |        | 15   | 9.11 $\pm$ 1.43 | 4.55 $\pm$ 0.71 | 21.28 $\pm$ 5.25  |
|               | SE     | 5    | 9.6 $\pm$ 0.31  | 4.8 $\pm$ 0.15  | 23.1 $\pm$ 1.55   |
|               |        | 10   | 9.54 $\pm$ 0.33 | 4.77 $\pm$ 0.16 | 22.78 $\pm$ 1.68  |
|               |        | 15   | 9.57 $\pm$ 0.29 | 4.78 $\pm$ 0.14 | 22.95 $\pm$ 1.46  |

**Figure 3-22. Strain wavelength ( $\lambda$ ) estimates for the SE (A) and GRE (B) methods at 500 Hz in 1.0% agar and SE (C) and GRE (D) in 0.5% agar for the five regions of interest (ROIs).**



WAVELENGTH

**Figure 3-23. ANOVA results comparing mean Phase-to-Noise Ratio efficiency for the techniques tested at 500 Hz.**



### 3.2.3.3 Discussion and Conclusions

The strain wavelength and shear stiffness estimates found in this study are higher than those found in similar studies. Hamhaber [85] found shear stiffness values of ~4.5 and ~15 kPa for 0.5% and 1.0% agar phantoms, respectively. Uffman [62] reported 1.0% agar phantom shear stiffness values of ~12 kPa. However differences in image processing and phantom may account for the inconsistencies. Hamhaber used a manual technique to determine strain wavelength, while Uffman had good agreement with both manual and automated strain wavelength methods. The present technique is limited compared to Uffman, et al.'s in that the wave direction is determined by the maximum gradient of all three dimensions. In this study, the analysis assumed waves traveled only away from the contact plate. Obvious reflections and distortions from the interface of the agar regions were evident, so the assumption of wave propagation direction may lead to errors in wavelength estimation. In addition, differences in the type



of agar and in the specific mixing and preparation methods may account for some discrepancies.

The reason the GRE method had more inconsistent wavelength estimates compared to the SE method is likely due to two reasons: noise from the piezoelectric actuator and phase wrap fringe effects. Analysis of the individual, outlier strain wavelength estimates showed that the ROI 5 had several cases which crossed phase fringe lines that would pass extreme values through the median filter. In addition, the effect of the dephasing of the signal due to the piezoelectric actuator added substantial noise to the portion of the ROI closest to the actuator that would create a noisier frequency power spectrum. These factors are likely to be the cause of finding a significant effect of ROI on the 1.0% agar  $\lambda$  estimates for the GRE method.

The relationship of the number of MEGs and the PNR efficiency was found to be different for the SE and GRE methods. While the  $M = 5$  condition was best for the SE technique, it was worst for the GRE condition. However, this effect could be explained by the compromise necessary in elastography between the number of MEGs and TE. While the MEGs theoretically linearly add phase to the signal, the increased TE will increase noise. Since all conditions for the GRE method operated in a domain of relatively short TE's, increasing the MEGs would benefit the PNR efficiency. However, the SE method was operating at relatively longer TE's, and the increased noise from the addition of more MEGs overwhelms their benefit, lowering the PNR. Therefore, care should be taken to optimize the TE and number of MEGs depending on the T2 of the object of interest.

Attempts were made to remove the phase fringe effects for the GRE method, both Goldstein's and the quality-guided phase unwrapping techniques (sections 2.4.2.3 and 2.4.2.4) [110] were implemented and used to try to unwrap the phase images – which, for these experiments, were reconstructed by the scanner. However, both were

unsuccessful due to the relatively large noise in the wrap transition regions, and therefore artifact remained along the phase wrap locations. Unwrapping was successful if the fringe artifacts were replaced with interpolated phase values. However, the strain velocity information is still lacking in this case, and so these images were not analyzed. This problem was overcome in later studies by finding the complex phase difference from the real and imaginary images (see section 2.4.1).

The shear wave images were processed in a manner suggested by Denk et al. [18], where the difference of wave images with exactly opposite motion phase was found. The results are not presented in detail here, but only mentioned to acknowledge that the PNR can be effectively doubled for any particular technique. However, the relative, significant differences in PNR found between techniques did not change, nor did shear wavelength or wave velocity estimates change significantly.

The present study provides a direct comparison of two MR elastography techniques at 3T. The SE method was found to be superior from the practical fact of not producing phase wrap fringe artifacts. In addition, the piezoelectric actuator was found to be a severe problem for the GRE method, causing signal drop-out up to 1 cm into the phantom. Obviously different actuator designs could address this problem, but the SE method was found, as would be expected, to be more robust and insensitive to these field inhomogeneities.

Taking the knowledge gained during the implementation phase of the present work, the elastography method was applied to agar gels to validate the method against traditional compressive mechanical testing. Secondly, the elastography method was applied to bovine intervertebral disc samples with controlled hydration and simulated degradation with the enzyme papain. These results provide the basis of demonstrating the utility of the method to detect tissue changes similar to those experience with disease.

#### 4.1 Embedded Gel samples

Gel phantoms designed with inclusions in a homogeneous background provide a model for biological tissue features of interest. Depending on the goal of a particular experiment, the elastographic technique may be primarily concerned with the detection of regions of increased or decreased stiffness, or the quantification of tissue stiffness in a particular region, or ideally, both. It should be understood, however, that spatial detection resolution and stiffness resolution are related. The limits of detection are more detailed than limits of quantification, since quantification has higher requirements for resolving shear motion. In a pilot study, two agar gel phantoms were created and experiments were performed to assess how these parameters are related. Both phantoms had homogeneous 1.0% agarose backgrounds. One phantom had three 2.5% agarose cylinders of different sizes, while the other had two cylindrical inclusions of different agarose concentration (2.5% and 0.5%) of the same diameter. In a broader study – the “comprehensive” study – ten different agar concentrations were made into mechanical test specimens and inclusion phantoms to assess the agreement between shear modulus estimates from compression tests and elastography.

## **4.1.1 Pilot Study of Agar Stiffness with Elastography and Mechanical Testing**

### **4.1.1.1 Detection of inclusions**

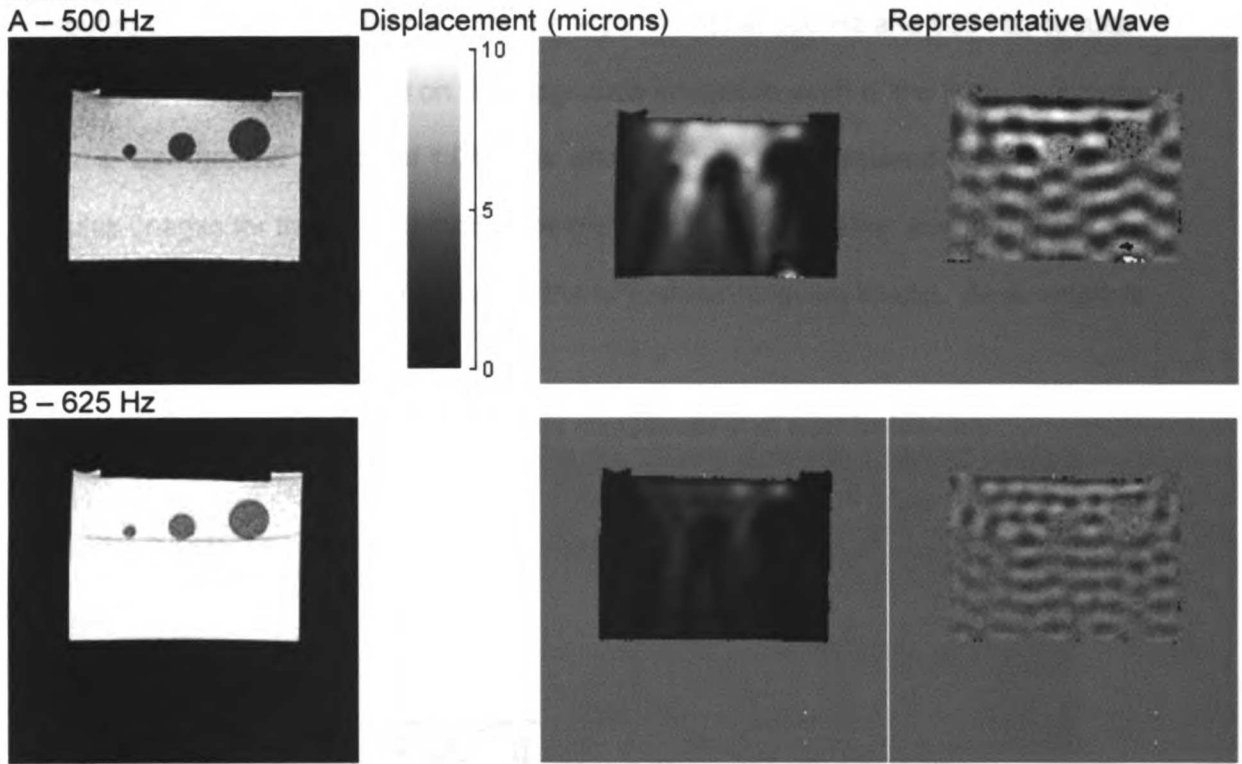
An agarose phantom with a homogeneous 1.0% background was constructed with three cylindrical inclusions of 2.5% agarose. The inclusions had diameters of 3.2, 6.45, and 9.5 mm. The cylinders were arranged so that an axial view of the phantom revealed the circular cross-section of the inclusions, as shown in the magnitude image in Figure 4-1.

Two experiments were performed using the spin-echo elastography method at 500 and 625 Hz. Sixteen offsets were acquired, at each eighth of the shear wave period with the motion phase starting at 0 and 180 degrees. The voltage output of the wave generator was set to 7 V, the maximum amplitude of the MEGs was 3.5 G/cm, with ten MEGs before and after the 180 degree refocusing pulse on the slice selection axis. The TE/TR was set to 20/175 ms, the bandwidth was 15.6 kHz, and the field of view was 12 cm with a slice thickness of 5 cm. The acquired matrix was 256x160, NEX = 1, and the frequency direction was right-to-left for the axial plane acquisition.

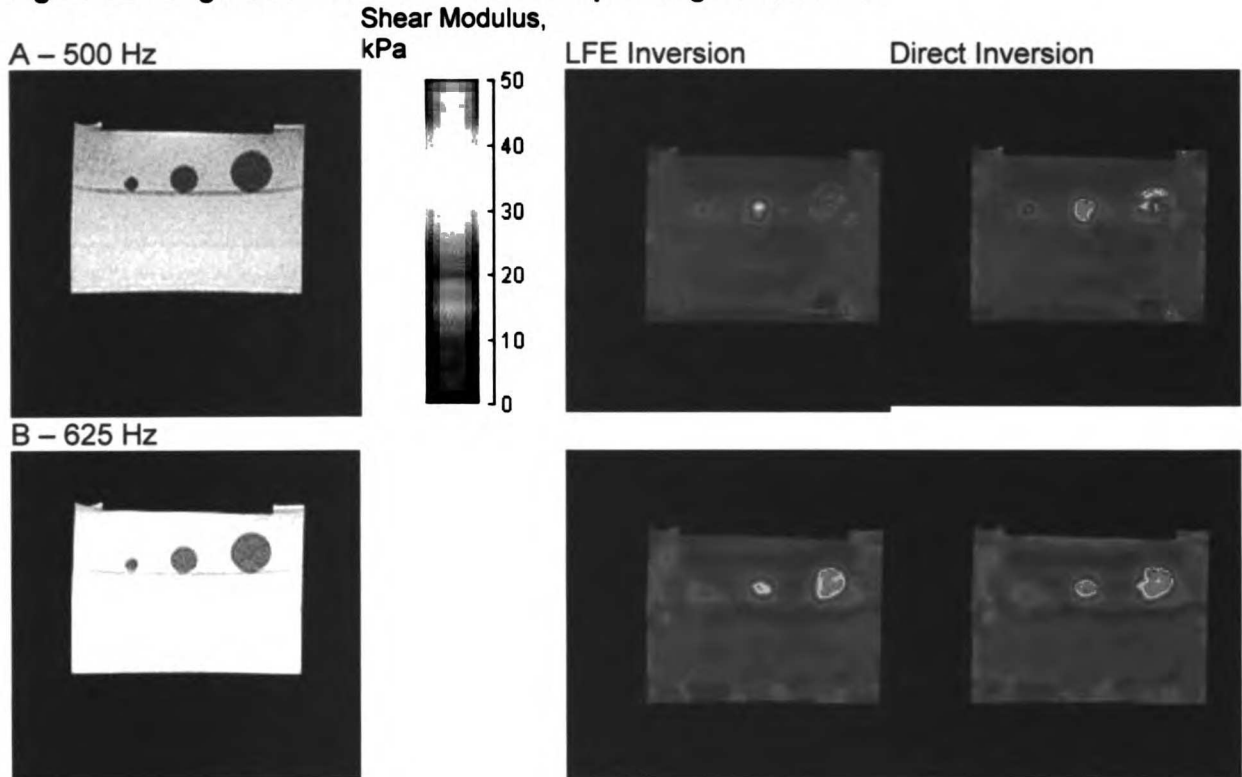
The MREView program was used to analyze the wave images from the experiment. The maximum displacement of each voxel was determined and shown in Figure 4-1. For inversion of the wave images into a shear modulus estimate, both the

UNIVERSITY OF MICHIGAN

**Figure 4-1. Magnitude, displacement amplitude, and representative wave image for agar inclusions.**



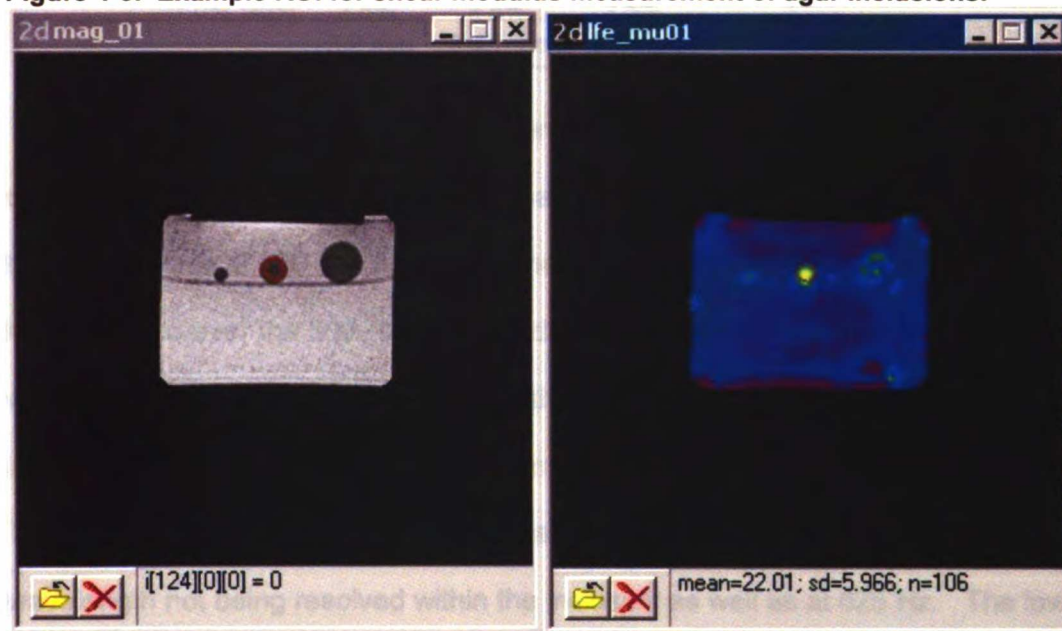
**Figure 4-2. Magnitude and shear modulus maps for agar inclusions.**



www.lidi.com

Local Frequency Estimation (LFE) [111] and Direct Inversion (DI) [31] results were computed as shown in Figure 4-2. For the experiments at 500 Hz and 625 Hz, circular regions of interest were placed on the magnitude images in each of the three inclusions and in a “background” region of 1.0% agar and automatically registered to the shear modulus images for the LFE method. The mean, standard deviation and number of voxels were recorded for each region on the LFE shear modulus image. An example is shown in Figure 4-3.

Figure 4-3. Example ROI for shear modulus measurement of agar inclusions.

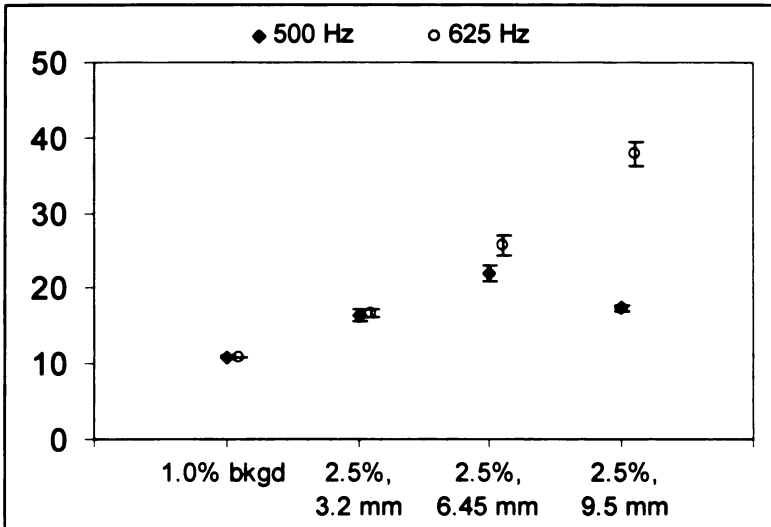


The results of the study are summarized in Table 4-1, which has the mean shear modulus of each region of interest and its 95% confidence interval.

Table 4-1. Shear modulus results for detection of inclusions experiment.

| Shear Modulus (kPa)<br>Mean $\pm$ 95% CI | 500 Hz           | 625 Hz           |
|--|------------------|------------------|
| 1.0% background                          | 10.93 $\pm$ 0.1  | 10.88 $\pm$ 0.07 |
| 2.5%, 3.2 mm dia.                        | 16.4 $\pm$ 0.7   | 16.58 $\pm$ 0.52 |
| 2.5%, 6.45 mm dia.                       | 22.01 $\pm$ 1.13 | 25.69 $\pm$ 1.31 |
| 2.5%, 9.5 mm dia.                        | 17.36 $\pm$ 0.39 | 37.81 $\pm$ 1.54 |

**Figure 4-4. Shear modulus results for detection of inclusions experiment.**



As shown in the table and in Figure 4-4, all of the inclusions were found to be significantly ( $p < 0.05$ ) greater than the background. No difference was found between the experiments at 500 and 625 Hz for the background and the 3.2 mm diameter inclusion; however the 500 Hz shear modulus estimates for the two largest inclusions were significantly lower than those from the 625 Hz experiment. For the 9.5 mm inclusion, there is considerable disagreement between the 500 Hz and 625 Hz methods. The possible explanation for this discrepancy would be due to the 500 Hz shear wavelength not being resolved within the inclusion as well as at 625 Hz. The lower shear modulus estimates of the smaller inclusions shows the effect of underestimating the shear modulus when the shear wave is not fully resolved in the object, and the effect seems to be affecting the 500 Hz case more than the 625 Hz case. In addition, the TE for the 625 Hz is shorter, 52 ms compared to 60 ms for the 500 Hz condition. The resulting small additional SNR may allow more accurate shear modulus calculation from the 625 Hz condition.

UNIVERSITY OF MICHIGAN

#### **4.1.1.2 Quantification of stiffness**

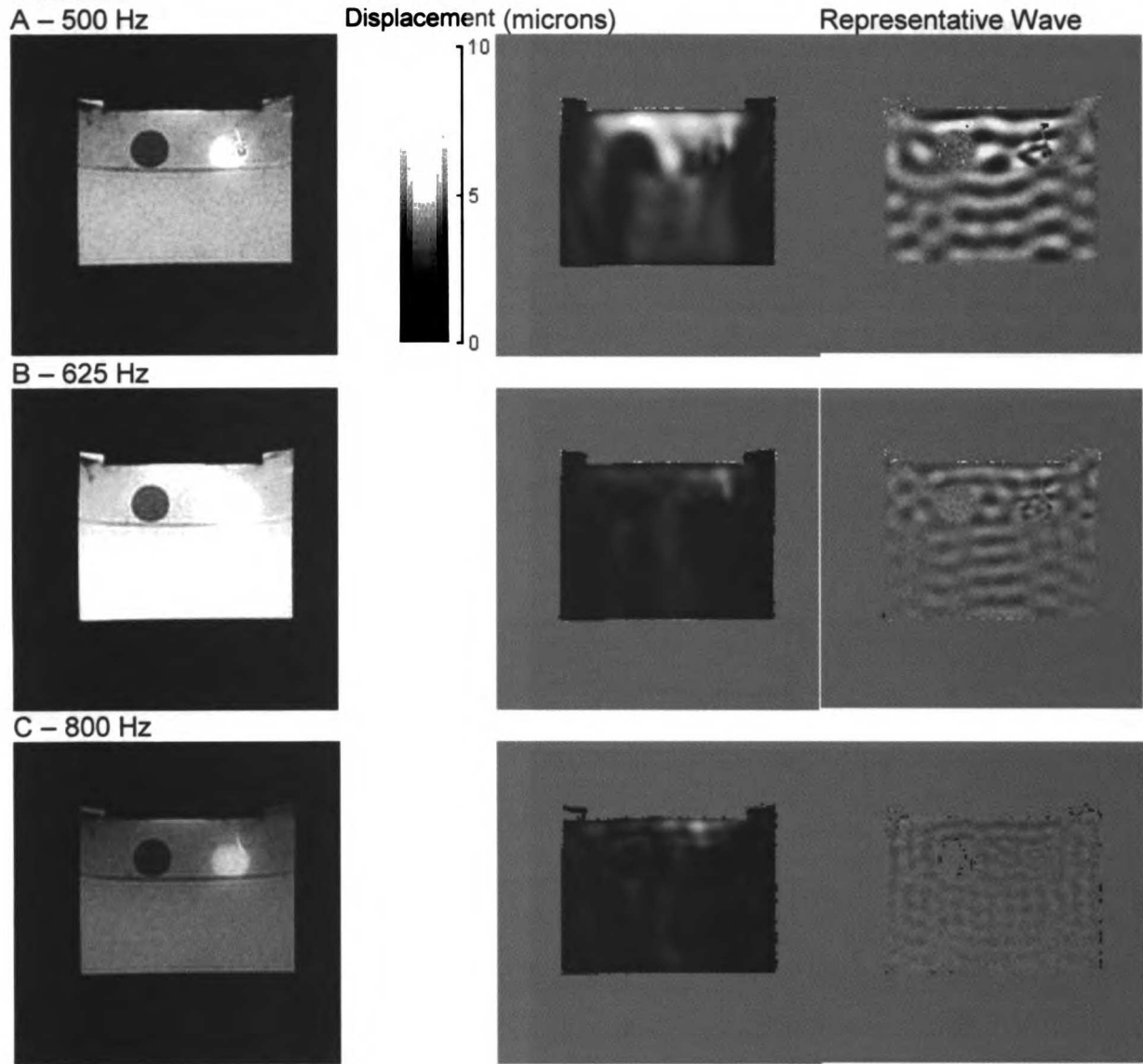
An agarose phantom with a homogeneous 1.0% background was constructed with two cylindrical inclusions of 0.5% and 2.5% agarose. The inclusions had diameters of 9.5 mm. The cylinders were arranged so that an axial view of the phantom revealed the circular cross-section of the inclusions, as shown in the magnitude image in Figure 4-5.

Three experiments were performed, using the spin-echo elastography method at 500, 625, and 800 Hz. Except for the addition of the 800 Hz experiment, the method was identical to the experiment used for the detectability experiment in section 4.1.1.1. Sixteen offsets were acquired, at each eighth of the shear wave period with the motion phase starting at 0 and 180 degrees. The voltage output of the wave generator was set to 7 V, the maximum amplitude of the MEGs was 3.5 G/cm, with ten MEGs before and after the 180 degree refocusing pulse on the slice selection axis. The TE/TR was set to 20/175 ms, the bandwidth was 15.6 kHz, and the field of view was 12 cm with a slice thickness of 5 cm. The acquired matrix was 256x160, NEX = 1, and the frequency direction was right-to-left for the axial plane acquisition.

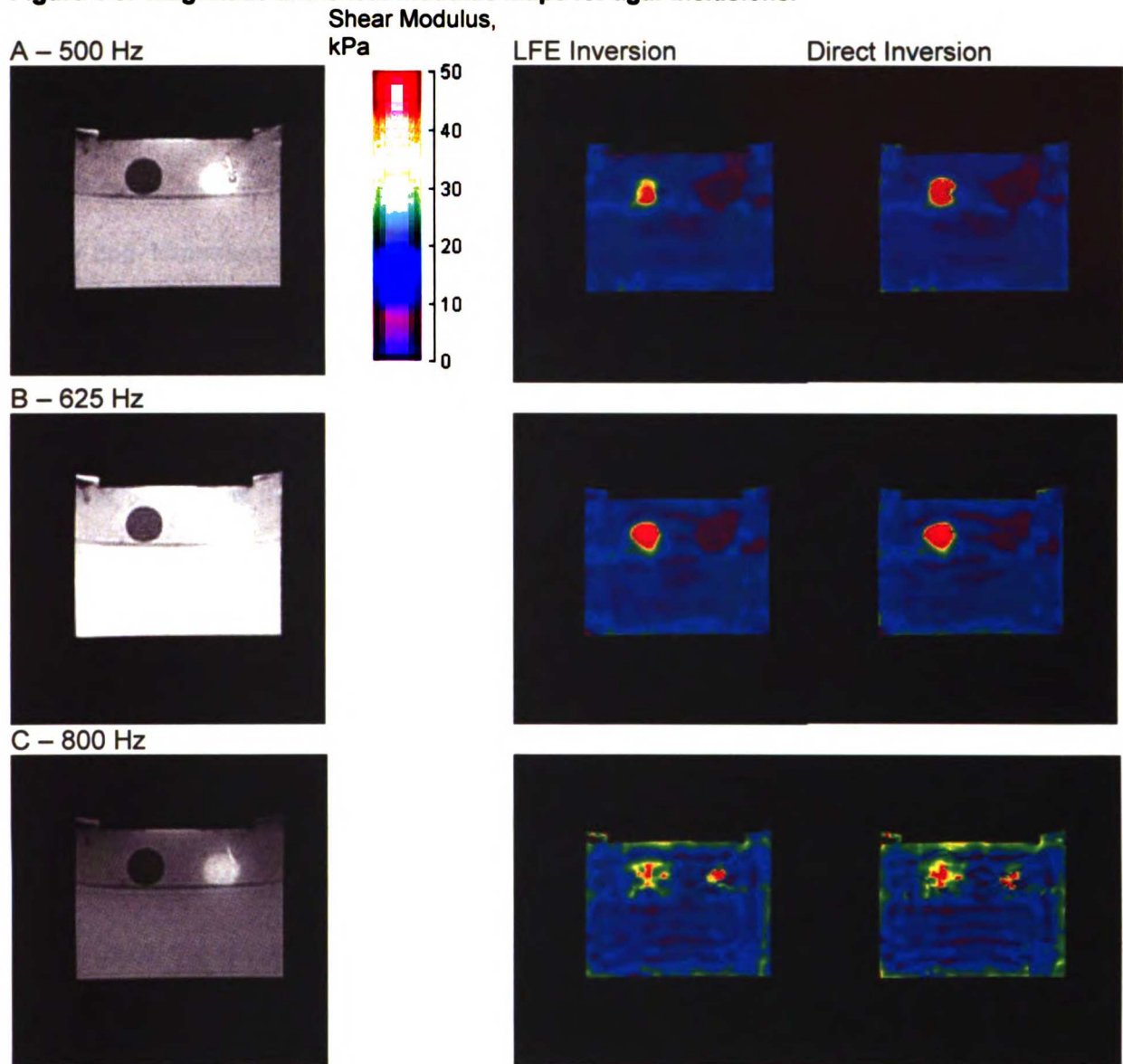
UWU LINDA



**Figure 4-5. Magnitude, displacement amplitude, and representative wave image for agar inclusions.**



**Figure 4-6. Magnitude and shear modulus maps for agar inclusions.**



For the elastography experiments performed at 500 and 625 Hz, regions of interest were drawn in areas with different agar concentration to find shear modulus estimates for each Agar concentration. The 800 Hz condition resulted in shear wave phase amplitude that were insufficiently large for shear stiffness inversion. This result agrees with earlier analysis of the effect of frequency on shear wave sensitivity.

### 4.1.1.3 Comparison to Mechanical Testing

From the same Agar gel batches used to create the imaging phantoms, cylindrical samples (dia = 2 cm, height = 1.5 cm) were cast for compression testing. Compressing tests were performed by a servohydraulic materials testing system (MTS Bionix 858, Minneapolis, MN) with non-porous platens on the top and bottom of the sample.

Four samples of 2.5% were tested, while only two samples of 1.0% and 0.5% were tested. The slope of the load-displacement curve was used to find the Young's modulus, which was then converted to shear modulus. The Young's modulus is defined as [2]:

$$E = \frac{\sigma}{\varepsilon} = \frac{A_0}{l_0} \frac{\Delta F}{\Delta l} = \frac{l_0}{A_0} * \frac{\Delta F}{\Delta l} \quad [29]$$

where  $\sigma$  is the stress and  $\varepsilon$  is the strain the material is experiencing. Since stress is defined as the applied load ( $\Delta F$ ) per cross-sectional area ( $A_0$ ), and strain is the change in length ( $\Delta l$ ) of the specimen relative to the original length ( $l_0$ ), the Young's modulus can be defined in terms of the load-displacement relation as shown in the equation above. For an isotropic material, such as agar gel, Young's modulus ( $E$ ) can be converted to shear modulus ( $G$ ) by [2]:

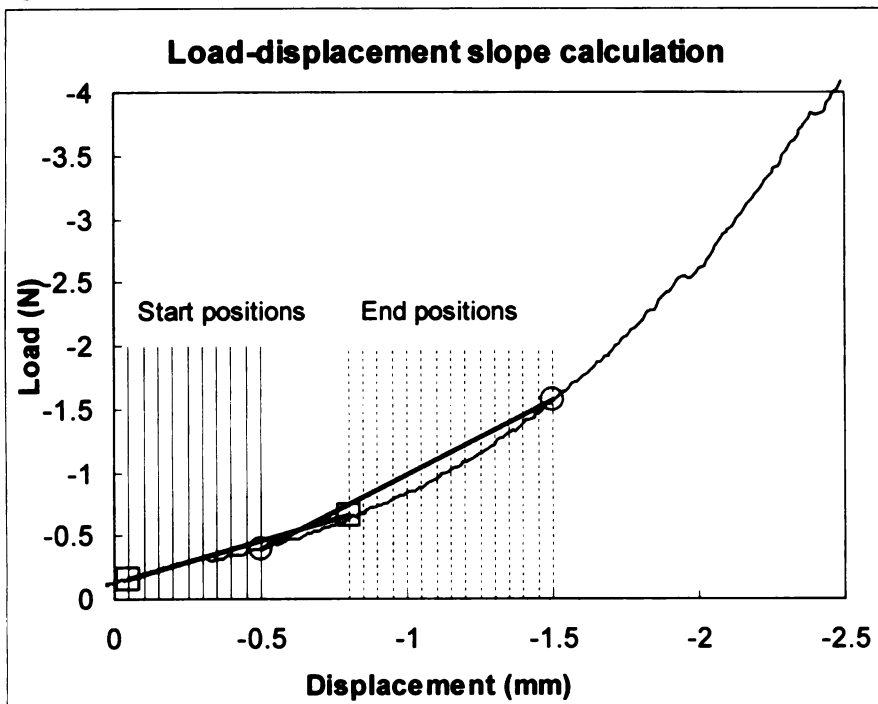
$$G = \frac{E}{2(1+\nu)} \quad [30]$$

where  $\nu$  is the Poisson's ratio of the material. An incompressible material, such as water, has a Poisson's ratio of 0.5. Agar gel, being composed of almost entirely water, has a Poisson's ratio approximately 0.495, a value used by other investigators [85].

UNIVERSITY OF MINNESOTA

Shear modulus values were found via the load-displacement curve in the region of initial displacement of varying start positions (0.05 to 0.5 mm) and change in displacement (0.75 to 1 mm). A representative load-displacement curve is shown in Figure 4-7, with increasing compressive load and displacement being represented by increasingly negative load and displacement values. The entire set of start and end locations used to determine the slope of the curve is shown. However, not all end positions were paired with the start positions for the analysis, but only those that had a change in displacement between 0.75 mm and 1.0 mm, resulting in sixty slope measurements. For reference, the lowest start position (-0.05 mm) and lowest change in displacement (0.75 mm) is shown with a square outline symbol, while the highest start position (-0.5 mm) and highest change in displacement (1 mm) is shown with a circle outline symbol. The average and standard deviation of the sixty slope measurements were computed and used to represent the shear modulus of the gel.

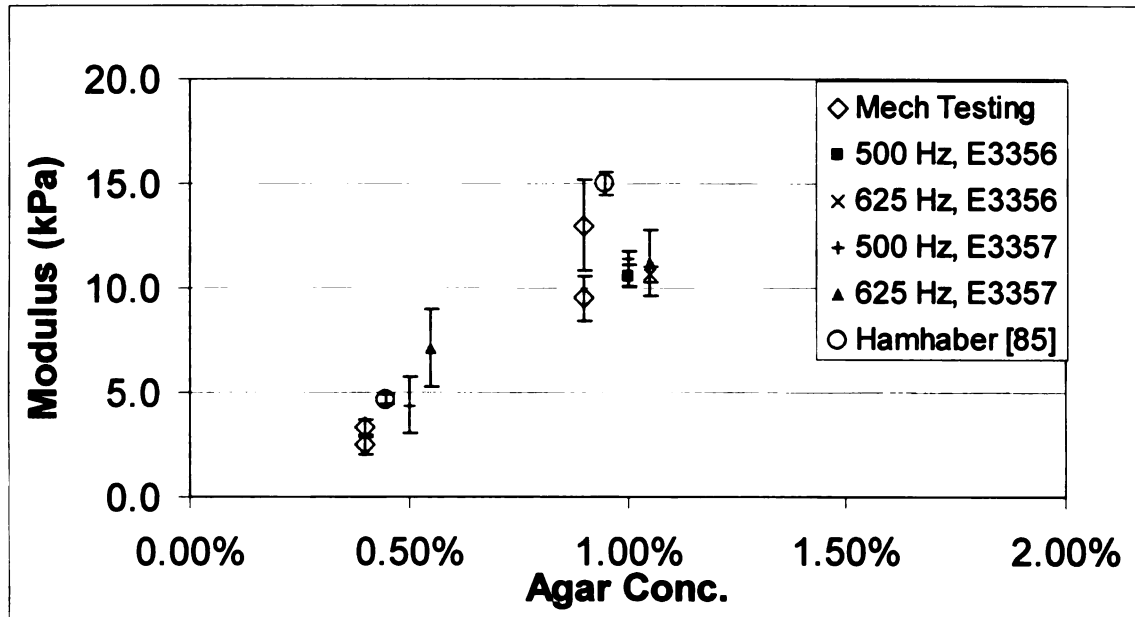
**Figure 4-7. Example load-displacement curve for Agar gel (1.0%) compression test.**



The resulting shear modulus estimates from the mechanical testing and the elastography experiments are shown in Figure 4-8 and Figure 4-9. For comparison to results found in the literature, the approximate elastographic shear modulus values reported by Hamhaber and co-workers [85] are also reported.

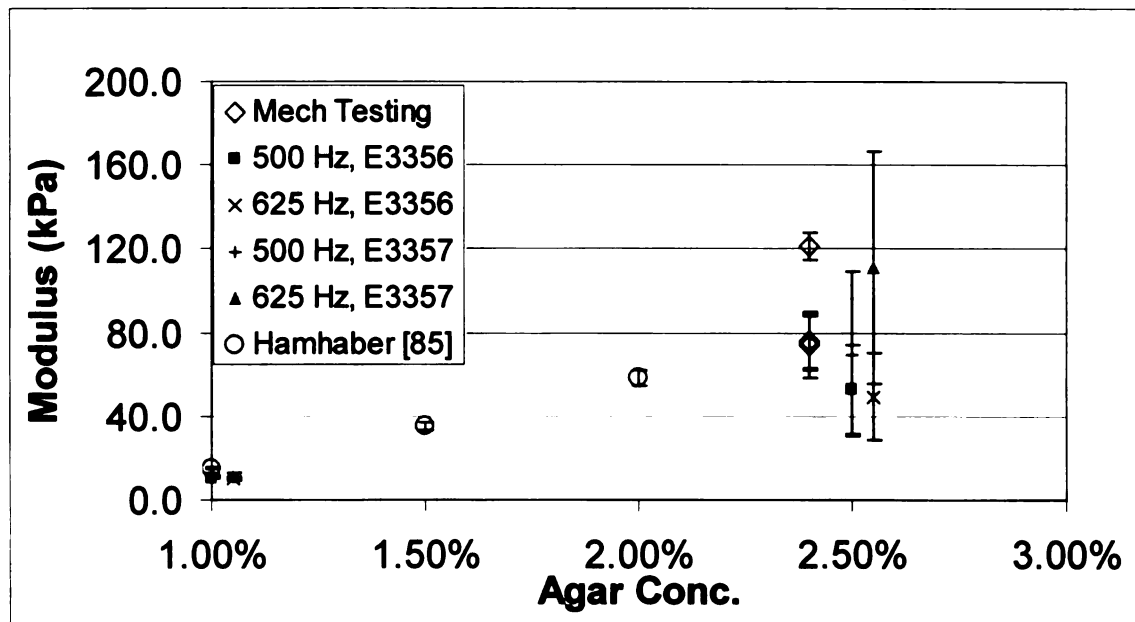
UWI LIBRARY

**Figure 4-8. Shear modulus estimate comparison, low concentration agar**



Error bars are  $\pm 1SD$

**Figure 4-9. Shear modulus estimate comparison, high concentration agar**



Error bars are  $\pm 1SD$

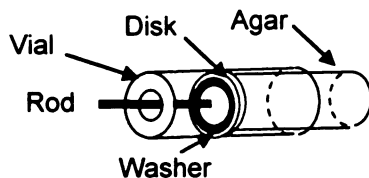
#### 4.1.2 Comprehensive Agar Stiffness Study

To achieve finer detail of the relationship between agar gel concentration and shear modulus, a more comprehensive study was done. For this study, ten agar gel

concentrations were made with purified water and 0.5mM GAD: 0.5, 0.625, 0.75, 0.875, 1.0, 1.125, 1.25, 1.5, 1.75 and 2.0%. For each batch, three cylinders were cast into plastic vials, two for mechanical testing (approximately 1.5 cm tall), and one for elastography (approximately 3 cm tall). All vials had an internal diameter of 20.3 mm. The 1.5 cm samples were used for mechanical testing, and the 3 cm samples were embedded in pairs in a homogeneous background of 1.0% agar gel for elastography imaging. The five phantoms for elastography imaging had inclusion pairs of 0.5% and 0.625%, 0.75% and 1.0%, 0.875% and 1.125%, 1.25% and 1.5%, and 1.75% and 2.0%.

In order to remove the cured gel samples, the vials had a plastic disk attached to the bottom with a plasticine “washer” between the disk and bottom of the vial. This washer seals the disk to the bottom of the vial and prevents leaking of the agar gel before curing. By pushing a rod (such as a paper clip) through the hole in the bottom of the vial, the plastic disk pushes the soft, brittle agar cylinder to be out of the vial without damage, as shown in Figure 4-10.

**Figure 4-10. Cylindrical vial cast for agar gel and removal.**



#### 4.1.2.1 Elastography

The embedded agar cylindrical inclusions were imaged with the spin echo-based elastography method with ten motion encoding gradients and 28 motion cycles at 500 Hz. Sixteen delay offsets were acquired at every eighth (0, .25, .5, .75, 1, 1.25, 1.5, 1.75 ms) of the motion period with a starting phase of 0 and 180 degrees. Therefore, the scan time for each phantom was approximately eight minutes. The phantom with 1.0% and 0.75% inclusions was scanned twice. For comparison to mechanical testing, the

www.livsci.com

1. The first part of the document is a list of names and addresses of the members of the committee. The names are listed in alphabetical order, and the addresses are listed below each name. The list includes names such as Mr. J. H. Smith, Mr. J. B. Jones, and Mr. W. C. Brown.

2. The second part of the document is a list of the names and addresses of the members of the committee who were present at the meeting. The names are listed in alphabetical order, and the addresses are listed below each name. The list includes names such as Mr. J. H. Smith, Mr. J. B. Jones, and Mr. W. C. Brown.



shear modulus values for these concentrations were averaged from the two measurements.

The complex difference image was found at each delay timepoint with starting phases of 0° and 180° degrees using the equation:

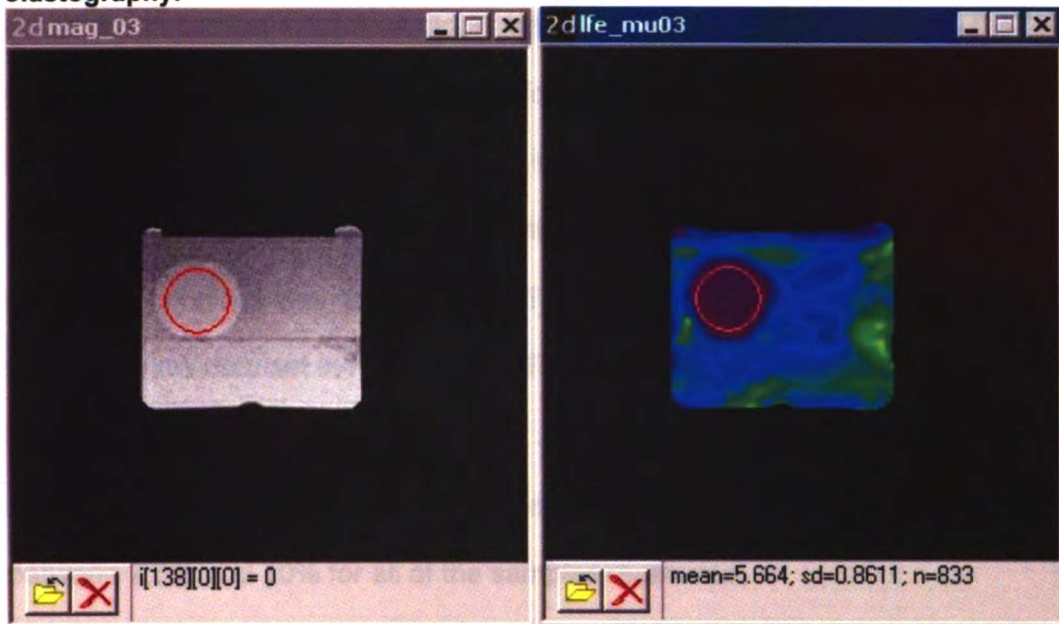
$$PhaseDiff = \text{atan2}\left(\text{Im}(Z1 \bullet Z2^*), \text{Re}(Z1 \bullet Z2^*)\right). \quad [31]$$

where  $\text{atan2}$  is the four-quadrant arctangent function,  $Z1$  is the complex image with 0° motion phase,  $Z2$  is the complex image with 180° motion phase,  $*$  is complex conjugation, and  $\bullet$  is element-by-element matrix multiplication. The MREView program was used to determine the shear modulus image from the eight phase difference images using the Local Frequency Estimation (LFE) method [111]. A circular region of interest (ROI) was placed on the magnitude image with a 33 pixel diameter. The ROI was automatically registered onto the shear modulus image, and the mean and standard deviation was found. An example ROI in 0.75% agar is shown in Figure 4-11.

1. The first part of the document is a list of names and addresses of the members of the committee. The names are listed in alphabetical order, and the addresses are listed below each name. The list includes names such as Mr. J. H. Smith, Mr. W. B. Jones, and Mr. C. D. Brown, along with their respective addresses in various cities and states.

2. The second part of the document is a list of names and addresses of the members of the committee. The names are listed in alphabetical order, and the addresses are listed below each name. The list includes names such as Mr. J. H. Smith, Mr. W. B. Jones, and Mr. C. D. Brown, along with their respective addresses in various cities and states.

**Figure 4-11. Representative agar gel inclusion shear modulus determined by elastography.**



#### **4.1.2.2 Mechanical Testing**

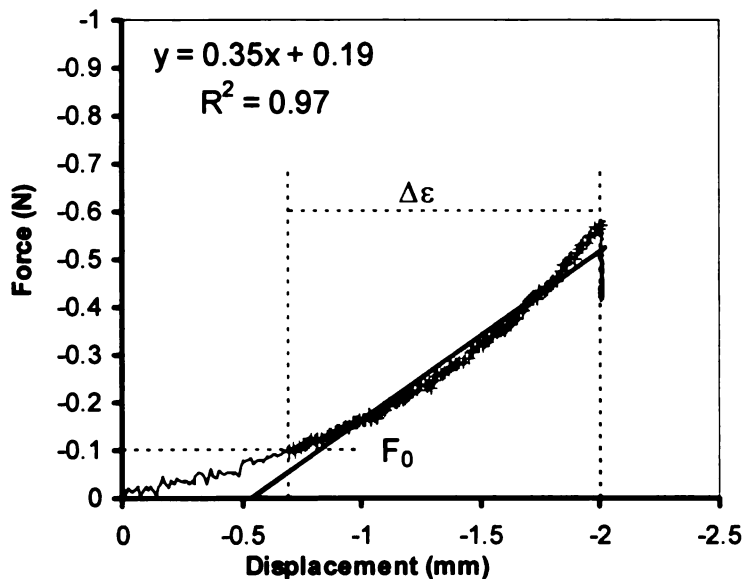
Compressing tests were performed by a servohydraulic materials testing system (MTS Bionix 858, Minneapolis, MN) with non-porous platens on the top and bottom of the sample. The upper, movable platen was manually lowered to the top surface of each sample and the position measurement was zeroed. The loading protocol was to compress the sample by 2 mm at a rate of 1 mm per second, hold for 3 seconds, and unload at a rate of 0.5 mm per second. Forty compression trials were planned to be performed in total, with two trials for each of twenty samples (ten concentrations, two gels for each concentration). However, for several samples additional compressions were performed, and for three compressions the data were not analyzed due to slippage of the sample or not having the force transducer zeroed properly. In total, 45 compression tests were analyzed. The samples were tested in random order. Sandpaper was attached to the upper and lower platens with cyanoacrylate ("superglue") to reduce slippage of the samples during compression.

1. The first part of the document is a list of names and addresses of the members of the committee. The names are listed in alphabetical order, and the addresses are listed below each name. The list includes names such as Mr. J. B. Smith, Mr. J. C. Jones, and Mr. J. D. Brown.

2. The second part of the document is a list of names and addresses of the members of the committee. The names are listed in alphabetical order, and the addresses are listed below each name. The list includes names such as Mr. J. E. White, Mr. J. F. Black, and Mr. J. G. Green.

The shear modulus of the agar gels was determined as described in the equations in section 4.1.1.3. A strain range was determined for analyzing the force-displacement curve. The starting point for the strain range, or initial length of the sample, was determined at the point an initial force ( $F_0$ ) was crossed, and the final length (or height) was the ultimate displacement or a maximum strain displacement ( $\Delta\varepsilon$ ), whichever condition was satisfied first. These parameters are shown on a representative data set in Figure 4-12. The initial force,  $F_0$ , was set to be 0.1 N, and the maximum allowable strain displacement  $\Delta\varepsilon$  was set to be either 10% strain or the maximum displacement achieved. The actual strain range for the analysis varied between 7.3% and 10% for all of the samples measured.

**Figure 4-12. Representative force-displacement data for agar mechanical testing.**



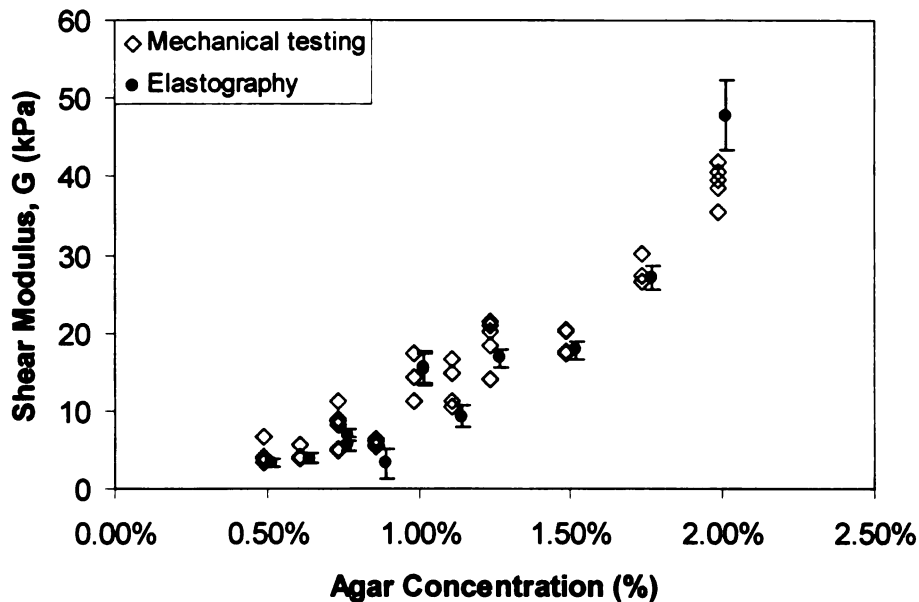
#### **4.1.2.3 Comparison of Elastography and Mechanical Testing**

The shear modulus estimates for agar gel were compared between the mechanical testing and elastographic methods. Figure 4-13 displays all of the individual mechanical test results and the mean and standard deviation of the shear modulus estimates in the ROI for the elastography results. Across the range of agar gel concentrations tested, there is generally very good agreement between the two

methods. The highest concentration of 2.0% is the only one where the mean and 1 SD error bar of the elastography method does not overlap with the mechanical test results.

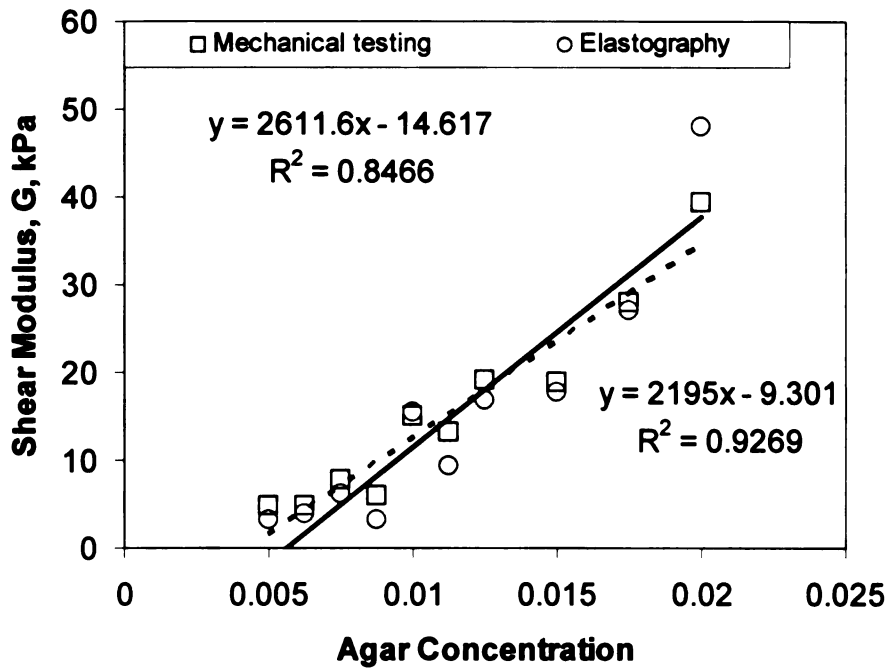
The average values for shear modulus were found for the mechanical test results, as well as for 0.75% and 1.0% elastography results, and least squares linear regression was used to find the relationship between shear modulus and agar gel concentration for the two methods. The results are shown in Figure 4-14, and the 95% confidence intervals for the slope were determined to be 1693 to 2697 for the mechanical testing and 1705 to 3517 for elastography. For the intercept, the 95% confidence intervals were found to be -5.2 to 7.1 for mechanical testing and -10.3 to 12.0 for elastography. Hence, the linear regression terms for the two methods were not found

**Figure 4-13. Shear modulus estimates from mechanical testing and elastography.**



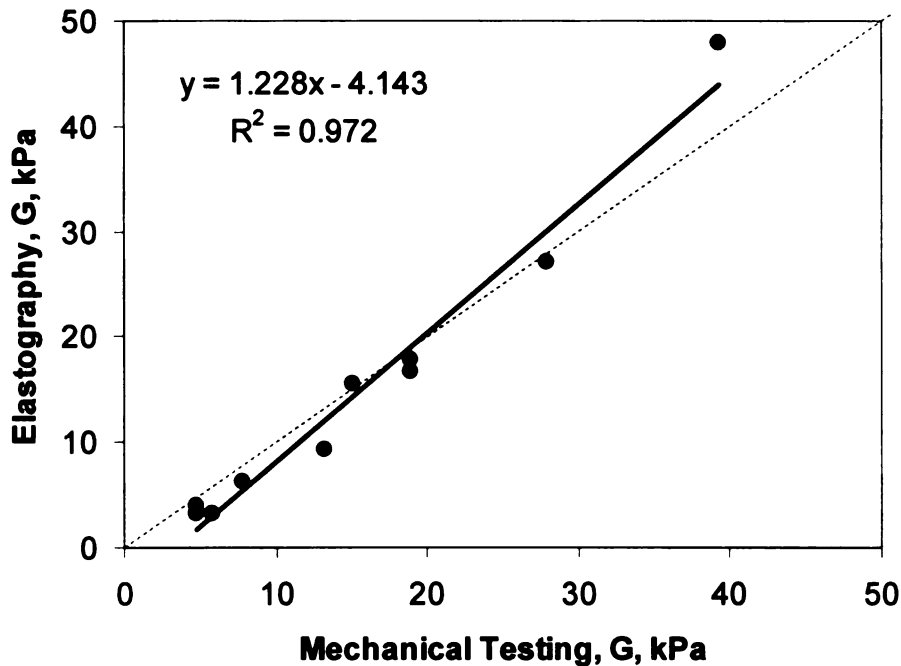
\* Error bars are 1 SD in the ROI for elastography.

**Figure 4-14. Mean shear modulus estimates from mechanical testing and elastography.**



to be significantly different ( $P > 0.05$ ). The correlation of the mean shear modulus estimates for agar gel for the two methods is shown in Figure 4-15. All of the values fall very close to the  $y=x$  line except for the measurement at 2.0%, where the elastography method overestimates the shear modulus compared to the mechanical testing method. This value greatly influences the linear regression between the two methods, which is found to have 95% confidence intervals for the slope and intercept to be 1.06 to 1.40 and -7.34 to -0.95 for the slope and intercept, respectively. Therefore, the elastography method is found to overestimate the shear modulus of the agar gel compared to mechanical testing.

**Figure 4-15. Correlation of shear modulus estimates from mechanical testing and elastography.**



With the elastography and mechanical testing methods agreeing well on the shear modulus of the agar gels, the elastographic method is confirmed in its ability to assess changes in shear modulus. To apply the method to an interesting biological tissue, bovine intervertebral disc tissue is evaluated in series of experiments.

Preliminary experiments were performed on cervical bovine discs, which developed the technique for embedding the tissue in agar and performing both elastography and MR relaxation measurements on the tissue. These qualitative experiments showed the effect of swelling on the tissue, and further experiments, a “pilot study”, were designed to attempt control the swelling of the tissue. Finally, a comprehensive study combines the optimal elastography method with a sample preparation method that controls the hydration of the tissue, enabling evaluation of the effect of tissue degeneration with Papain on the shear modulus and MR relaxation values of the tissue.



1. The first part of the document discusses the importance of maintaining accurate records of all transactions. It emphasizes that proper record-keeping is essential for the integrity of the financial system and for the ability to detect and prevent fraud.

2. The second part of the document outlines the specific procedures for recording transactions. It details the steps involved in the accounting process, from the initial recording of a transaction to the final preparation of financial statements.

## **4.2 Ex vivo Bovine Cervical Intervertebral Disc**

An intervertebral disc (IVD) specimen was dissected from the cervical section of a freshly butchered calf that was acquired at a local meat market. The IVD was embedded into a homogeneous 1.0% agarose gel with phosphate-buffered saline (PBS). The IVD was arranged so that an axial view of the object revealed the axial cross-section of the IVD, with the anterior-posterior portions of the disc aligned in the right-left direction, as shown in the magnitude images in Figure 4-17.

### **4.2.1 T1 and T2 maps of bovine cervical intervertebral disc**

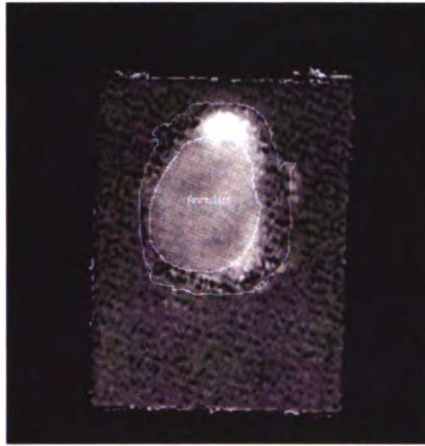
Quantitative T1 and T2 maps of the intervertebral discs were generated from multi-echo spin echo sequences. For the T2 maps, a repetition time of 1 sec was used with four echoes at 20/40/60/80 ms. For the T1 maps, repetition times of 250/500/750/1000 ms were acquired with four echoes at 20/40/60/80 ms, however only the first echo at 20 ms was used for fitting the T1 values. The same slices volume was acquired as for the elastography experiments.

The region of interests (ROIs) were generated with the TE/TR = 20/1000 ms magnitude image by setting a contour threshold of 2000. This allowed good delineation of the annulus and nucleus pulposus regions of the disc. The ROIs were overlaid on the T1 and T2 maps, shown in Figure 4-16.

**Figure 4-16. T1 and T2 maps for bovine IVD.**

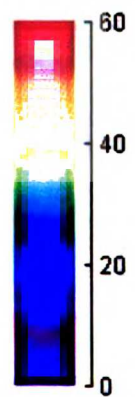
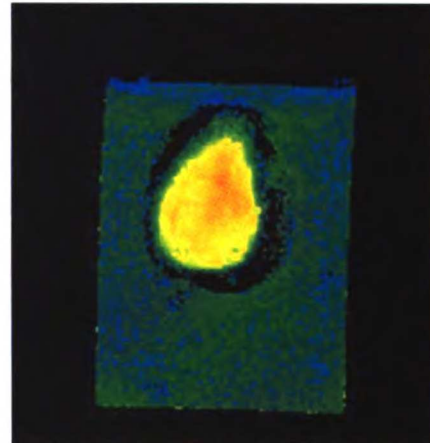
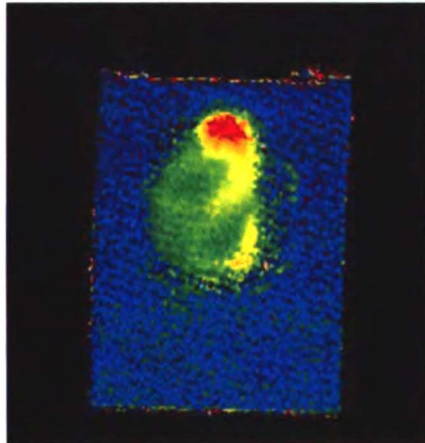
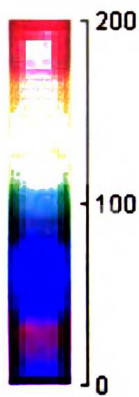
A – T1 map with ROIs

C – T2 map with ROIs



B – Color T1 map

D – Color T2 map



\* Annulus ROI is between the contours, the nucleus ROI is inside inner contour.

**Table 4-2. T1 and T2 for bovine IVD.**

| Mean $\pm$ 1 SD | Nucleus Pulposus | Annulus Fibrosus |
|-----------------|------------------|------------------|
| T1, ms          | 110.1 $\pm$ 15.2 | 83.4 $\pm$ 44.5  |
| T2, ms          | 39.7 $\pm$ 5.0   | 22.7 $\pm$ 4.1   |

#### 4.2.2 Elastography of bovine cervical intervertebral disc

Three elastography experiments were performed, using the spin-echo elastography method at 500 and 625 Hz. The 500 Hz condition was repeated with NEX = 1 and 2, while the 625 Hz experiment was done with NEX = 2. Sixteen offsets were acquired, at each eighth of the shear wave period with the motion phase starting at 0

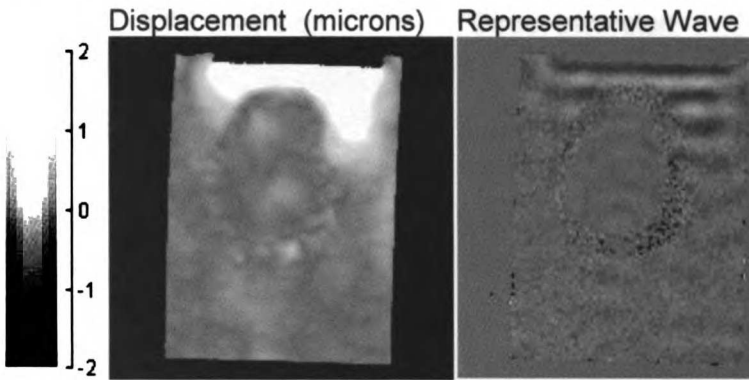
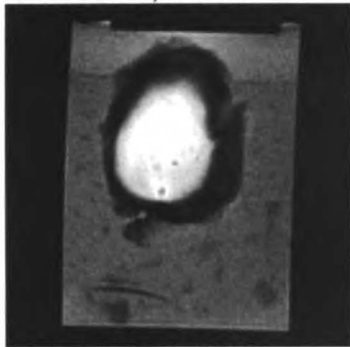
and 180 degrees. The voltage output of the wave generator was set to 7 V, the maximum amplitude of the MEGs was 3.5 G/cm, with ten MEGs before and after the 180 degree refocusing pulse on the slice selection axis. The TE/TR was set to 20/175 ms, the bandwidth was 15.6 kHz, and the field of view was 12 cm with a slice thickness of 5 cm. The acquired matrix was 256x160 and the frequency direction was right-to-left for the axial plane acquisition.

Adequate shear wave penetration is visible for all of the conditions tested (Figure 4-17). However, at 625 Hz, there was a marked reduction in phase encoding of the shear motion. In addition, the extremely small signal from the annulus fibrosus made phase measurements in this tissue impossible.

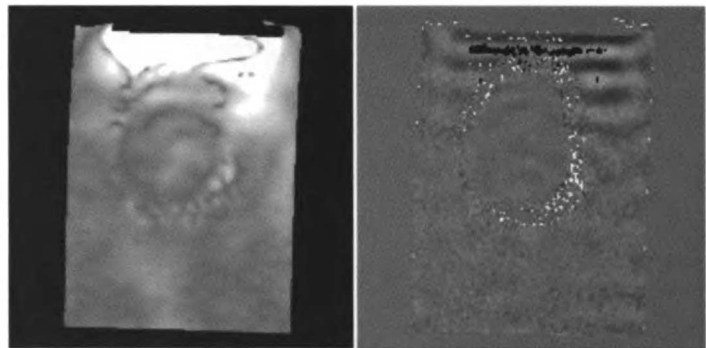
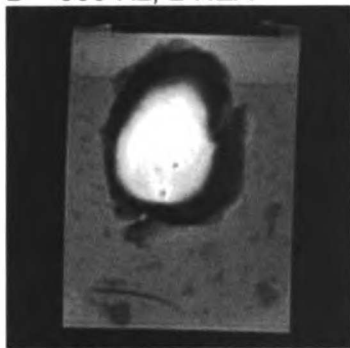
The phase images were inverted to shear modulus estimates by both the local frequency estimation (LFE) and direct inversion (DI) methods, shown in Figure 4-18. The results are noticeably varied, with the NEX = 1 and NEX = 2 conditions at 500 Hz to have substantial differences in shear estimates in the NP. The background has a mottled appearance, most likely due to low phase amplitude and complex wave motions in the material.

**Figure 4-17. Magnitude, displacement amplitude, and representative wave image for bovine cervical IVD.**

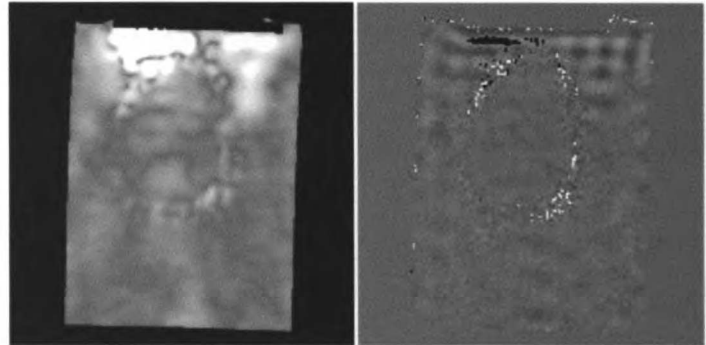
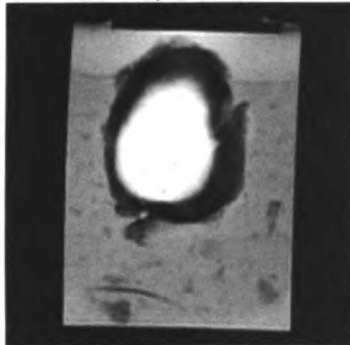
A – 500 Hz, 1 NEX



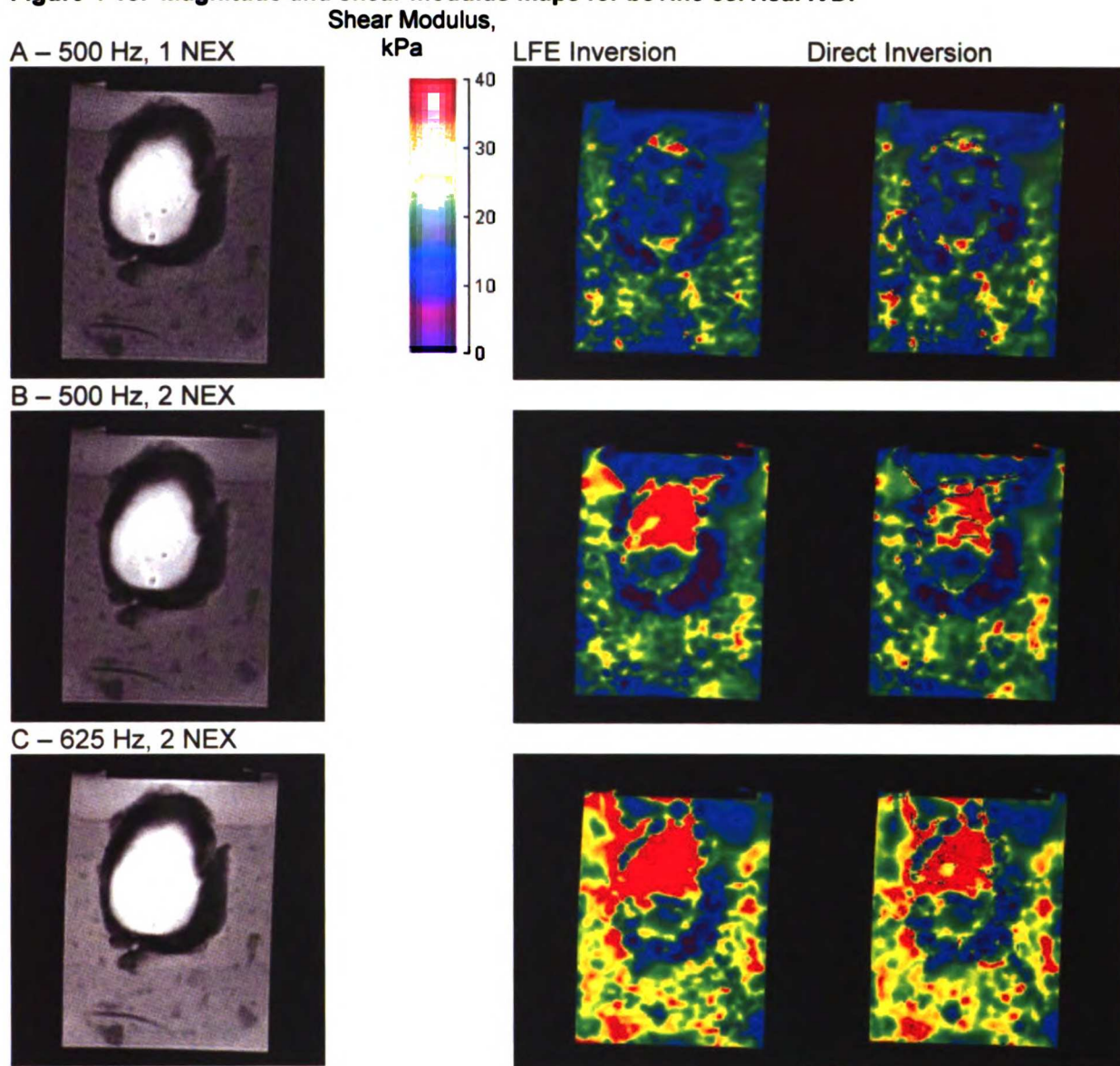
B – 500 Hz, 2 NEX



C – 625 Hz, 2 NEX



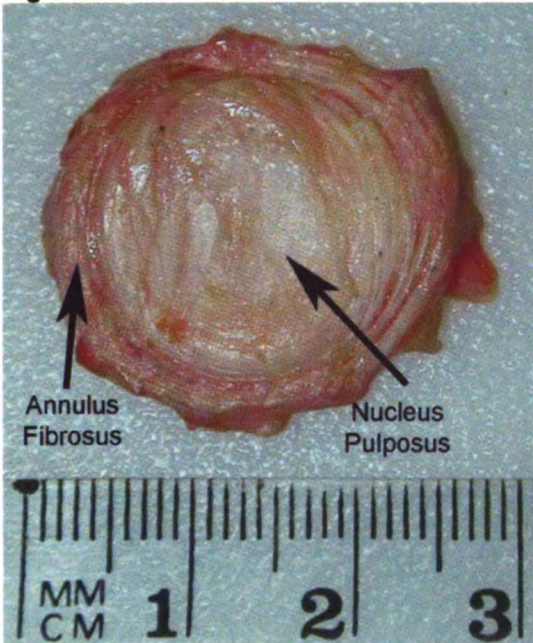
**Figure 4-18. Magnitude and shear modulus maps for bovine cervical IVD.**



### **4.3 Pilot Study of Ex Vivo Bovine Caudal Intervertebral Disc Elastography**

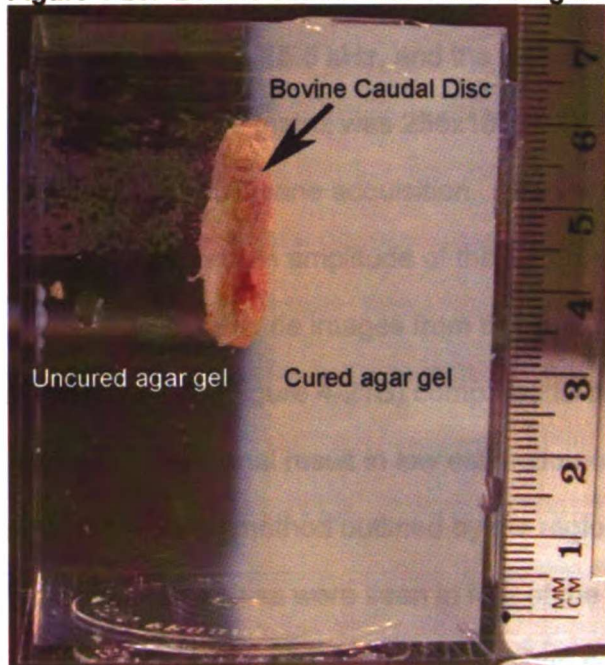
Five fresh frozen bovine caudal intervertebral disc specimens were harvested from cow tails acquired at a local butcher (Smith's Meats, San Francisco, CA). The distinct regions of the disc were clearly visible, with the thick collagen bundles of the annulus fibrosus encircling the softer, more homogeneous nucleus pulposus (Figure 4-19). After dissection, the discs were immediately double wrapped in plastic wrap, put in a sealed plastic bag, and frozen at  $-80^{\circ}\text{C}$ .

**Figure 4-19. Bovine caudal intervertebral disc**



For a pilot study of the efficacy of the elastography method to measure the shear modulus of the discs, five disc samples were thawed and embedded in 1% agarose gel with 0.5 mM GAD (Figure 4-20). Three of the discs were embedded in agar gel made with purified water, and two were embedded in gel made with phosphate-buffered saline ( $Mg^{++}$ ,  $Ca^{++}$  free). The different preparations were both observed to cause significant swelling of the nucleus pulposus when placed into the uncured agar solution. However, it was expected that the PBS solution would cause less swelling and more consistent elastography measurements. The purpose of the pilot study was to assess the feasibility of measuring shear modulus estimates in the nucleus pulposus, examine differences between the embedding material and differences between the spin echo-based and gradient echo-based elastography methods.

**Figure 4-20. Bovine caudal disc embedding in agar gel**



#### **4.3.1 Comparison of elastography acquisition method**

The gradient echo-based (GE) and spin echo-based (SE) elastography methods were compared for the bovine caudal intervertebral disc. Despite previous analysis of the differences these methods in agar, the comparison was made in this biological tissue due to expected influences of the shortened T2 of the disc material as seen in the cervical disc tissue. With the shorter echo time of the GE method, it has the potential to have improved SNR. However, it is also more susceptible to inhomogeneities in the sample, so these effects may reduce its efficacy compared to the SE method.

The elastography experiments were successful in resolving shear waves in the nucleus pulposus of the samples. The two experiments were performed at 500 Hz, one using the SE elastography method with 10 motion encoding gradients, and one using the GE elastography method with 5 motion encoding gradients. For the SE method, sixteen offsets were acquired, at each eighth of the shear wave period with the motion phase starting at 0 and 180 degrees. The TE/TR was set to 20/175 ms. For the GE method, eight offsets were acquired, at each eighth of the shear wave period with the motion

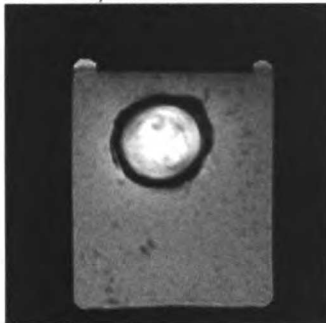


phase starting at 0 degrees. The TE/TR was set to 10/175 ms. For both experiments, the bandwidth was 15.6 kHz, and the field of view was 12 cm with a slice thickness of 5 cm. The acquired matrix was 256x160, NEX = 1, and the frequency direction was right-to-left for the axial plane acquisition. The voltage output of the wave generator was set to 7 V, the maximum amplitude of the MEGs was 3.5 G/cm.

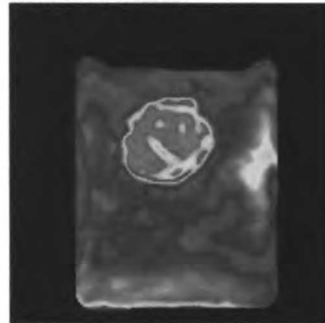
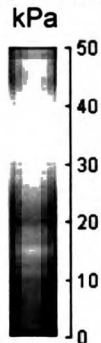
The magnitude images from the experiments showed regions of signal loss for the GE method (Figure 4-21B) compared to the SE method (Figure 4-21A). These regions of low signal result in low estimation of the shear stiffness by the local frequency estimation (LFE) method outlined by the region of interest in the GE images. Similar regions of signal loss were seen in four of the five discs, and indicate that the potential benefit of the shorter TE for the GE method does not improve the elastographic technique.

**Figure 4-21. Elastography of bovine caudal intervertebral disc.**

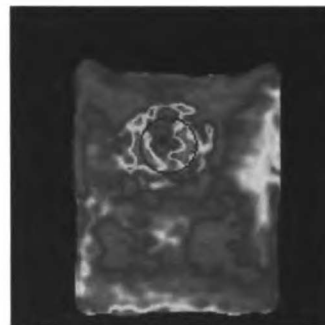
A – SE, MEGs = 10



Shear Modulus, LFE Inversion



B – GE, MEGs = 5



1. The first part of the document discusses the importance of maintaining accurate records of all transactions and activities. It emphasizes that this is crucial for ensuring transparency and accountability in the organization's operations.

2. The second part of the document outlines the various methods and tools used to collect and analyze data. It highlights the need for a systematic approach to data collection and the importance of using reliable sources of information.

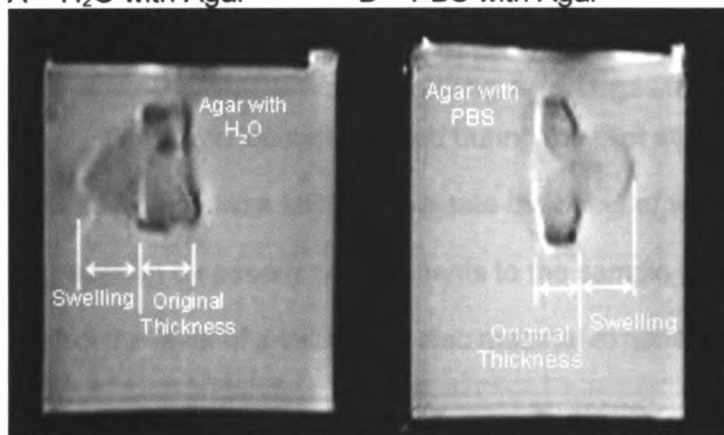
### 4.3.2 Comparison of embedding material: Purified Water and PBS

The intervertebral disc samples were able to swell to a very significant degree when placed into the uncured agar gel. Whether mixed with H<sub>2</sub>O or PBS, the nucleus pulposus swelled into a bulge that was two to three times its original thickness. Figure 4-22 shows the sagittal views of discs embedded in agar gel from the localizer imaging series. As shown, in both cases there was significant swelling, and in both cases the swelling only occurred in the direction where the uncured agar gel was added. The opposite half of the agar gel had been cured in order to allow placement of the disc in the middle of the phantom. Previous work cited by Iatridis [113] found that the nucleus pulposus was capable of swelling more than 200% of its original volume, which is closely reflected here.

**Figure 4-22. Swelling of bovine nucleus pulposus.**

A – H<sub>2</sub>O with Agar

B – PBS with Agar



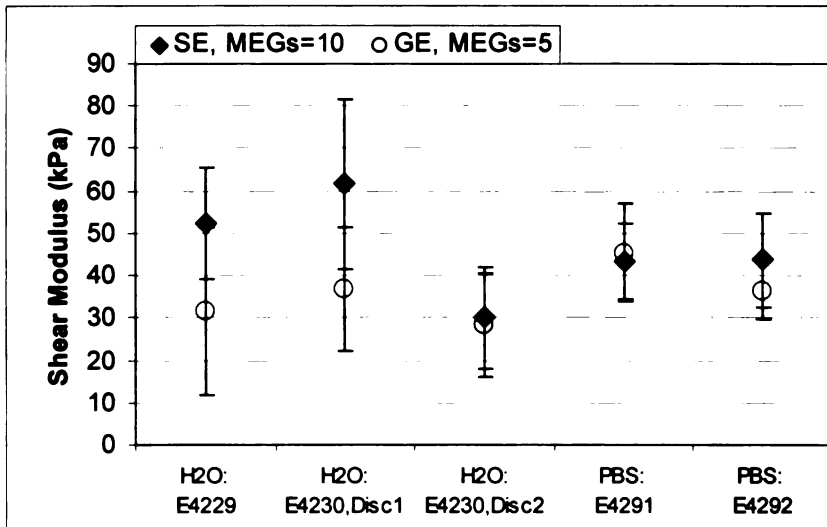
The shear modulus estimates for the samples in the water and PBS-based agar gels were found to be similar, as shown in Figure 4-23. The measurements from the GE-based method are shown as well, and can be seen to be lower than the SE method for two of the five samples. These values for the shear modulus closely track those reported by previous investigators. Bodine [114] performed dynamic mechanical testing on nucleus samples at 100 Hz and found shear modulus values of 30 to 50 kPa at

1. The first part of the document discusses the importance of maintaining accurate records of all transactions and activities. It emphasizes the need for transparency and accountability in financial reporting.

2. The second part of the document outlines the various methods and techniques used to collect and analyze data. It highlights the importance of using reliable sources and ensuring the accuracy of the information gathered.

physiologic hydration. With dehydration, however, the shear modulus was found to increase to 100 – 500 kPa.

**Figure 4-23. Shear modulus estimates in bovine caudal intervertebral disc.**



#### 4.4 Comprehensive Study of Ex Vivo Bovine Caudal Intervertebral Disc Elastography with Swelling and Digestion

Given the lessons learned during the pilot study, a comprehensive study was undertaken to utilize MRE to evaluate the effect of water imbibition and enzymatic degradation by papain. Adjustments to the sample preparation were necessary to control the level of swelling the disc material experiences.

##### 4.4.1 Sample preparation: swelling and latex coating

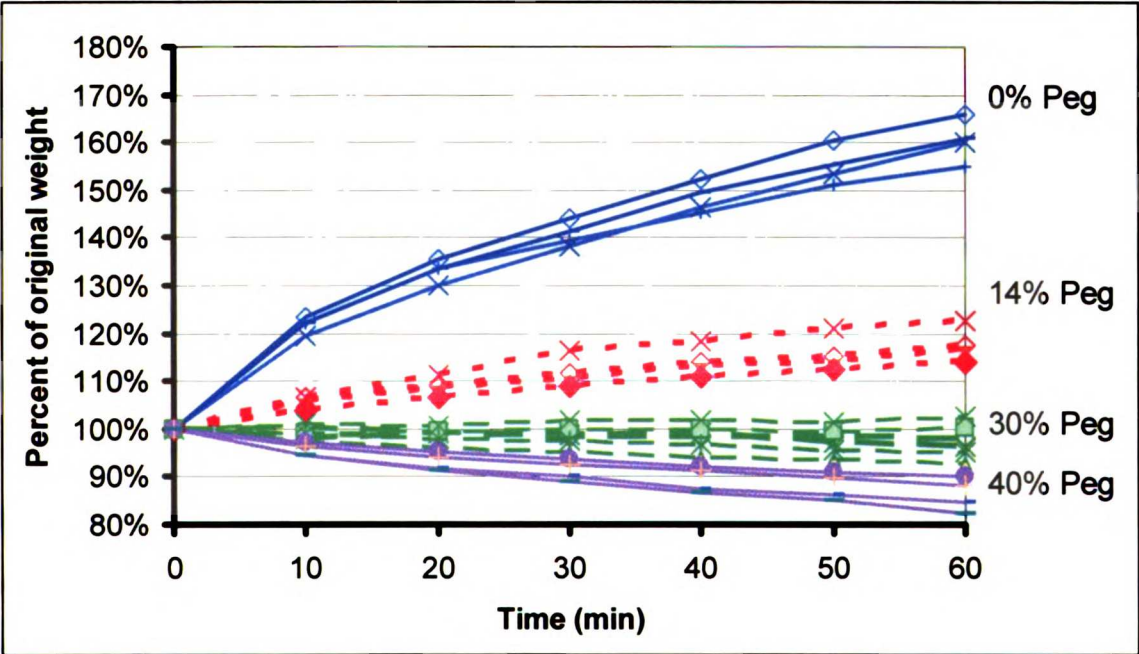
Eighteen fresh frozen bovine caudal intervertebral disc specimens were harvested as for the pilot study. The distinct regions of the disc were clearly visible, and the annulus material was trimmed away from the sample, leaving only the nucleus pulposus (NP). To control the amount of water in the NP tissue, polyethylene glycol (PEG) (Fisher Scientific, Catalog Number BP233-1, molecular weight of 8000) was added to PBS solution, similar to Urban [115]. The tissue was equilibrated in the solutions of varying PEG concentrations for one hour, since Urban noted that at high

1. The first part of the document discusses the importance of maintaining accurate records of all transactions and activities. It emphasizes the need for transparency and accountability in financial reporting.

2. The second part of the document outlines the various methods and techniques used to collect and analyze data. It highlights the importance of using reliable sources and ensuring the accuracy of the information gathered.

PEG concentrations, PEG molecules begin to penetrate the tissue and alter the swelling dynamics. The tissue was weighed every 10 minutes during the treatment, making sure to pat-dry the tissue with Kimwipes before weighing. The results of the swelling effect for four PEG concentrations (0%, 14%, 30%, 40%) is shown in Figure 4-24 over time, with the final swelling amount shown in Figure 4-25. Four samples were prepared in the 0%, 14% and 40% PEG solutions, and six specimens were prepared in the 30% PEG solution.

**Figure 4-24. Swelling of NP tissue over time with varying PEG concentration**



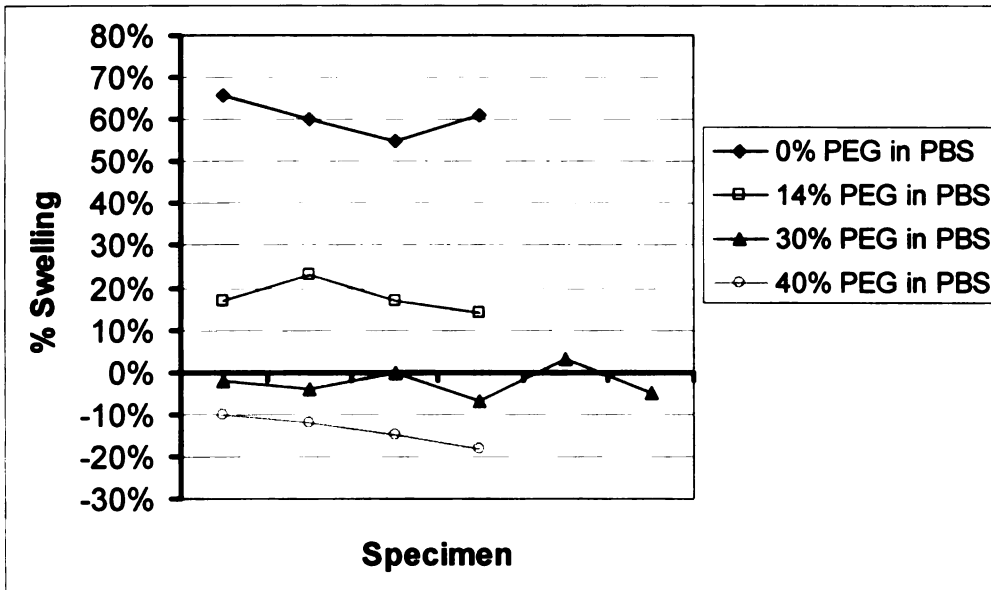
1. The first part of the document is a list of names and addresses of the members of the committee. The names are listed in alphabetical order, and the addresses are listed below each name. The list includes names such as Mr. J. H. Smith, Mr. W. D. Jones, and Mr. R. L. Brown.

2. The second part of the document is a list of the names and addresses of the members of the committee who were present at the meeting. This list is also in alphabetical order and includes names such as Mr. J. H. Smith, Mr. W. D. Jones, and Mr. R. L. Brown.

3. The third part of the document is a list of the names and addresses of the members of the committee who were absent from the meeting. This list is also in alphabetical order and includes names such as Mr. J. H. Smith, Mr. W. D. Jones, and Mr. R. L. Brown.



**Figure 4-25. Final swelling amount for intervertebral disc samples.**



These swelling results vary from Urban, where 14% of 20 kDa PEG would cause no net change in disc tissue weight, and 30% kDa PEG would cause shrinking (or net water loss) of the disc. With the 8 kDa PEG, the 30% PEG causes approximately no net water loss.

In order to seal the disc tissue from further water loss or gain, the tissue was coated with liquid latex (Mold Builder, TAP Plastics, Dublin, CA). The tissue was held with forceps and dipped repeatedly into the liquid latex and dried while being waved in front of a hot air gun. After approximately 10 coats, the forceps were released and the coating material was held instead of the tissue. The hole left by the forceps was sealed by pressing the material together, and by further coats, for a total of about 15 or 20 coats. Total preparation time for the coating process is about five to ten minutes per specimen. The latex was allowed to cure overnight before mounting into an agar gel phantom, in the manner used for the pilot study (see Figure 4-20).

1. The first part of the document discusses the importance of maintaining accurate records of all transactions and activities related to the business. It emphasizes the need for transparency and accountability in financial reporting.

2. The second part of the document outlines the various methods and techniques used to collect and analyze data, including surveys, interviews, and focus groups.

3. The third part of the document provides a detailed overview of the results of the research, highlighting key findings and trends. It also discusses the implications of these findings for the business and the industry as a whole.

#### **4.4.2 Papain Digestion Injection**

The enzymatic degradation of the NP tissue was achieved with papain (Sigma P-4762). Each disc was injected with 0.1 mL containing 2 mg of papain (14 U/mg) 0.1 M sodium phosphate (Aldrich 342483), 0.05 M EDTA (Sigma E6758) and 0.01 M L-cysteine hydrochloride (Sigma C1276), following the formulation used by Bradford [116]. Due to the small weights of the constituents of the formulation, the actual recipe for making the injections is described. In order to make six injections, 7.89 mg of cysteine was added to 5 mL of solution containing 0.1 M sodium phosphate and 0.05 M EDTA. A syringe was used to take 0.6 mL of this solution and add it to 12 mg of papain that had been measured into a 1.5 mL eppendorf tube. Each of the six injections was then taken from the eppendorf tube. This process was repeated three times for a total of 18 injections.

#### **4.4.3 Elastography, T1 and T2 mapping**

The spin-echo based elastography sequence was used for the comprehensive study, as the pilot study showed the advantage of this sequence over the gradient echo-based sequence. The piezoelectric transducer output 18 cycles of motion for each TR, with an applied voltage of 7V from the waveform generator (140 V from the amplifier). The excitation and motion encoding gradient (MEG) frequency was set to 500 Hz, with five MEGs. The amplitude of the MEGs was set to 3.5 G/cm. Sixteen offsets between the applied motion and the MEGs were acquired, at 0, 0.25, 0.5, 0.75, 1, 1.25, 1.5 and 1.75 ms with starting phase of 0 and 180 degrees. The TE/TR was set to 20/500 ms, with a bandwidth of 15.6 kHz, 12 cm field of view, and 5 mm slice thickness. The acquisition matrix was 256x160, with 1 NEX, right-to-left frequency direction for the axial slice acquisition. In addition, the CV for the "reconstruction header control", or "rhrcctrl", was set to a value of 31 so that the magnitude, phase, real and imaginary images were all reconstructed by the scanner.

1. The first part of the document is a list of names and addresses of the members of the committee. The names are listed in alphabetical order, and the addresses are given in full. The list includes the names of the members of the committee, the names of the members of the sub-committee, and the names of the members of the advisory committee. The addresses are given in full, including the street, city, and state.

2. The second part of the document is a list of the names and addresses of the members of the committee. The names are listed in alphabetical order, and the addresses are given in full. The list includes the names of the members of the committee, the names of the members of the sub-committee, and the names of the members of the advisory committee. The addresses are given in full, including the street, city, and state.

3. The third part of the document is a list of the names and addresses of the members of the committee. The names are listed in alphabetical order, and the addresses are given in full. The list includes the names of the members of the committee, the names of the members of the sub-committee, and the names of the members of the advisory committee. The addresses are given in full, including the street, city, and state.

A four-echo spin echo sequence was used to acquire images to be processed as T1 and T2 maps. The slice position was set to be the same as for the elastography scan using the “Copy Rx” feature of the graphical prescription tool. The scan was executed with the echoes at 15, 30, 45, and 60 ms with repetition times of 2500, 1000, 500 and 250 ms. The “optr” CV was modified so that the four scans were all saved into the same series. The “mrsc\_image” software tool package was used to generate the T1 and T2 maps. For the T2 map, the TR = 2500 ms was used with a magnitude threshold of 200. For the T1 map, the TE = 15 ms was used with a magnitude threshold of 250. These maps were saved in “int2” format, and then converted into Matlab format for region of interest processing with the MREView program.

#### **4.4.4 Results**

The comprehensive study results allow analysis of the effect of both papain degradation and water imbibition on the measures of shear modulus (G), T1 relaxation and T2 relaxation. Of the two effects, the papain degradation is the most controlled, since it allows a paired analysis on the same tissue before and after treatment. From the analysis, the papain treatment is shown to significantly affect the shear modulus and T2 of the NP tissue. The effect of swelling is not controlled in the same way, however, since the extensive sample preparation – latex coating and mounting in agar gel – prevented a before-and-after study design. The results show that the underlying dispersion of the measured values overpowers any effect of the swelling treatment.

##### **4.4.4.1 Effect of injection**

A Student’s t-test was used to examine the effect of the papain injection on the mean values of shear modulus, T1 and T2. The results, shown in Table 4-3, found significant ( $p < 0.05$ ) changes in shear modulus and T2 with the application of the papain injection. The effects were opposite in magnitude, with the shear modulus decreasing

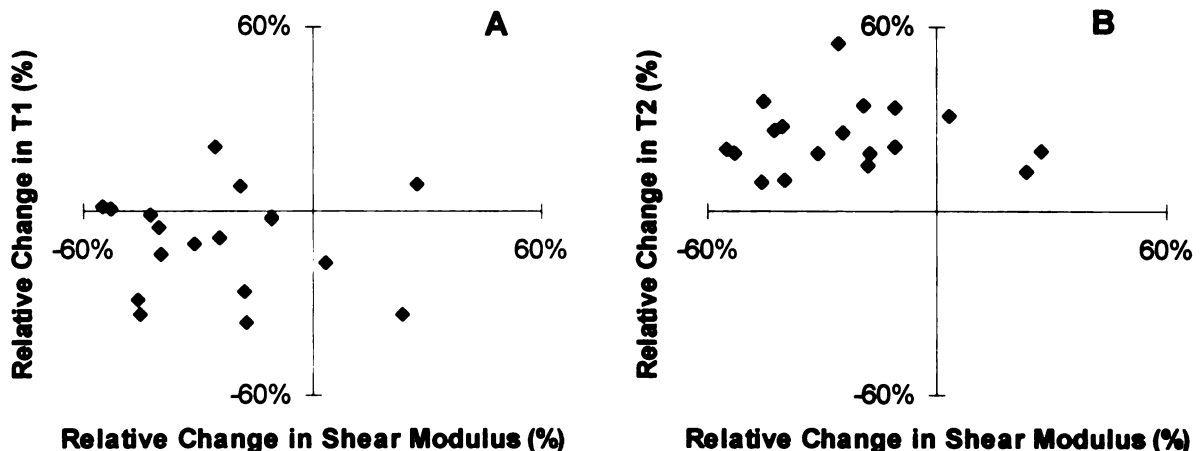
on average, whereas the T2 values were found to increase. There was no significant change in T1 with the application of the papain injection.

**Table 4-3. Effect of papain injection on shear modulus, T1 and T2.**

| Mean $\pm$ 1 SD     | Before Injection    | After Injection     | p value  |
|---------------------|---------------------|---------------------|----------|
| Shear Modulus (kPa) | 59.84 $\pm$ 12.00   | 43.87 $\pm$ 9.41    | < 0.0001 |
| T1 (ms)             | 561.08 $\pm$ 225.67 | 512.09 $\pm$ 269.85 | 0.5584   |
| T2 (ms)             | 46.38 $\pm$ 6.59    | 57.11 $\pm$ 6.70    | < 0.0001 |

Given the general effect of shear modulus decreasing and T2 increasing, the correlation of the relative change in the measures was evaluated for each specimen. Figure 4-26A and B plots the relative changes in T1 and T2 versus the relative change in shear modulus. Despite the change in the mean values, the changes in T1 or T2 and shear modulus are not correlated ( $r = 0.002$ ,  $r = 0.0004$ ).

**Figure 4-26. Relative change in T1 or T2 versus shear modulus due to papain injection.**



For three of the specimens, the shear modulus actually increases after papain treatment. Potential causes include incomplete injection of the papain or leaking of the latex coating. However, no conclusive evidence was found for these aberrations.

1. The first part of the document discusses the importance of maintaining accurate records of all transactions and activities. It emphasizes that this is crucial for ensuring transparency and accountability in the organization's operations.

2. The second part of the document outlines the various methods and tools used to collect and analyze data. It highlights the need for consistent and reliable data collection processes to support informed decision-making.

3. The third part of the document focuses on the role of technology in modern data management. It discusses how advanced software solutions can streamline data collection, storage, and analysis, leading to more efficient and effective operations.

4. The fourth part of the document addresses the challenges associated with data security and privacy. It stresses the importance of implementing robust security measures to protect sensitive information from unauthorized access and breaches.

5. The fifth part of the document concludes by summarizing the key findings and recommendations. It reiterates the importance of a data-driven approach and encourages the organization to continue investing in data management capabilities to stay competitive in the market.

6. The sixth part of the document provides a detailed overview of the data collection process, including the identification of data sources, the selection of appropriate collection methods, and the implementation of data collection protocols.

7. The seventh part of the document discusses the importance of data quality and the steps taken to ensure the accuracy and reliability of the collected data. It highlights the need for regular data audits and validation processes.

8. The eighth part of the document explores the various applications of data analysis, such as identifying trends, forecasting future performance, and optimizing operational efficiency. It provides examples of how data insights have been used to drive positive change in the organization.

9. The ninth part of the document addresses the ethical considerations surrounding data collection and analysis. It emphasizes the need for transparency, informed consent, and the protection of individual privacy rights.

10. The tenth part of the document provides a final summary and concludes the report. It expresses confidence in the organization's ability to leverage its data effectively and achieve its strategic goals.

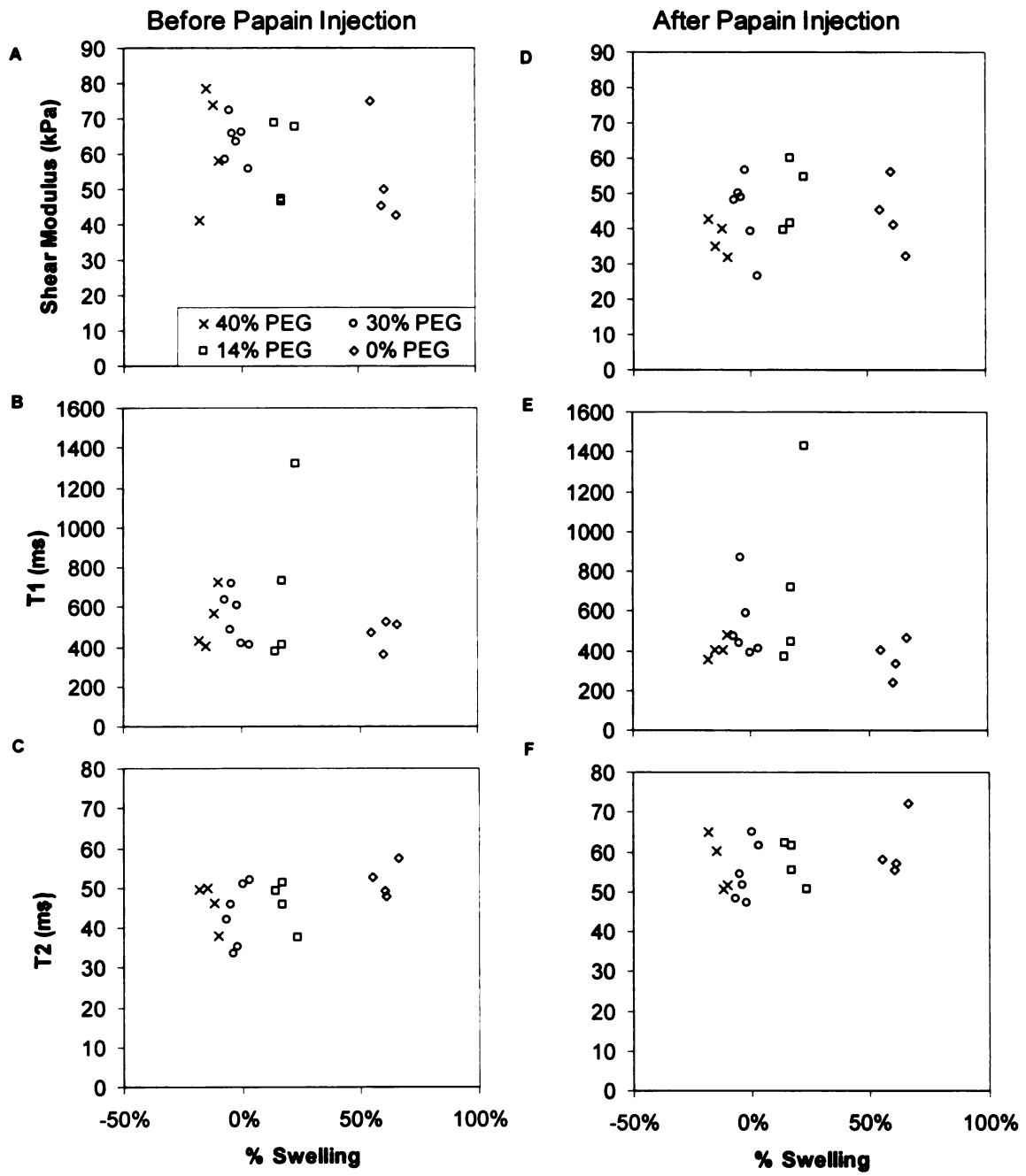
#### **4.4.4.2 Effect of swelling**

As shown in Figure 4-25, there was effective separation of the amount of swelling the specimens underwent by soaking in PBS with varying concentrations of PEG. The measures of shear modulus, T1 and T2 were examined across the treatments, however no effect was found, either before or after papain injection (Figure 4-27).

A one-way analysis of variance (ANOVA) was performed to examine the effect of the relative change in shear modulus, T1 and T2 due to the papain treatment for the different treatment groups. As shown in Figure 4-28, there is a large amount of dispersion in the results for all three measures. The only significant effect ( $p < 0.05$ ) found was for the relative change in T1. For that measure, the average relative change in T1 for the 14% PEG treatment was 3.3%, which was found to be significantly different from the 40% PEG treatment (-19.5%) and the 0% PEG treatment (-23.3%). The average relative change in T1 for the 30% PEG treatment was -3.8%, which was found to be significantly different from the 0% PEG treatment (-23.3%). These results are difficult to interpret, given that there was no underlying difference in mean T1 for these treatment groups, and that the two extreme treatments (0% and 40%) were found to be different from the two mid-range treatments (14% and 30%). Furthermore, the 14% treatment had one specimen that had an abnormally high T1 value, approximately 1300 ms, compared to a mean value of 723 ms for that group.



**Figure 4-27. Effect of swelling on shear modulus, T1 and T2.**

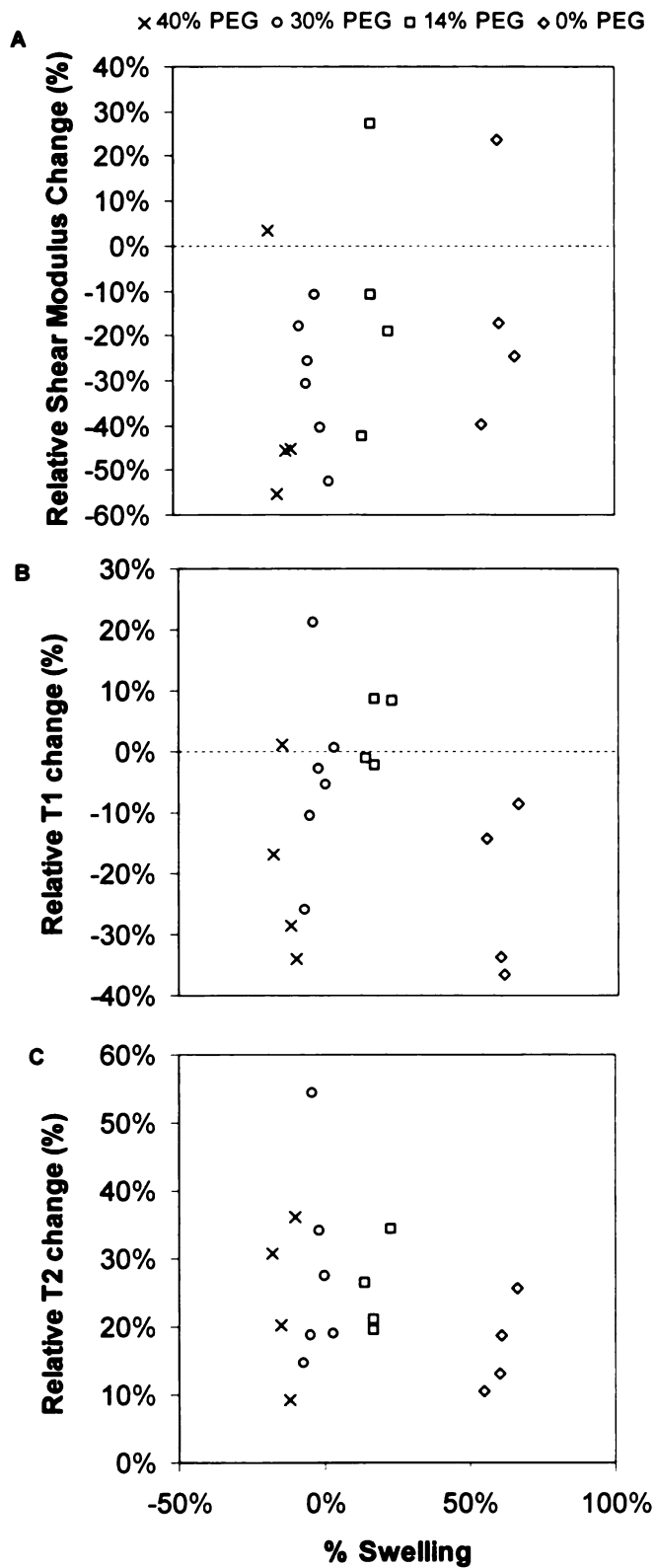


1. The first part of the document discusses the importance of maintaining accurate records of all transactions and activities. It emphasizes that proper record-keeping is essential for ensuring transparency and accountability in financial operations.

2. The second part of the document outlines the various methods and tools used to collect and analyze data. It highlights the need for robust data management systems that can handle large volumes of information efficiently.

3. The third part of the document focuses on the role of technology in modern data analysis. It discusses how advanced software solutions and artificial intelligence can significantly enhance the speed and accuracy of data processing and reporting.

**Figure 4-28. Effect of swelling on relative change in shear modulus, T1 and T2 due to papain injection.**



#### **4.4.5 Discussion**

The comprehensive study of the effect of swelling pre-treatment and papain injection on the shear modulus, T1 and T2 of bovine caudal intervertebral disc has validated the efficacy of the spin echo elastography method and its sensitivity to tissue changes. The study design of having paired measurements on the same samples before and after papain injection gave this arm of the study more power to determine changes in shear modulus and T2. The data concerning the effect of swelling pre-treatment, however, suffered from a large underlying dispersion of the measured values compared to any potential effect size. Conducting a study that has similar pairing for the swelling portion of the study presents logistical challenges, however. While the injection of the papain could be performed with the disc tissue coated in latex and embedded in agar, the swelling treatment would require repeating the coating and embedding portions of the sample preparation. While feasible, the extra preparation time and tissue handling on top of the already extensive scan time presents challenges in execution.

---

### Conclusion and Future Plans

---

The application of the elastography method for the examination of small, stiff tissues was accomplished by evaluating a range of embedded agar gel cylinders and enzymatically degrading bovine nucleus pulposus tissue with papain. The work presented here details the methods and implementation for performing MR elastography experiments, including the development and usage of spin-echo and gradient-echo techniques. These methods were developed to capture strain waves with relatively high frequencies, at least 500 Hz, to address the limitations of capturing strain waves in small, stiff tissues. The measurements determined in agar gel phantoms of varying concentration (and therefore shear stiffness) were compared between the elastography method and compressive mechanical tests, thus validating the performance of the elastography method. A sample preparation protocol was developed to allow the elastographic evaluation of ex vivo bovine nucleus pulposus tissue. The preparation included pretreatment in hyper-, hypo- and iso-osmotic PEG solutions to control the water content of the disc tissue. The tissue was then encased in latex to prevent further water exchange and embedded in agar for testing.

As a model of disc degeneration, papain was injected into the disc tissue. The changes in elastographic shear stiffness measurements were evaluated and correlations were examined with MR relaxation parameters. A significant reduction in shear stiffness was found with the enzymatic degradation of the tissue. The T2 relaxation was found to significantly increase with degradation, however there was not significant correlation between the shear stiffness and T2 changes. Additionally, the disc pretreatment in PEG solutions provided an investigation into the effect of water content on the shear stiffness of the tissue. However, these results did not show any significant

1. The first part of the document discusses the importance of maintaining accurate records of all transactions and activities. It emphasizes the need for transparency and accountability in financial reporting.

2. The second part of the document outlines the various methods and techniques used to collect and analyze data. It includes a detailed description of the experimental procedures and the statistical tools employed.

3. The third part of the document presents the results of the study, showing the trends and patterns observed in the data. It includes several tables and graphs to illustrate the findings.

4. The fourth part of the document discusses the implications of the results and provides recommendations for future research. It highlights the areas that need further investigation and the potential applications of the findings.

5. The fifth part of the document concludes the study and summarizes the key findings. It reiterates the importance of the research and the need for continued efforts in this field.

6. The sixth part of the document provides a list of references and sources used in the study. It includes books, articles, and other relevant materials that have informed the research.

7. The seventh part of the document contains the author's contact information and a statement of acknowledgment. It expresses gratitude to the individuals and organizations that have supported the research.

changes in shear stiffness with water content changes. These experiments are the first known to apply MR elastography to intervertebral disc tissue.

The MR elastography technique presents challenges on several fronts. Primary among these, the acoustic stimulation technique must be carefully matched to the application of interest. While the device presented in this work was robust across frequencies of interest and different sample sizes, it is still limited in its applications. For example, in vivo applications are problematic, primarily due to the relative fragility of the piezoelectric device in a setting that could impart “jostling” or “jolts” that could damage the device. Future enhancements to the experimental system presented here, therefore, would be to develop application-specific motion actuators. Piezoelectric devices have found success in other laboratories, but more basic coil-wrap devices would permit faster, and cheaper, device development. Further development of the current system to include different options for motion actuation would expand its potential applications.

To address the long acquisition times of the current system, there are new developments in pulse sequence design being developed. In particular, a reduced field of view method has been proposed by Glaser [117]. Alternatively, exciting progress has been made in using steady state free precession (SSFP) sequences for MR elastography [118, 119], which provide extremely fast acquisition times. For example, the SSFP-based methods claim to offer an order-of-magnitude scan-time efficiency improvement compared to traditional methods. These methods could make full three-dimensional acquisitions feasible in an in vivo setting from a scan time point of view, and could greatly improve the applicability to new tissues of interest.

Reducing the acquisition time is important for in vivo application, but for the intervertebral disc the biggest challenge lies in driving strain waves of sufficient amplitude into the disc. Not only are the discs located deep in the body, but they are well protected by the vertebral bodies and spinous processes. Strain waves generated

on the skin would likely be attenuated or reflected by the surrounding bony tissue. More elaborate methods of generating shear motion deep in the body have been proposed using focused ultrasound [120, 121]. This method may be difficult in a setting where thermal treatment is not wanted, however, as the energy needed create shear motion is very similar to that used to heat the tissue. However, methods could be adapted from intravascular elastography [71, 72, 75, 122] which involve inserting probes or catheters into the region of the spine to be evaluated. This may allow the evaluation of early degenerative changes of the intervertebral disc in a clinical setting. The information provided by these evaluations could track the progression of disease and monitor the effects of interventions.

The future of MR elastography is dependent on capitalizing on the promise of providing a valuable new contrast mechanism – shear modulus – for the evaluation of tissue health and disease. The present work describes in detail the implementation of MR elastography for the purpose of determining the shear mechanical properties of small stiff tissues. Extensive groundwork in pulse sequence development allows flexible use of both spin echo and gradient echo-based techniques. The complete MRE system, including the motion actuator, was evaluated across many dimensions of acquisition parameters, providing support for theoretical descriptions and future experimental designs. Finally, the technique was verified and validated by application to agar gel samples and enzymatically degraded intervertebral disc tissue.





1. The first part of the document  
 discusses the general principles  
 of the system and its  
 objectives. It also outlines  
 the scope of the study and  
 the methodology used.

2. The second part of the document  
 provides a detailed description  
 of the system and its components.  
 It also discusses the results of  
 the study and the conclusions  
 drawn from the analysis.

---

## References

---

- [1] "Prevention and Early Detection of Cancer," American Cancer Society 2002.
- [2] Y. Fung, *Biomechanics: mechanical properties of living tissues*. Berlin:: Springer, 1993.
- [3] J. C. Iatridis, S. Kumar, R. J. Foster, M. Weidenbaum, and V. C. Mow, "Shear mechanical properties of human lumbar annulus fibrosus," *J Orthop Res*, vol. 17, pp. 732-7., 1999.
- [4] J. C. Iatridis, L. A. Setton, M. Weidenbaum, and V. C. Mow, "Alterations in the mechanical behavior of the human lumbar nucleus pulposus with degeneration and aging," *J Orthop Res*, vol. 15, pp. 318-22., 1997.
- [5] Y. Fujita, D. R. Wagner, A. A. Biviji, N. A. Duncan, and J. C. Lotz, "Anisotropic shear behavior of the annulus fibrosus: effect of harvest site and tissue prestrain," *Med Eng Phys*, vol. 22, pp. 349-57, 2000.
- [6] P. J. McCracken, T. E. Oliphant, J. F. Greenleaf, and R. L. Ehman, "Magnetic Resonance Elastography," in *Handbook of Elastic Properties of Solids, Liquids and Gases*, vol. 1, B. a. S. Levy, Ed.: Academic Press, 2001, pp. 109-119.
- [7] T. A. Krouskop, D. R. Dougherty, and F. S. Vinson, "A pulsed Doppler ultrasonic system for making noninvasive measurements of the mechanical properties of soft tissue," *J Rehabil Res Dev*, vol. 24, pp. 1-8, 1987.
- [8] R. M. Lerner, S. R. Huang, and K. J. Parker, ""Sonoelasticity" images derived from ultrasound signals in mechanically vibrated tissues," *Ultrasound Med Biol*, vol. 16, pp. 231-9, 1990.
- [9] L. Gao, K. Parker, S. Alam, D. Rubens, and R. Lerner, "Theory and Application of Sonoelasticity Imaging," *International Journal of Imaging Systems and Technology*, vol. 8, pp. 104-109, 1997.
- [10] A. Skovoroda, S. Emelianov, and M. O'Donnell, "Tissue elasticity reconstruction based on ultrasonic displacement and strain images," *IEEE Transactions on Ultrasonics, Ferroelectrics, and Frequency Control*, vol. 42, pp. 747-765, 1995.
- [11] J. Ophir, S. K. Alam, B. Garra, F. Kallel, E. Konofagou, T. Krouskop, and T. Varghese, "Elastography: ultrasonic estimation and imaging of the elastic properties of tissues," *Proc Inst Mech Eng [H]*, vol. 213, pp. 203-33, 1999.
- [12] L. Gao, K. J. Parker, R. M. Lerner, and S. F. Levinson, "Imaging of the elastic properties of tissue—a review," *Ultrasound Med Biol*, vol. 22, pp. 959-77, 1996.
- [13] K. J. Parker, D. Fu, S. M. Graceswki, F. Yeung, and S. F. Levinson, "Vibration sonoelastography and the detectability of lesions," *Ultrasound Med Biol*, vol. 24, pp. 1437-47., 1998.
- [14] R. Souchon, L. Soualmi, M. Bertrand, J. Y. Chapelon, F. Kallel, and J. Ophir, "Ultrasonic elastography using sector scan imaging and a radial compression," *Ultrasonics*, vol. 40, pp. 867-71, 2002.
- [15] P. van Dijk, "Direct cardiac NMR imaging of heart wall and blood flow velocity," *J Comput Assist Tomogr*, vol. 8, pp. 429-36, 1984.
- [16] J. R. Singer, "Nmr Diffusion and Flow Measurements and an Introduction to Spin Phase Graphing," *Journal of Physics E-Scientific Instruments*, vol. 11, pp. 281-291, 1978.
- [17] P. R. Moran, "A flow velocity zeugmatographic interlace for NMR imaging in humans," *Magn Reson Imaging*, vol. 1, pp. 197-203, 1982.

1. The first part of the document discusses the importance of maintaining accurate records of all transactions. It emphasizes that this is crucial for ensuring the integrity of the financial statements and for providing a clear audit trail.

2. The second part of the document outlines the various methods used to collect and analyze data. It includes a detailed description of the sampling techniques employed and the statistical tests used to evaluate the results.

3. The third part of the document presents the findings of the study. It shows that there is a significant correlation between the variables being studied, and it provides a clear explanation of the reasons behind this relationship.

4. The final part of the document discusses the implications of the findings and offers suggestions for further research. It concludes that the study has provided valuable insights into the subject matter and that the results are likely to be of interest to other researchers in the field.

5. The document also includes a section on the limitations of the study. It acknowledges that there are certain constraints on the data and that the results may not be generalizable to all situations. However, it believes that the study has provided a solid foundation for further research in this area.

6. Finally, the document includes a section on the conclusions. It summarizes the main findings of the study and reiterates the importance of the research. It concludes that the study has provided a clear and concise overview of the subject matter and that the results are likely to be of interest to other researchers in the field.

- [18] W. Denk, R. M. Keolian, S. Ogawa, and L. W. Jelinski, "Oscillatory flow in the cochlea visualized by a magnetic resonance imaging technique," *Proc Natl Acad Sci U S A*, vol. 90, pp. 1595-8, 1993.
- [19] C. J. Lewa and J. D. de Certaines, "MR imaging of viscoelastic properties," *J Magn Reson Imaging*, vol. 5, pp. 242-4, 1995.
- [20] C. J. Lewa and J. D. De Certaines, "Viscoelastic property detection by elastic displacement NMR measurements," *J Magn Reson Imaging*, vol. 6, pp. 652-6, 1996.
- [21] R. Muthupillai, D. J. Lomas, P. J. Rossman, J. F. Greenleaf, A. Manduca, and R. L. Ehman, "Magnetic resonance elastography by direct visualization of propagating acoustic strain waves," *Science*, vol. 269, pp. 1854-7, 1995.
- [22] J. B. Fowlkes, S. Y. Emelianov, J. G. Pipe, A. R. Skovoroda, P. L. Carson, R. S. Adler, and A. P. Sarvazyan, "Magnetic-resonance imaging techniques for detection of elasticity variation," *Med Phys*, vol. 22, pp. 1771-8, 1995.
- [23] A. Sarvazyan, A. Skovoroda, S. Emelianov, J. Fowlkes, J. Pipe, R. Adler, R. Buxton, and P. Carson, "Biophysical bases of elasticity imaging," *Acoustical Imaging*, vol. 21, pp. 223-240, 1995.
- [24] D. B. Plewes, I. Betty, S. N. Urchuk, and I. Soutar, "Visualizing tissue compliance with MR imaging," *J Magn Reson Imaging*, vol. 5, pp. 733-8, 1995.
- [25] R. Muthupillai and R. L. Ehman, "Magnetic resonance elastography," *Nat Med*, vol. 2, pp. 601-3, 1996.
- [26] V. Dutt, R. R. Kinnick, R. Muthupillai, T. E. Oliphant, R. L. Ehman, and J. F. Greenleaf, "Acoustic shear-wave imaging using echo ultrasound compared to magnetic resonance elastography," *Ultrasound Med Biol*, vol. 26, pp. 397-403, 2000.
- [27] A. Manduca, D. S. Lake, S. A. Kruse, and R. L. Ehman, "Spatio-temporal directional filtering for improved inversion of MR elastography images," *Med Image Anal*, vol. 7, pp. 465-73, 2003.
- [28] A. Manduca, R. Muthupillai, P. J. Rossman, G. J. F, and R. L. Ehman, "Image Processing for Magnetic Resonance Elastography," *SPIE*, vol. 2710, pp. 616-623, 1996.
- [29] A. Manduca, T. E. Oliphant, M. A. Dresner, J. L. Mahowald, S. A. Kruse, E. Amromin, J. P. Felmlee, J. F. Greenleaf, and R. L. Ehman, "Magnetic resonance elastography: non-invasive mapping of tissue elasticity," *Med Image Anal*, vol. 5, pp. 237-54, 2001.
- [30] J. Braun, G. Buntkowsky, J. Bernarding, T. Tolxdorff, and I. Sack, "Simulation and analysis of magnetic resonance elastography wave images using coupled harmonic oscillators and Gaussian local frequency estimation," *Magn Reson Imaging*, vol. 19, pp. 703-13, 2001.
- [31] T. E. Oliphant, A. Manduca, R. L. Ehman, and J. F. Greenleaf, "Complex-valued stiffness reconstruction for magnetic resonance elastography by algebraic inversion of the differential equation," *Magn Reson Med*, vol. 45, pp. 299-310, 2001.
- [32] T. E. Oliphant, R. L. Ehman, and J. F. Greenleaf, "Estimation of complex-valued stiffness using acoustic waves measured with magnetic resonance," in *Topics in Applied Physics: Imaging of complex media with acoustic and seismic waves*. Berlin: Springer-Verlag, 2002, pp. 277-294.
- [33] T. Oliphant, "The maximum likelihood estimator of stiffness for MR elastography and its approximation as an adaptive filter," presented at ISMRM, Toronto, 2003.
- [34] E. E. Van Houten, M. M. Doyley, F. E. Kennedy, K. D. Paulsen, and J. B. Weaver, "A three-parameter mechanical property reconstruction method for MR-

- based elastic property imaging," *IEEE Trans Med Imaging*, vol. 24, pp. 311-24, 2005.
- [35] E. E. Van Houten, M. I. Miga, J. B. Weaver, F. E. Kennedy, and K. D. Paulsen, "Three-dimensional subzone-based reconstruction algorithm for MR elastography," *Magn Reson Med*, vol. 45, pp. 827-37, 2001.
- [36] E. E. Van Houten, K. D. Paulsen, M. I. Miga, F. E. Kennedy, and J. B. Weaver, "An overlapping subzone technique for MR-based elastic property reconstruction," *Magn Reson Med*, vol. 42, pp. 779-86, 1999.
- [37] J. Bishop, A. Samani, J. Sciarretta, C. Luginbuhl, and D. B. Plewes, "A signal/noise analysis of quasi-static MR elastography," *IEEE Trans Med Imaging*, vol. 20, pp. 1183-7, 2001.
- [38] J. Bishop, A. Samani, J. Sciarretta, and D. B. Plewes, "Two-dimensional MR elastography with linear inversion reconstruction: methodology and noise analysis," *Phys Med Biol*, vol. 45, pp. 2081-91, 2000.
- [39] B. J and P. DB, "An alternate method for calculating elastic properties of breast tissue," presented at ISMRM, Sydney, 1998.
- [40] Bishop J, S. A, and P. DB, "Pressure/modulus inversion for MR elastography," presented at ISMRM, Philadelphia, 1999.
- [41] "Leading Sites of New Cancer Cases and Deaths - 2005 Estimates," American Cancer Society 2005.
- [42] E. E. Van Houten, M. M. Doyley, F. E. Kennedy, J. B. Weaver, and K. D. Paulsen, "Initial in vivo experience with steady-state subzone-based MR elastography of the human breast," *J Magn Reson Imaging*, vol. 17, pp. 72-85, 2003.
- [43] H. T. Liu, L. Z. Sun, G. Wang, and M. W. Vannier, "Analytic modeling of breast elastography," *Med Phys*, vol. 30, pp. 2340-9, 2003.
- [44] J. Lorenzen, R. Sinkus, M. Biesterfeldt, and G. Adam, "Menstrual-cycle dependence of breast parenchyma elasticity: estimation with magnetic resonance elastography of breast tissue during the menstrual cycle," *Invest Radiol*, vol. 38, pp. 236-40, 2003.
- [45] A. L. McKnight, J. L. Kugel, P. J. Rossman, A. Manduca, L. C. Hartmann, and R. L. Ehman, "MR elastography of breast cancer: preliminary results," *AJR Am J Roentgenol*, vol. 178, pp. 1411-7, 2002.
- [46] D. B. Plewes, J. Bishop, A. Samani, and J. Sciarretta, "Visualization and quantification of breast cancer biomechanical properties with magnetic resonance elastography," *Phys Med Biol*, vol. 45, pp. 1591-610, 2000.
- [47] R. Sinkus, J. Lorenzen, D. Schrader, M. Lorenzen, M. Dargatz, and D. Holz, "High-resolution tensor MR elastography for breast tumour detection," *Phys Med Biol*, vol. 45, pp. 1649-64, 2000.
- [48] T. A. Krouskop, T. M. Wheeler, F. Kallel, B. S. Garra, and T. Hall, "Elastic moduli of breast and prostate tissues under compression," *Ultrason Imaging*, vol. 20, pp. 260-74, 1998.
- [49] I. Cespedes, J. Ophir, H. Ponnekanti, and N. Maklad, "Elastography: elasticity imaging using ultrasound with application to muscle and breast in vivo," *Ultrason Imaging*, vol. 15, pp. 73-88., 1993.
- [50] R. Sinkus, M. Tanter, S. Catheline, J. Lorenzen, C. Kuhl, E. Sondermann, and M. Fink, "Imaging anisotropic and viscous properties of breast tissue by magnetic resonance-elastography," *Magn Reson Med*, vol. 53, pp. 372-87, 2005.
- [51] T. Xydeas, K. Siegmann, R. Sinkus, U. Krainick-Strobel, S. Miller, and C. D. Claussen, "Magnetic resonance elastography of the breast: correlation of signal

- intensity data with viscoelastic properties," *Invest Radiol*, vol. 40, pp. 412-20, 2005.
- [52] J. F. Greenleaf, M. Fatemi, and M. Insana, "Selected Methods for Imaging Elastic Properties of Biological Tissues," *Annu Rev Biomed Eng*, vol. 10, pp. 10, 2003.
- [53] F. Kallel, R. E. Price, E. Konofagou, and J. Ophir, "Elastographic imaging of the normal canine prostate in vitro," *Ultrason Imaging*, vol. 21, pp. 201-15, 1999.
- [54] K. Konig, U. Scheipers, A. Pesavento, A. Lorenz, H. Ermert, and T. Senge, "Initial experiences with real-time elastography guided biopsies of the prostate," *J Urol*, vol. 174, pp. 115-7, 2005.
- [55] R. Souchon, O. Rouviere, A. Gelet, V. Detti, S. Srinivasan, J. Ophir, and J. Y. Chapelon, "Visualisation of HIFU lesions using elastography of the human prostate in vivo: preliminary results," *Ultrasound Med Biol*, vol. 29, pp. 1007-15, 2003.
- [56] R. J. Stafford, R. E. Price, C. J. Diederich, M. Kangasniemi, L. E. Olsson, and J. D. Hazle, "Interleaved echo-planar imaging for fast multiplanar magnetic resonance temperature imaging of ultrasound thermal ablation therapy," *J Magn Reson Imaging*, vol. 20, pp. 706-14, 2004.
- [57] J. D. Hazle, C. J. Diederich, M. Kangasniemi, R. E. Price, L. E. Olsson, and R. J. Stafford, "MRI-guided thermal therapy of transplanted tumors in the canine prostate using a directional transurethral ultrasound applicator," *J Magn Reson Imaging*, vol. 15, pp. 409-17, 2002.
- [58] R. J. Stafford, F. Kallel, R. E. Price, D. M. Cromeens, T. A. Krouskop, J. D. Hazle, and J. Ophir, "Elastographic imaging of thermal lesions in soft tissue: a preliminary study in vitro," *Ultrasound Med Biol*, vol. 24, pp. 1449-58, 1998.
- [59] S. A. Kruse, J. A. Smith, A. J. Lawrence, M. A. Dresner, A. Manduca, J. F. Greenleaf, and R. L. Ehman, "Tissue characterization using magnetic resonance elastography: preliminary results," *Phys Med Biol*, vol. 45, pp. 1579-90, 2000.
- [60] S. F. Levinson, M. Shinagawa, and T. Sato, "Sonoelastic determination of human skeletal muscle elasticity," *J Biomech*, vol. 28, pp. 1145-54., 1995.
- [61] I. Sack, J. Bernarding, and J. Braun, "Analysis of wave patterns in MR elastography of skeletal muscle using coupled harmonic oscillator simulations," *Magn Reson Imaging*, vol. 20, pp. 95-104, 2002.
- [62] K. Uffmann, S. Maderwald, W. Ajaj, C. G. Galban, S. Mateiescu, H. H. Quick, and M. E. Ladd, "In vivo elasticity measurements of extremity skeletal muscle with MR elastography," *NMR Biomed*, vol. 17, pp. 181-90, 2004.
- [63] M. S. Uffmann K, Quick H, Ladd ME, "In vivo determination of biceps elasticity with MR elastography," presented at ISMRM, Honolulu, 2002.
- [64] S. Papazoglou, J. Braun, U. Hamhaber, and I. Sack, "Two-dimensional waveform analysis in MR elastography of skeletal muscles," *Phys Med Biol*, vol. 50, pp. 1313-25, 2005.
- [65] M. A. Dresner, G. H. Rose, P. J. Rossman, R. Muthupillai, A. Manduca, and R. L. Ehman, "Magnetic resonance elastography of skeletal muscle," *J Magn Reson Imaging*, vol. 13, pp. 269-76, 2001.
- [66] G. Heers, T. Jenkyn, M. A. Dresner, M. O. Klein, J. R. Basford, K. R. Kaufman, R. L. Ehman, and K. N. An, "Measurement of muscle activity with magnetic resonance elastography," *Clin Biomech (Bristol, Avon)*, vol. 18, pp. 537-42, 2003.
- [67] T. R. Jenkyn, R. L. Ehman, and K. N. An, "Noninvasive muscle tension measurement using the novel technique of magnetic resonance elastography (MRE)," *J Biomech*, vol. 36, pp. 1917-21, 2003.

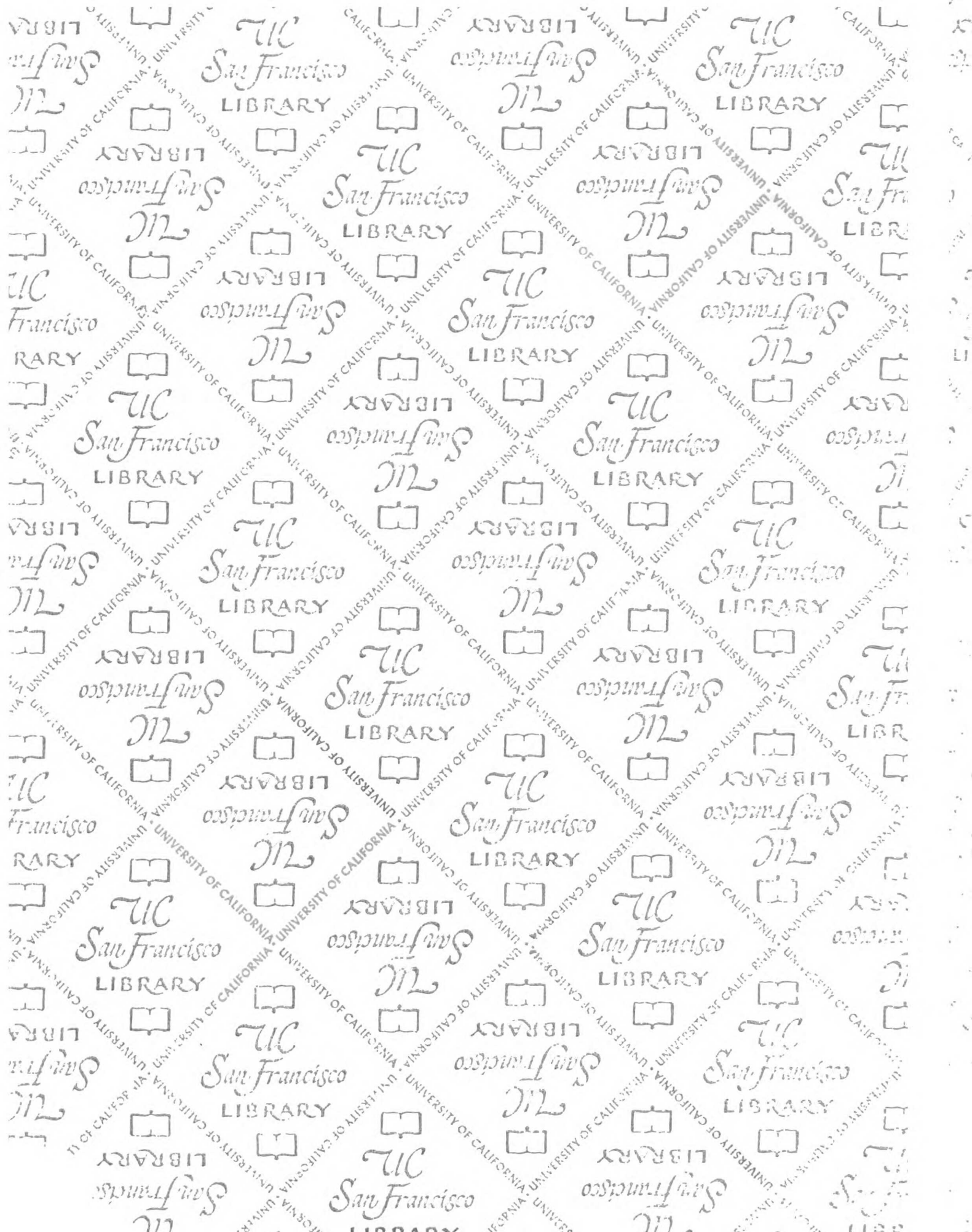
- [68] K. K. Jenkyn TR, An KN, Ehman RL, "Change in relaxed muscle stiffness due to joint positioning measured in vivo using magnetic resonance elastography," presented at ISMRM, Honolulu, 2002.
- [69] J. R. Basford, T. R. Jenkyn, K. N. An, R. L. Ehman, G. Heers, and K. R. Kaufman, "Evaluation of healthy and diseased muscle with magnetic resonance elastography," *Arch Phys Med Rehabil*, vol. 83, pp. 1530-6, 2002.
- [70] C. L. de Korte, J. A. Schaar, F. Mastik, P. W. Serruys, and A. F. van der Steen, "Intravascular elastography: from bench to bedside," *J Interv Cardiol*, vol. 16, pp. 253-9, 2003.
- [71] C. L. de Korte, M. J. Siervogel, F. Mastik, C. Strijder, J. A. Schaar, E. Velema, G. Pasterkamp, P. W. Serruys, and A. F. van der Steen, "Identification of atherosclerotic plaque components with intravascular ultrasound elastography in vivo: a Yucatan pig study," *Circulation*, vol. 105, pp. 1627-30, 2002.
- [72] C. L. de Korte and A. F. van der Steen, "Intravascular ultrasound elastography: an overview," *Ultrasonics*, vol. 40, pp. 859-65, 2002.
- [73] C. L. de Korte, A. F. W. van der Steen, E. I. Cespedes, G. Pasterkamp, S. G. Carlier, F. Mastik, A. H. Schoneveld, P. W. Serruys, and N. Bom, "Characterization of plaque components and vulnerability with intravascular ultrasound elastography," *Physics in Medicine and Biology*, vol. 45, pp. 1465-1475, 2000.
- [74] C. L. de Korte, S. G. Carlier, F. Mastik, M. M. Doyley, A. F. van der Steen, P. W. Serruys, and N. Bom, "Morphological and mechanical information of coronary arteries obtained with intravascular elastography; feasibility study in vivo," *Eur Heart J*, vol. 23, pp. 405-13, 2002.
- [75] S. G. Carlier, C. L. de Korte, E. Brusseau, J. A. Schaar, P. W. Serruys, and A. F. van der Steen, "Imaging of atherosclerosis. Elastography," *J Cardiovasc Risk*, vol. 9, pp. 237-45, 2002.
- [76] J. A. Schaar, C. L. de Korte, F. Mastik, and A. F. van der Steen, "Effect of temperature increase and freezing on intravascular elastography," *Ultrasonics*, vol. 40, pp. 879-81, 2002.
- [77] M. A. McCracken PJ, Ehman RL, "MR elastography for studying the biomechanics of traumatic brain injury.," presented at ISMRM, Toronto, 2003.
- [78] D. M. Kruse SA, Rossman PJ, Felmlee JP, Jack CR, Ehman RL, "Palpation of the brain" using magnetic resonance elastography," presented at ISMRM, Philadelphia, 1999.
- [79] S. Sampath, J. A. Derbyshire, E. Atalar, N. F. Osman, and J. L. Prince, "Real-time imaging of two-dimensional cardiac strain using a harmonic phase magnetic resonance imaging (HARP-MRI) pulse sequence," *Magn Reson Med*, vol. 50, pp. 154-63, 2003.
- [80] T. B. Kelleher and N. Afdhal, "Noninvasive assessment of liver fibrosis," *Clin Liver Dis*, vol. 9, pp. 667-83, 2005.
- [81] N. S. Shah, S. A. Kruse, D. J. Lager, G. Farell-Baril, J. C. Lieske, B. F. King, and R. L. Ehman, "Evaluation of renal parenchymal disease in a rat model with magnetic resonance elastography," *Magn Reson Med*, vol. 52, pp. 56-64, 2004.
- [82] J. L. Gennisson, T. Baldeweck, M. Tanter, S. Catheline, M. Fink, L. Sandrin, C. Cornillon, and B. Querleux, "Assessment of elastic parameters of human skin using dynamic elastography," *IEEE Trans Ultrason Ferroelectr Freq Control*, vol. 51, pp. 980-9, 2004.
- [83] J. B. Weaver, M. Doyley, Y. Cheung, F. Kennedy, E. L. Madsen, E. E. Van Houten, and K. Paulsen, "Imaging the shear modulus of the heel fat pads," *Clin Biomech (Bristol, Avon)*, vol. 20, pp. 312-9, 2005.

- [84] P. A. Hardy, A. C. Ridler, C. B. Chiarot, D. B. Plewes, and R. M. Henkelman, "Imaging articular cartilage under compression—cartilage elastography," *Magn Reson Med*, vol. 53, pp. 1065-73, 2005.
- [85] U. Hamhaber, F. A. Grieshaber, J. H. Nagel, and U. Klose, "Comparison of quantitative shear wave MR-elastography with mechanical compression tests," *Magn Reson Med*, vol. 49, pp. 71-7, 2003.
- [86] Q. Chen, S. I. Ringleb, T. Hulshizer, and K. N. An, "Identification of the testing parameters in high frequency dynamic shear measurement on agarose gels," *J Biomech*, vol. 38, pp. 959-63, 2005.
- [87] Q. Chen, S. I. Ringleb, A. Manduca, R. L. Ehman, and K. N. An, "A finite element model for analyzing shear wave propagation observed in magnetic resonance elastography," *J Biomech*, vol. 38, pp. 2198-203, 2005.
- [88] Q. Chen, S. I. Ringleb, A. Manduca, R. L. Ehman, and K. N. An, "Differential effects of pre-tension on shear wave propagation in elastic media with different boundary conditions as measured by magnetic resonance elastography and finite element modeling," *J Biomech*, 2005.
- [89] Q. Chen, B. Suki, and K. N. An, "Dynamic mechanical properties of agarose gels modeled by a fractional derivative model," *J Biomech Eng*, vol. 126, pp. 666-71, 2004.
- [90] S. I. Ringleb, Q. Chen, D. S. Lake, A. Manduca, R. L. Ehman, and K. N. An, "Quantitative shear wave magnetic resonance elastography: comparison to a dynamic shear material test," *Magn Reson Med*, vol. 53, pp. 1197-201, 2005.
- [91] A. Samani, J. Bishop, C. Luginbuhl, and D. B. Plewes, "Measuring the elastic modulus of ex vivo small tissue samples," *Phys Med Biol*, vol. 48, pp. 2183-98, 2003.
- [92] S. M. Klisch and J. C. Lotz, "A special theory of biphasic mixtures and experimental results for human annulus fibrosus tested in confined compression," *J Biomech Eng*, vol. 122, pp. 180-8., 2000.
- [93] J. C. Iatridis, L. A. Setton, R. J. Foster, B. A. Rawlins, M. Weidenbaum, and V. C. Mow, "Degeneration affects the anisotropic and nonlinear behaviors of human annulus fibrosus in compression," *J Biomech*, vol. 31, pp. 535-44., 1998.
- [94] E. R. Acaroglu, J. C. Iatridis, L. A. Setton, R. J. Foster, V. C. Mow, and M. Weidenbaum, "Degeneration and aging affect the tensile behavior of human lumbar annulus fibrosus," *Spine*, vol. 20, pp. 2690-701., 1995.
- [95] H. S. An, P. A. Anderson, V. M. Haughton, J. C. Iatridis, J. D. Kang, J. C. Lotz, R. N. Natarajan, T. R. Oegema, Jr., P. Roughley, L. A. Setton, J. P. Urban, T. Videman, G. B. Andersson, and J. N. Weinstein, "Introduction: disc degeneration: summary," *Spine*, vol. 29, pp. 2677-8, 2004.
- [96] E. J. Chiu, D. C. Newitt, M. R. Segal, S. S. Hu, J. C. Lotz, and S. Majumdar, "Magnetic resonance imaging measurement of relaxation and water diffusion in the human lumbar intervertebral disc under compression in vitro," *Spine*, vol. 26, pp. E437-44, 2001.
- [97] H. Frei, T. R. Oxland, G. C. Rathonyi, and L. P. Nolte, "The effect of nucleotomy on lumbar spine mechanics in compression and shear loading," *Spine*, vol. 26, pp. 2080-9., 2001.
- [98] J. C. Lotz, A. H. Hsieh, A. L. Walsh, E. I. Palmer, and J. R. Chin, "Mechanobiology of the intervertebral disc," *Biochem Soc Trans*, vol. 30, pp. 853-8, 2002.
- [99] J. C. Lotz, "Animal models of intervertebral disc degeneration: lessons learned," *Spine*, vol. 29, pp. 2742-50, 2004.



- [100] W. S. Marras, K. G. Davis, S. A. Ferguson, B. R. Lucas, and P. Gupta, "Spine loading characteristics of patients with low back pain compared with asymptomatic individuals," *Spine*, vol. 26, pp. 2566-74., 2001.
- [101] J. R. Meakin, T. W. Redpath, and D. W. Hukins, "The effect of partial removal of the nucleus pulposus from the intervertebral disc on the response of the human annulus fibrosus to compression," *Clin Biomech (Bristol, Avon)*, vol. 16, pp. 121-8., 2001.
- [102] P. J. Roughley, "Biology of intervertebral disc aging and degeneration: involvement of the extracellular matrix," *Spine*, vol. 29, pp. 2691-9, 2004.
- [103] J. P. Thompson, R. H. Pearce, M. T. Schechter, M. E. Adams, I. K. Tsang, and P. B. Bishop, "Preliminary evaluation of a scheme for grading the gross morphology of the human intervertebral disc," *Spine*, vol. 15, pp. 411-5, 1990.
- [104] D. Nishimura, *Principles of Magnetic Resonance Imaging*: Stanford University, 1996.
- [105] H. Carr and E. Purcell, "Effects of diffusion on free precession in nuclear magnetic resonance experiments," *Physical Review*, vol. 94, pp. 630-638, 1954.
- [106] G. K. Rossman P, Felmlee J, Ehman R, "Piezoelectric bending elements for use as motion actuators in MR elastography," presented at ISMRM, ISMRM, Toronto, 2003.
- [107] M. D. Mitchell, H. L. Kundel, L. Axel, and P. M. Joseph, "Agarose as a tissue equivalent phantom material for NMR imaging," *Magn Reson Imaging*, vol. 4, pp. 263-6, 1986.
- [108] M. A. Bernstein, K. F. King, and X. J. Zhou, *Handbook of MRI Pulse Sequences*. Burlington, MA: Elsevier Academic Press, 2004.
- [109] K. Itoh, "Analysis of the Phase Unwrapping Algorithm," *Applied Optics*, vol. 21, pp. 2470-2470, 1982.
- [110] D. C. Ghiglia and M. D. Pritt, *Two-dimensional phase unwrapping: theory, algorithms, and software*. New York: John Wiley & Sons, 1998.
- [111] H. Knutsson, C.-F. Westin, and G. Granlund, "Local multiscale frequency and bandwidth estimation," presented at Image Processing, 1994. Proceedings. ICIP-94., IEEE International Conference, 1994.
- [112] A. Manduca, R. Muthupillai, P. J. Rossman, J. F. Greenleaf, and R. L. Ehman, "Local wavelength estimation for magnetic resonance elastography," presented at Image Processing, 1996. Proceedings., International Conference on, 1996.
- [113] J. C. Iatridis, M. Weidenbaum, L. A. Setton, and V. C. Mow, "Is the nucleus pulposus a solid or a fluid? Mechanical behaviors of the nucleus pulposus of the human intervertebral disc," *Spine*, vol. 21, pp. 1174-84., 1996.
- [114] A. D. Bodine AJ, Hayes WC, White AA, "Viscoelastic shear modulus of the human intervertebral disc.," *Transactions of the Orthopedic Research Society*, vol. 7, pp. 237, 1982.
- [115] J. P. Urban and A. Maroudas, "Swelling of the intervertebral disc in vitro," *Connect Tissue Res*, vol. 9, pp. 1-10, 1981.
- [116] D. S. Bradford, T. R. Oegema, Jr., K. M. Cooper, K. Wakano, and E. Y. Chao, "Chymopapain, chemonucleolysis, and nucleus pulposus regeneration. A biochemical and biomechanical study," *Spine*, vol. 9, pp. 135-47, 1984.
- [117] K. J. Glaser, J. Felmlee, and R. L. Ehman, "High-Speed Reduced-FOV MR Elastography," presented at ISMRM, Miami, 2005.
- [118] J. Rump, D. Klatt, C. Warmuth, J. Braun, U. Hamhaber, S. Papazoglou, and I. Sack, "Synchronisation of shear vibrations and balanced steady state free precession in MR Elastography (SSFP-MRE)," presented at ISMRM, Miami, 2005.

- [119] O. Bieri, S. Maderwald, M. E. Ladd, and K. Scheffler, "Balanced Alternating Steady-State Elastography," presented at ISMRM, Miami, 2005.
- [120] T. Wu, J. P. Felmlee, J. F. Greenleaf, S. J. Riederer, and R. L. Ehman, "MR imaging of shear waves generated by focused ultrasound," *Magn Reson Med*, vol. 43, pp. 111-5, 2000.
- [121] T. Wu, J. P. Felmlee, J. F. Greenleaf, S. J. Riederer, and R. L. Ehman, "Assessment of thermal tissue ablation with MR elastography," *Magn Reson Med*, vol. 45, pp. 80-7, 2001.
- [122] M. M. Doyley, F. Mastik, C. L. de Korte, S. G. Carlier, E. I. Cespedes, P. W. Serruys, N. Bom, and A. F. van der Steen, "Advancing intravascular ultrasonic palpation toward clinical applications," *Ultrasound Med Biol*, vol. 27, pp. 1471-80, 2001.





7487278

3 1378 00748 7278

**For  
reference**

Not to be taken  
from the room.

